SPIN TRANSFER TORQUE INDUCED SWITCHING IN MAGNETIC TUNNEL JUNCTION FOR STT-RAM APPLICATION

A DISSERTATION
SUBMITTED TO THE FACULTY OF
UNIVERSITY OF MINNESOTA
BY

HUI ZHAO

IN PARTIAL FULFILLMENT OF THE REQUIREMENTS
FOR THE DEGREE OF
DOCTOR OF PHILOSOPHY

PROFESSOR JIAN-PING WANG

DECEMBER 2013

Acknowledgements

It is a great pleasure for me to acknowledge all the help and support that I got in pursuit of my graduate degree.

First of all, I would like to express my gratitude to my advisor Prof. Jian-Ping Wang for giving me the opportunity to work on such an exciting topic. During the five years of my study, his patience, constant support and guidance have been a significant help. The knowledge and experience I obtained during those years will be a precious treasure for my future.

I would also like to thank my committee members, who have helped me a lot on my study. Prof. Randall Victora's knowledgeable and excellent teaching laid a solid foundation for my understanding on magnetics. Through all the fruitful discussions with Prof. Chris Kim, I learned to evaluate the magnetic results from the circuit and system point of view. It broadened my knowledge of the STT-RAM technology. Prof. Paul Crowell inspired me with his scientific enthusiasm and rigorous scholarship. I sincerely appreciate his help and valuable input on my work.

My thesis is done in collaboration with Prof. Chris Kim's group in UMN, Prof. Kang Wang's and Prof. Hongwen Jiang's group in UCLA, Prof. Ilya Krivorotov's group in UCI, Dr. J. A. Katine's group in HGST and Dr. Jüergen Langer in Singulus. I would like to thank all the collaborators in the projects, especially Dr. J. A. Katine and Dr. Jüergen Langer for the help on preparing the MTJ samples. Many thanks to all the students and scholars worked in the projects, Dr. Kichul Chun, Dr. Wei Zhang, Dr. Pedram Khalili

Amiri, Dr. Zhongming Zeng, Dr. Graham Rowlands Dr. Andrew Lyle, Dr. Tofizur Rahma and Pramey Upadhyaya. I would also like to thank all the UMN Nanofabrication Center staff members for their help and suggestions.

Sincere gratitude goes to all the students worked with me in the lab. It is my pleasure to work in close collaboration with Yisong Zhang during those years and together we have made a lot of things happen. Thanks to Dr. Andrew Lyle, Dr. Tofizur Rahma, Dr. Mahdi Jamali, Dr. Xiaofeng Yao, Brain Glass, Jonathan Harms and Xuan Li for the collaboration and valuable discussions. I would also like to thank all other students Dr. Liang Tu, Dr. Yuanpeng Li, Dr. Nian Ji, Dr. Ying Jing, Dr. Hao Wang, Dr. Xiaoqi Liu, Todd Klein, Yi Wang, Yinglong Feng, Xiaowei Zhang, Xiaohui Chao, Angeline Klemm, Shaoqian Yin, Meiyin Yang, Yang Lv, Jinmin Liu and Patrick Quarterman for their friendship.

Last but not the least, my deepest gratitude goes to my parents for their unconditional love and support. I am also very grateful that I have my husband Shihai in companion during those years. To them, this thesis is dedicated.

Abstract

This thesis describes experimental studies of the spin transfer torque induced switching in magnetic tunnel junctions (MTJ) for the application of spin transfer torque random access memory (STT-RAM).

In the material development; the in-plane MTJ was optimized in order to meet the requirement of STT-RAM application. Perpendicular magnetocrystalline anisotropy was obtained in the $L1_0$ phase FePd designed for the top MTJ electrode and bottom MTJ electrode. Moreover, full CoFeB MTJ with interface perpendicular anisotropy was developed. An average of 48% reduction in the intrinsic critical current density was found by increasing the interface perpendicular anisotropy. Sub 200 ps ultrafast STT induced switching was also demonstrated in those CoFeB MTJs where the out-of-plane demagnetizing field was partially canceled by the interface perpendicular anisotropy. High J/J_{c0} ratio and magnetization nucleation at the edge of free layer are possibly the two major factors that contribute to the ultrafast spin transfer torque switching.

In the spin transfer torque (STT) induced switching study; systematic characterization of the probabilistic STT induced switching process was done. It includes the three STT induced switching modes, the switching energy, the switching speed and the high precision switching probability density function (PDF). The temperature dependent MTJ properties and STT switching distribution was also studied. Those results provided key parameters for the STT-RAM design. In the end, direct and compelling experimental evidence was provided to show the large dynamic energy barrier reduction induced by high frequency spin current excitations. The concept of magnetization logarithmic

susceptibility was proposed to describe this dynamic effect. By comparing with the simulation results, the measured logarithmic susceptibility frequency response was used to reveal the magnetic properties of MTJs and understand the spin-transfer torque induced magnetization switching dynamics.

Table of Contents

List of Tables

List of Figures

1 Introduction

1.1 Magnetic tunnel junction

A magnetic tunnel junction (MTJ) is a thin film magnetic device, which includes two ferromagnetic layers separated by a thin dielectric barrier layer. The conductance of the device is determined by the spin-dependent tunneling phenomenon. The key to the spin-dependent tunneling is the spin-filter effect of ferromagnetic (FM) material. It means that when electrons pass through the FM layer, the ratio of the up-spin and down-spin in the flowing electrons will follow the ratio of available states in the majority-spin band and minority-spin band of the FM layer. Such a current is then called "spin polarized".

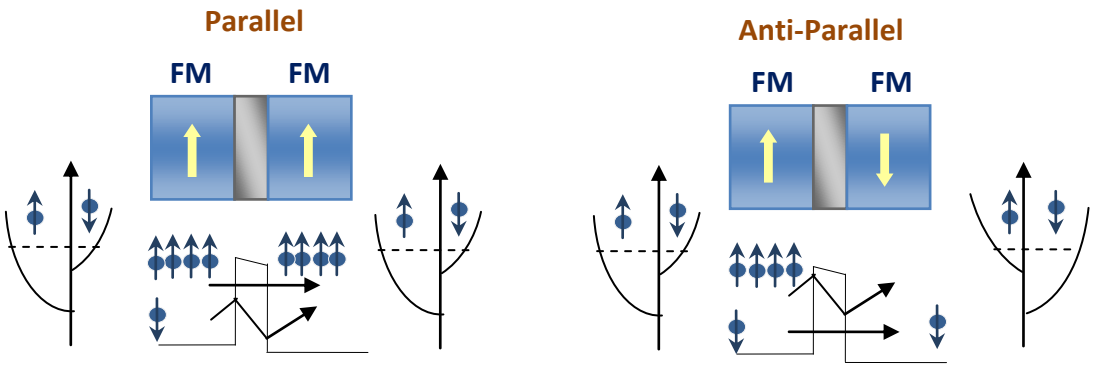

Fig. 1.1 Schematic illustration of the spin dependent tunneling effect in a parallel aligned MTJ and an anti-parallel aligned MTJ.

Fig. 1.1 illustrates the spin-dependent tunneling phenomenon in a MTJ. For electrons traveling from left to right, they are first filtered by the left FM layer. The majority electron passing through the left FM layer will have the up-spin states. The right FM

layer then works as the second spin-filter. In the case of the two FM layers having their magnetization aligned in parallel direction (left figure of Fig. 1), the up-spins have higher probability to tunnel through the barrier compared to the down-spins since there are more up-spin states available in the majority band of the right FM layer. On the other hand, in the anti-parallel aligned case (right figure of Fig. 1), the down-spins get a better chance to tunnel through the barrier. As a result, the parallel aligned FM layers overall allow more tunneling electrons and it leads to a lower resistance. The resistance difference is described by the tunneling magnetoresistance (TMR) ratio, defined as $(R_{ap}-R_p)/R_p$, where R_{ap} and R_p represent the resistances of the anti-parallel (AP) aligned MTJ and parallel (P) aligned MTJ respectively.

Tunneling magnetoresistance was first reported by Julliere as early as 1975[1]. He found a 14% TMR ratio at 4.2K in Fe/Ge–O/Co MTJ. However, it did not attract much attention for a decade because the TMR ratio dropped quickly to zero as the temperature increased. Research in this area boomed after1995 when Miyazaki *et al* and Moodera *et al* reported 18% TMR ratio at room temperature in the amorphous Al-O barrier MTJ[2–4]. The number increased to 70% until 2004 in Al-O barrier MTJ[5]. Another milestone in this area was the great success of MgO barrier MTJ. The 200% room temperature TMR ratio in MgO MTJ was first reported by Yuasa's and Parkin's groups in 2004[6,7]. Now the TMR ratio in MgO MTJ is over 600%[8]. This ultra high TMR ratio in MgO MTJ is referred to giant TMR.

The giant TMR in MgO barrier MTJ can be explained by the coherent tunneling model according to the first principle calculation in the Fe(001)/MgO(001)/Fe(001)

structure[9,10]. Among all Bloch states in the Fe (001) electrode, the Δ_1 spd hybridized states, Δ_2 d states and Δ_5 pd hybridized states are the dominant ones. First principle calculations show that Δ_1 has a large positive spin polarization value at Fermi energy in Fe (001), while Δ_2 and Δ_5 states have a relatively small negative spin polarization value at Fermi energy, which means Δ_2 and Δ_5 states reduce the total spin polarization and the ratio. When the three Bloch states in Fe (001) are coupled with the respective evanescent states in the crystalline MgO (001) barrier, the decay of the Δ_2 and Δ_5 states is much stronger than that of the Δ_1 state during the tunneling process. Therefore, the negative contribution to the TMR ratio from the Δ_2 and Δ_5 states is eliminated. However, in case of amorphous Al-O barrier, all the three states have the same tunneling probability. Thus, the net spin polarization is the sum of the positive and negative spin polarizations of the three states. It is much smaller than the value in the coherent tunneling model with the crystalline MgO (001) barrier.

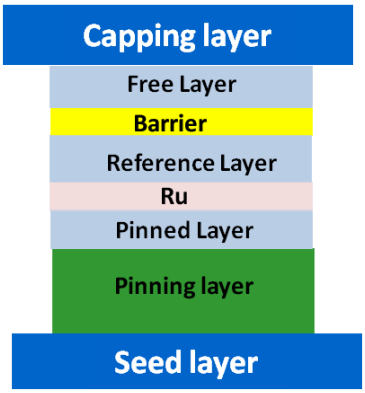

Fig. 1.2 Typical MTJ multi-layer schematic structure

A typical MgO MTJ structure is shown in Fig. 1.2. It consists of a pinning layer,

pinned layer, Ru layer, reference layer, barrier and free layer. The pinning layer is made of an antiferromagentic (AFM) material, such as IrMn, PtMn etc. The pinned layer, reference layer and free layer are made of ferromagnetic material. When the Ru layer is around 0.8 nm, the reference layer and pinned layer are strongly anti-parallel coupled through the RKKY exchange coupling effect. Those three layers are also called synthetic antiferromagentic (SAF) layers.

1.2 Spin Transfer Torque

The pioneering Spin transfer torque (STT) work starts from the research in magnetic domain wall motion. Berger first predicted domain wall motion driven by STT in 1978[11,12] and observed it in experiment afterwards in 1985[13] and 1988[14]. However, this phenomenon did not attract much attention until fabrication of 100 nm magnetic wires was possible by the advanced nanofabrication techniques. Modern research on STT driven domain wall motion has been pursued vigorously[15–21], and a new 3D memory "Racetrack" has been proposed based on this phenomenon[22,23]. Another important research area of STT is in the magnetic multilayer structure: spin value and MTJ. In 1989, Slonczewski first calculated the interlayer exchange coupling in MTJ as a result of the spin polarized current[24]. The specific STT concept was proposed by Slonczewski and Berger independently in 1996[25,26]. They predicted that the magnetization of a ferromagnetic layer can be switched by a spin-polarized current through the STT effect. Slonczewski further pointed out that the magnetization can also stay in a steady-state precession when damping is canceled by STT[27]. Those theoretical predictions were soon proved by experiments both in spin valves and MTJs[28–31]. It quickly become one of the

most attractive research topics in magnetics due to many promising applications[32], such as STT-RAM[33,34], magnetic oscillators[35], microwave detectors[36] and so on.

STT happens as a result of the spin-filter effect. It can be illustrated in a simplified 2D picture as shown in Fig. 1.3(a). Consider an incident electron state with its spin oriented θ° away from the direction of the FM layer magnetization. As discussed before, when the electron passes through a ferromagnetic material, its spin-angular momentum will follow the local majority spin and minority spin direction. Assuming the spin polarization factor of the FM material is 1, only electrons with their spin aligned parallel with the FM magnetization will pass through, and the anti-parallel aligned electrons will be reflected. In this process, the spin-angular momentum of the flowing electrons is not conserved in the transverse direction. The loss of the spin-angular momentum is absorbed by the local electrons in the ferromagnet and will consequently act like a "torque" to rotate the magnetization of the ferromagnet as indicated by the red arrow in Fig. 1.3(a). It is named as spin transfer torque. The strength of the STT can be calculated by considering the angular momentum conservation of the whole system during the spin-

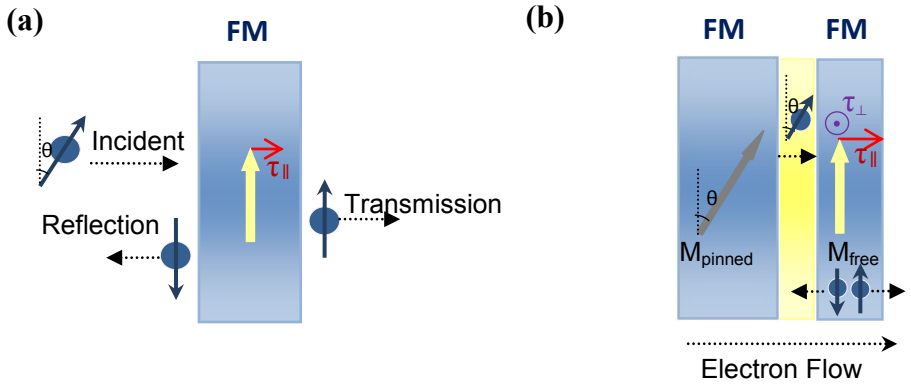

Fig. 1.3 (a) Illustration of the in-plane spin transfer torque in 2D model; (b) Illustration of the spin transfer torque in spin valve or MTJ.

filtering process.

Please note that the above picture is a simplified 2D illustration. When averaging the available states over the FM material's Fermi surface in 3D, the flowing electrons' spin-angular momentum may also be non-conserved in the out-of-plane direction. It results in an additional STT in the out-of-plane direction, which is usually referred as the perpendicular torque ($\tau_{\perp}$). In contrast, the transverse STT discussed in the previous paragraph is named as the in-plane torque ($\tau_{\parallel}$). Unlike the in-plane torque, the perpendicular torque is conservative and its effect on the magnetic energy potential can also be understood similar to the external magnetic field. That's why it's also called field-like torque. Another way in which perpendicular torque also differs from the in-plane torque in its non-zero value at zero current flow. In this case, it contributes to the generally observed "interlayer exchange coupling" from the energy point of view[24]. First principle calculation results and experimental results both show that the in-plane torque is the dominant STT effect. The perpendicular torque is typically 1-3% of the in-plane torque in the metallic multilayers[37–39] and 10%-30% of the in-plane torque in the MTJs[40–42].

As shown in Fig. 1.3(b), in the spin valve or MTJ structure with electrons flowing from left to the right, the electrons will first be polarized by the pinned layer. Therefore, the incident electrons to the free layer have their spin aligned parallel to the pinned layer. The in-plane torque ($\tau_{\parallel}$) and perpendicular torque ($\tau_{\perp}$) on the free layer are labeled in red and purple in the figure respectively. The two torques can be described as follows:[25,26,29,43]

$$\tau_{\parallel} = a_J M \times \left(M \times M_p \right), \qquad \tau_{\perp} = b_J M \times M_p , \tag{1.1}$$

where **M** and $\mathbf{M_p}$ are the normalized magnetizations of the free layer and pinned layer respectively, a_J and b_J are the magnitude parameter for in-plane torque and perpendicular torque, respectively. According to Slonczewski's theory,[26,27]

$$a_J = \frac{\gamma \hbar J \eta}{2eM_s t} \tag{1.2}$$

where J is the current density, M_s is the free layer's saturation magnetization and t is the free layer thickness. η is the spin polarization factor $\eta = (n_\uparrow - n_\downarrow)/(n_\uparrow + n_\downarrow)$, where $n_\uparrow$ and $n_\downarrow$ are the carrier density in the spin up and spin down channels, respectively. The magnitude of b_J is still under study.

The complete dynamic motion of the free layer magnetization can be described by adding the two STT components to the Landau-Lifshitz-Gilbert (LLG) equation:

$$\frac{dM}{dt} = -\gamma M \times H_{eff} + \alpha M \times \frac{dM}{dt} + a_J M \times (M \times M_p) + b_J M \times M_p , \tag{1.3}$$

where $\mathbf{H_{eff}}$ is the effective field including magnetic anisotropy field and external field, γ is the gyromagnetic ratio and α is the Gilbert damping constant. The first term on the right ($-\gamma M \times H_{eff}$) is the precession term, which keeps the free layer magnetization in a precessional motion around $\mathbf{H_{eff}}$ direction. The second term

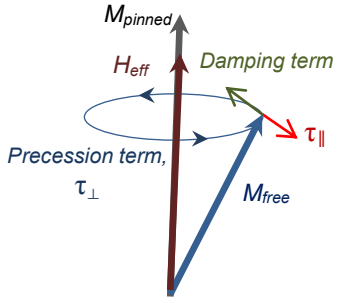

Fig. 1.4 Direction of all terms in the modified LLG equation (Eq. (1.3)) when the pinned layer magnetization and effective field are in the same direction.

($\alpha M \times \frac{dM}{dt}$) is the damping term, which moves the free layer magnetization towards $\mathbf{H_{eff}}$.

Fig. 1.4 indicates the direction of all terms when the effective field and the pinned layer magnetization are in the same direction. Please note the direction of the in-plane torque is determined by the polarity of voltage bias as indicated by Eq. (1.2). Depending on the applied voltage polarity, it can be in the same or opposite direction of the damping term. Similarly, the perpendicular torque will be in the same or the opposite direction of the precession term, though the exact bias voltage dependence of b_J is still under debate.

Next, let's discuss the free layer magnetization dynamics driven by the spin transfer torque[47]. Assume the initial position of the free layer magnetization has an angle to the easy axis as shown in Fig. 1.4. In a real sample, this angle comes from thermal fluctuations. When the in-plane torque is in the opposite direction of the damping term, the magnetization dynamics is determined by the competition of the damping term and the in-plane torque. There are three possible scenarios. First, if the damping term is larger than in-plane torque, the free layer magnetization will spiral back towards $\mathbf{M_p}$. Second, if the damping term is equal to the in-plane torque, the free layer magnetization will stay in a steady precession mode. Third, if the damping term is smaller than the in-plane torque, the free layer magnetization will spiral away from $\mathbf{M_p}$. The three scenarios are illustrated in Fig. 1.5 according to the macrospin LLG model. Fig. 1.5(a) shows the magnetization trajectories if the free layer is a circular thin film pillar with its easy axis and $\mathbf{M_p}$ in the out-of-plane direction. Fig. 1.5(b) shows another case when the free layer is an elliptical thin film pillar with its easy axis and $\mathbf{M_p}$ in plane along y direction. In the

second case, the magnetization trajectory is highly constrained near the thin film plane because of the shape anisotropy.

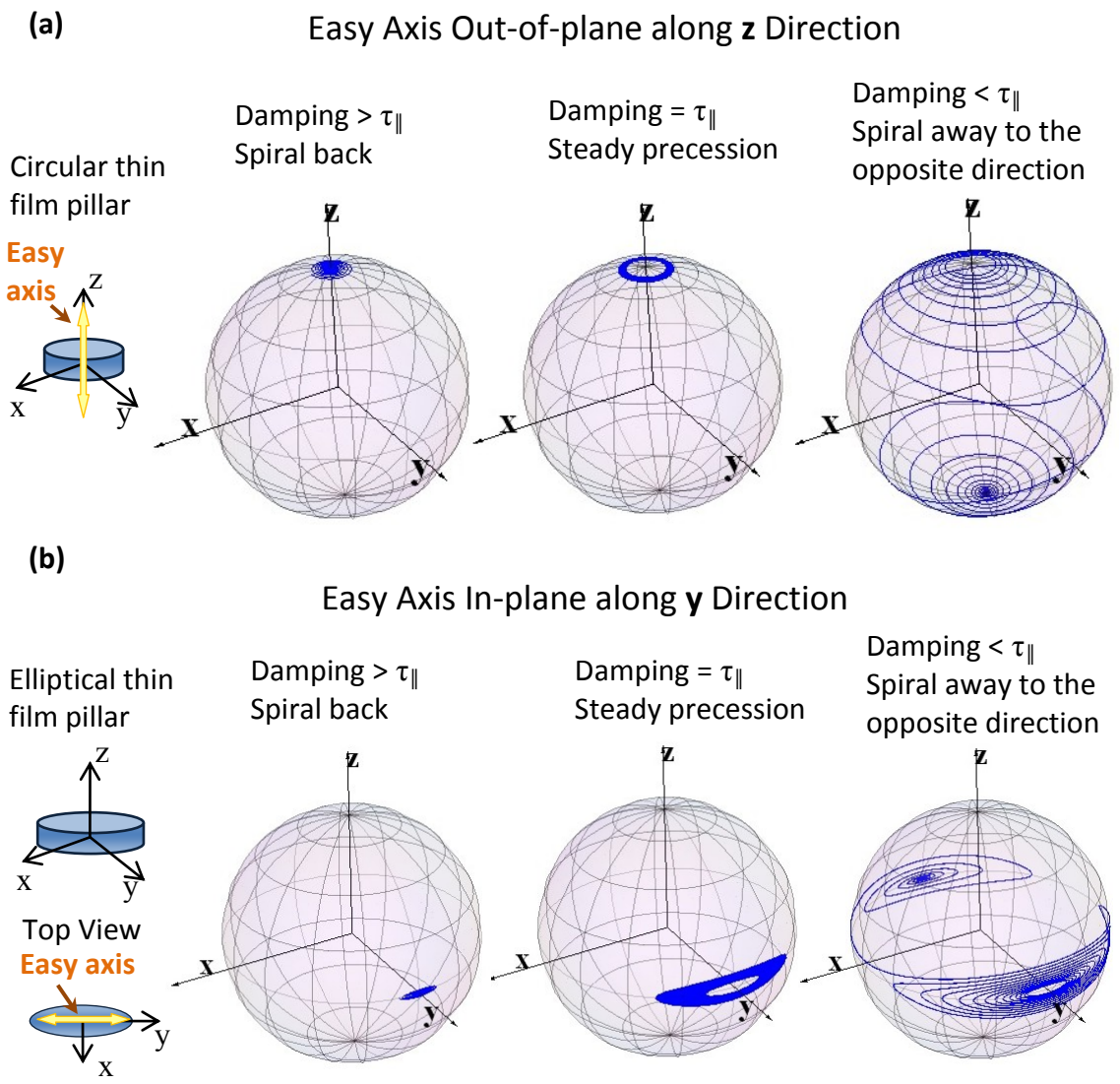

Fig. 1.5, Magnetization trajectory under in-plane spin transfer torque. (a) The free layer is a circular thin film pillar with its easy axis out-of-plane along z direction. The pinned layer magnetization is also along z direction. (b) The free layer is an elliptical thin film pillar with its easy axis in plane along y direction. . The pinned layer magnetization is also along y direction.

The minimum current value that can switch the free layer magnetization to its opposite direction is defined as the critical current. It can be estimated by integrating the energy gain/loss during a full precessional circle and determining the critical value at which the in-plane torque starts to overcomes the damping. For the circular thin film pillar with its easy axis in the out-of-plane direction, the critical current is [48]

$$I_{c0} = \frac{2e\alpha M_s V(H + H_{\perp k} - 4\pi M_s)}{\hbar \eta}, \tag{1.4}$$

where M_s is the saturation magnetization, V is the free layer volume, H is the applied field in the out-of-plane direction, and $H_{\perp k}$ is the perpendicular anisotropy field.

For a elliptical thin film pillar with its easy axis in plane along the long axis of the ellipse, the critical current is [47]

$$I_{c0} = \frac{2e\alpha M_s V(H + H_{\| k} + 2\pi M_s)}{\hbar \eta}, \tag{1.5}$$

where H is the applied field in parallel to the in-plane easy axis, and $H_{\| k}$ is the in-plane anisotropy field.

1.3 Spin transfer torque random access memory (STT-RAM)

One important application of STT effect is spin transfer torque random access memory (STT-RAM). It is currently under intensive development as a candidate for next generation memory technologies[33,34,49–56]. The potential advantages of STT-RAM include its nonvolatility, fast write speed, low energy consumption, and scalability with CMOS technology.

Fig. 1.6 (a) shows a schematic structure of a single STT-RAM memory cell. It uses the MTJ device as the storage unit. The two resistance states R_p and R_{ap} are regarded as "0" and "1" states. The writing process is done by the STT induced free layer magnetization switching as discussed in the previous section. When the electrons are injected from the pinned layer to the free layer and the injected current is larger than the critical current, the free layer magnetization will switch to the parallel direction of the pinned layer as a result of the in-plane spin torque (Fig. 1.6(b)). On the other hand, when the electrons are injected from the opposite direction, the in-plane spin torque will flip its direction and thus the free layer magnetization will switch to the anti-parallel direction of the pinned layer (Fig. 1.6(c)). The transistor underneath MTJ is used to control the current injection for selective writing and reading.

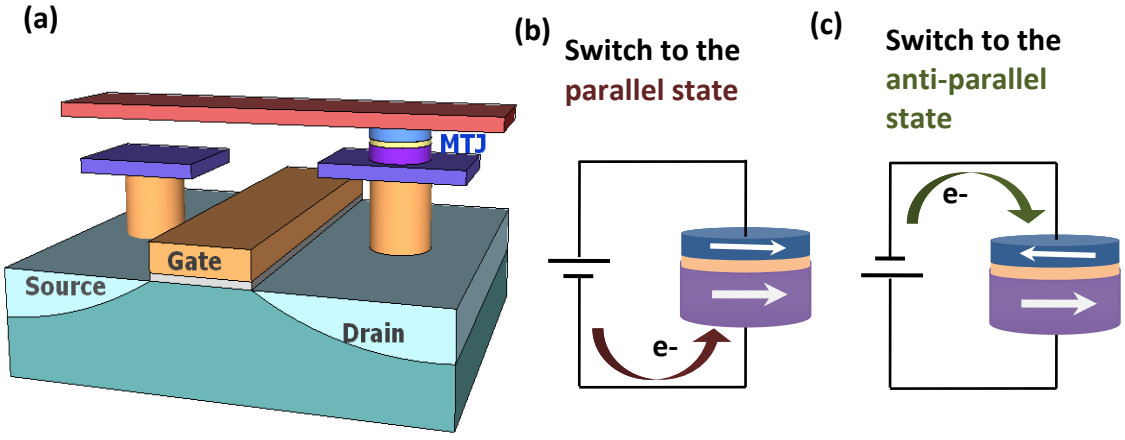

Fig. 1.6 (a) Schematic structure of a single memory cell of STT-RAM. (b) The writing principle of STT-RAM

Here I will briefly explain several key aspects of the STT-RAM development.

A. TMR ratio and resistance variation

The TMR ratio and sample to sample resistance variation determine whether the two states are distinguishable during the reading process. Higher TMR ratio and smaller sample to sample variation ensures a larger read margin. Fig. 1.7 shows an example of the two resistance state distribution in a 14Kb STT-RAM chip sub-array made by Grandis[57]. It demonstrated a 20σ separation between states.

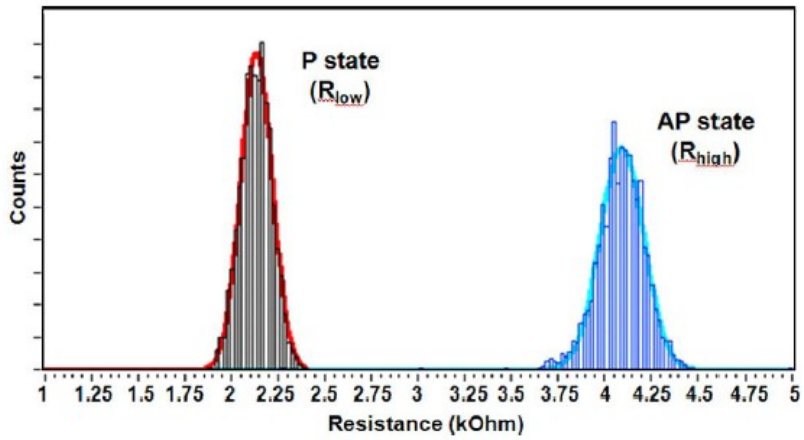

Fig. 1.7 The parallel and anti-parallel resistance distribution in a 14Kb STT-RAM chip sub-array by Grandis. Figure from Ref. 57.

B. Writing energy and writing speed

The critical current given in Eqs. (1.4) and Eq. (1.5) is calculated at zero temperature from the macrospin model. Therefore, it is also named as the intrinsic critical current. At finite temperature, the critical switching current is also affected by thermal fluctuation. The critical switching current reduction as a result of the thermal fluctuation can be written in the following equation, analogous to the field switching case[58,59].

$$I_c(\tau) = I_{c0}\left[1 - \frac{k_B T}{K_u V}\ln\left(\frac{\tau}{\tau_0}\right)\right], \tag{1.6}$$

where I_{c0} is the intrinsic critical current in Eq. (1.4) and Eq. (1.5), K_u is the magnetic anisotropy, V is the free layer volume, k_B is the Boltzmann constant, T is the temperature, τ is the pulse width and τ_0 is the attempt time of thermal agitation, which is assumed to be 1 ns. According to the physical picture of the thermal agitation, it's easy to understand that Eq. (1.6) only works when the pulse width is much longer than the thermal attempt time (1 ns), in other words, in the long pulse regime. For pulse width comparable or shorter than the thermal attempt time (1 ns), the STT induced switching process is almost independent of the thermal agitation. The switching time can be estimated approximately from the zero temperature macrospin model: $\tau \propto \frac{\ln(\pi/2\theta_0)}{I_c - I_{c0}}$, where θ_0 is initial angle between the free layer and pinned layer[29]. Therefore, for the short pulse regime,

$$I_c - I_{c0} \propto \frac{\ln(\pi/2\theta_0)}{\tau} \tag{1.7}$$

Fig. 1.8 summarizes the critical switching current as a function of the pulse width[33]. I will discuss more about the three switching modes in Chapter 4.3.1. Overall, we can see the required critical switching current increases as the reduction of pulse width. Therefore, there is always a trade-off between writing energy and writing speed.

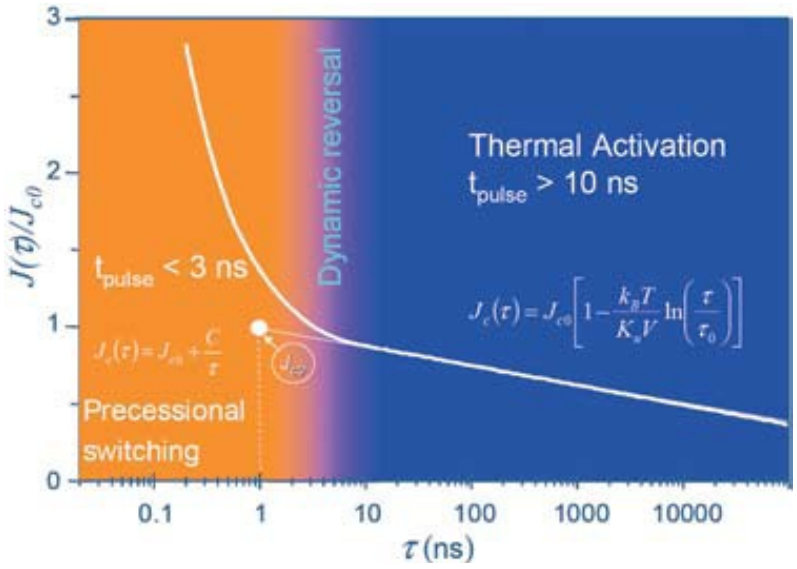

Fig. 1.8 Critical switching current density versus switching time. Three switching modes are indicated. Figure from Ref. 33.

C. Write error rate and read disturb rate

Until now, the critical switching current (I_c) is treated as a simple threshold value. Above the threshold value, the switching probability is 1, and below the threshold value the switching probability is 0 (Blue curve in Fig. 1.9). However, at finite temperature, the threshold value is dispersed due to the random thermal fluctuation during each switching process (red curve in Fig. 1.9). Therefore, cumulative switching probability characterization is required to study the STT driven switching process. From a product engineering point of view, the read disturb rate (RDR) means the probability of accidental switching during the reading process. It corresponds to the starting edge of the cumulative switching probability function curve. Write error rate (WER) stands for the unsuccessful switching during the writing process. It corresponds to the ending edge of the cumulative switching probability function curve. As a result, the read margin and

write margin are decided by the RDR and WER respectively. An error rate of 6×10^{-10} is reported to be tolerable with proper error correction code.

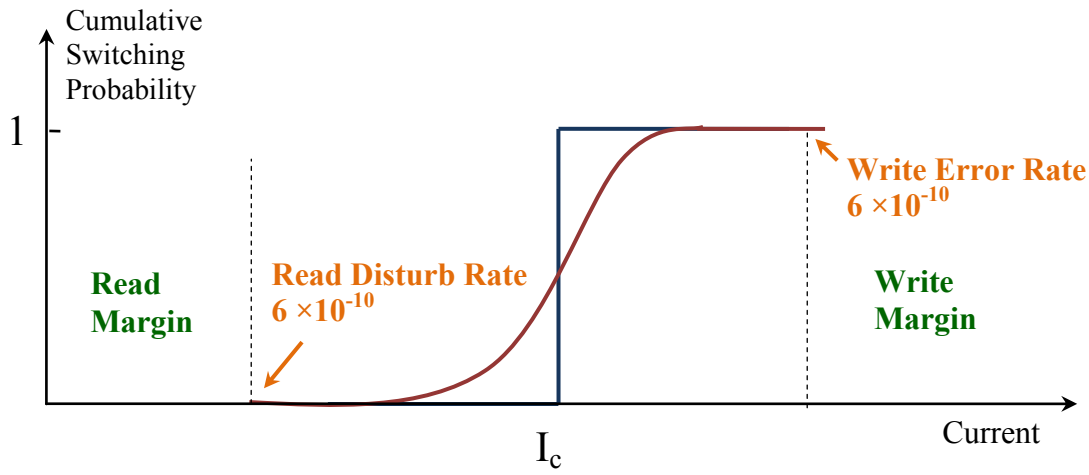

Fig. 1.9 Schematic picture of the cumulative switching probability as a function of current.

D. Data retention time

As a nonvolatile memory technology, the free layer magnetization must be able to keep its direction for enough time against the thermal agitation, which is called the data retention time. The requirement of data retention time depends on different applications. For example, if it is going to be used as a "permanent" data storage option such as hard disk drive, the data retention time should be 10 years. If it is designed to replace the CPU cache, a much shorter data retention time is acceptable since the device goes under frequent writing process in its working condition. The data retention time can be estimated from the thermal agitation induced switching probability[59].

$$P_{sw}(t) = 1 - \exp(-\frac{t}{\tau_0 \exp(\Delta)}), \qquad \Delta = \frac{K_u V}{k_B T} \tag{1.8}$$

where the t is the idle time and Δ is called thermal stability factor. The thermal stability factor for in-plane MTJ and perpendicular MTJ are as follows:

$$\Delta_{\parallel} = \frac{K_u V}{k_B T} = \frac{M_s H_{\parallel k}}{2} \frac{V}{k_B T}, \tag{1.9}$$

$$\Delta_{\perp} = \frac{K_u V}{k_B T} = \frac{M_s (H_{\perp k} - 4\pi M_s)}{2} \frac{V}{k_B T}. \tag{1.10}$$

Assume the 6×10^{-10} accidental switching rate is tolerable among 1 Gbit memory cells. For the 10 years, 1 year, 1 day, 1 hr and 60 s retention time requirements, the thermal stability factor should be 75, 73, 67, 64 and 60 respectively.

E. Barrier endurance

Since the writing process is done by STT induced switching, the thin MgO barrier has to survive under the voltage stress. The major threat of barrier failure comes from dielectric breakdown. This issue is especially important for the ultrafast writing operation where the writing voltage is close to its breakdown voltage as shown in Fig. 1.10. Min *et al* showed their MTJ barrier has a 0.02 failure rate under 1.107 V for 830 ns[52]. The barrier endurance under voltage stress determines the maximum writing cycle of the product.

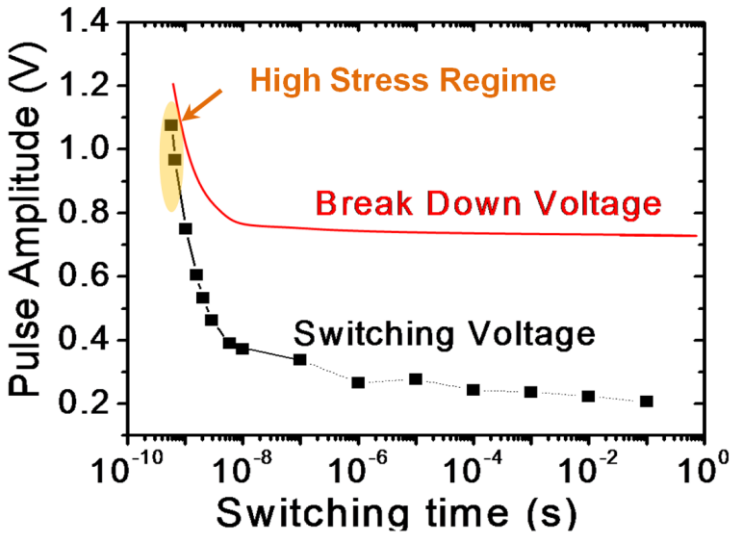

Fig. 1.10 The critical switching pulse voltage as a function of pulse width. The black dots are the measured results. The read curve indicates the assumed break down voltage. The yellow regime represents the high voltage stress regime.

1.4 Overview of my thesis

In Chapter 1, I have covered the background about my thesis, including the knowledge about MTJ, STT and STT-RAM.

In Chapter 2, I will first introduce all techniques and procedures of the MgO MTJ fabrication, including thin film deposition and nanofabrication. Then, I will also discuss the basic measurement techniques about MTJ and STT induced switching.

Chapter 3 describes my efforts on the MTJ device development for STT-RAM application. The first section introduces the optimization of MgO barrier thickness, junction size and CoFeB free layer thickness in the in-plane MTJs. In order to further scale down the MTJ size and reduce its writing energy, perpendicular magnetic anisotropy is preferred. The second section then talks about my work on developing the

perpendicular anisotropy in $L1_0$ FePd and CoFeB thin films.

Chapter 4 includes my general study of STT induced switching. It is mainly based on the pulse width dependent STT induced switching probability measurement. In this chapter, I will discuss the three STT induced switching modes, the switching energy, the switching speed and the switching distribution based on my measurement results. In the end, the temperature dependent STT induced switching behavior is also characterized.

Chapter 5 introduces my contribution to the ultrafast STT induced switching. The sub 200 ps ultrafast switching in thermally stable in-plane MTJs is demonstrated. The observed ultrafast switching is believed to occur because of partially canceled out-of-plane demagnetizing field in the free layer from interface perpendicular anisotropy. Here I proved that in the simple in-plane MTJ structure without extra energy assistance, ultrafast switching speed is still achievable.

In Chapter 6, I will shift my discussion to the dynamic energy barrier reduction under high frequency spin current excitation. The magnetization logarithmic susceptibility theory is used here to characterize such dynamic energy barrier reduction. I provide direct and compelling experimental evidence for the first time to prove the theory. By fitting the theory to the experiment results, I also propose a new methodology to reveal the damping parameter, the magnetic anisotropy and the magnetic dynamics during STT induced switching process.

In the last Chapter, I will give a complete summary of this work.

2 Magnetic tunnel junction fabrication and characterization

2.1 Thin film deposition

Magnetron sputtering is the main technology used to deposite the multilayer MTJ thin film stacks. The working principle of magnetron sputtering is illustrated in Fig. 2.1[60]. In the simple DC sputtering process, the sputtering target and substrate are connected to the cathode and anode of the DC power supply, respectively. When Ar gas is supplied, plasma can be excited and it will be confined by the magnetic field near the target surface as indicated by the purple color in the figure. Meanwhile, the Ar^- ion inside the plasma will be accelerated by the electrical field towards the target surface. As a result, the target atoms are ejected from the target surface because of the Ar^- ion bombardment. This sputtering process has to work in a high vacuum environment to make sure the ejected target atoms have a small chance to collide with other species and eventually reach the substrate surface. If the target material is non-conducting, negative charges will accumulate on the target surface without a good way to flow out. It will eventually repeal any further Ar^- ion bombardment and unable to maintain a stable plasma. Therefore, RF power supply is used for insulate target material. In this way, negative charge accumulation can be avoided by the alternating voltage.

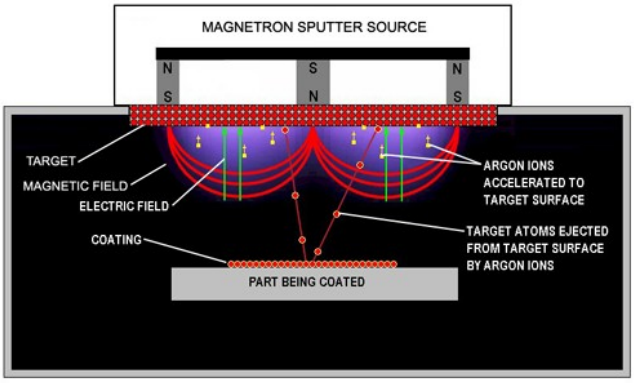

Fig. 2.1 The schematic picture of the magnetron sputtering working principle. Figure from Ref. 60.

In this work, the MTJ multilayer stacks are deposited by a Shamrock sputtering system and a Singulus TIMARIS sputtering system. The system pictures are shown in Fig. 2.2. The Shamrock system in University of Minnesota consists of a loadlock chamber for sample loading, an intermediate chamber for wafer transfer and a main chamber for sputtering. The intermediate chamber and main chamber are equipped with turbo pump and cryogenic water pump, which ensure a good base vacuum of 3×10^{-8} Torr. Five DC sputtering guns and a RF sputtering gun are installed in the main chamber. In addition, an ion mill gun is also added to the main chamber for the wafer cleaning. The Singulus TIMARIS sputtering system is located in Singulus Company, which is used to deposite the ultrathin MgO barrier MTJ samples in this thesis.

(a)

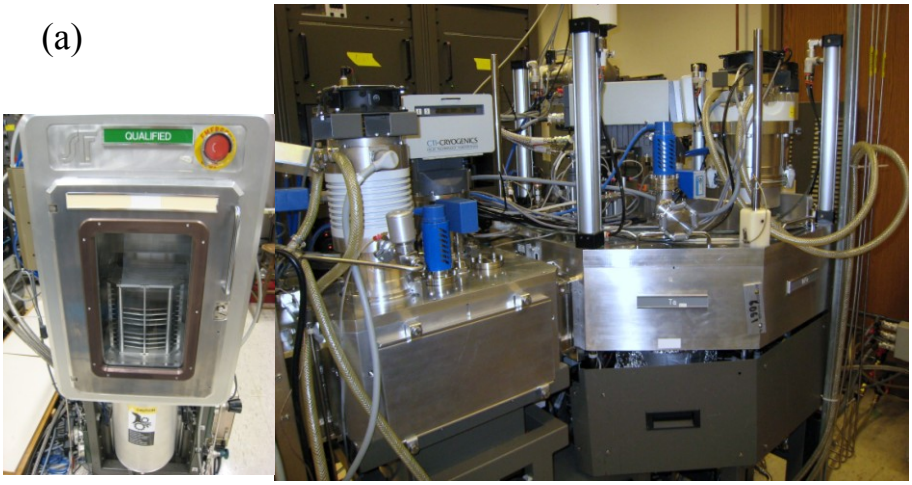

(b)

Fig. 2.2 (a) Picture of the Shamrock sputtering system at the University of Minnesota. (b) Picture of the TIMARIS sputtering system in Singulus.

The MTJ multilayer deposition is a quite complicated project. Many factors have to be carefully examined and controlled. For example, the most crucial layer is the MgO tunneling barrier, which is only around 1 nm thick. Therefore, the roughness of the bottom FM layer must be kept as low as possible in order to avoid pin holes and lattice defects in the barrier. In addition, good quality MgO layer must have a (002) texture with its [100] axis aligned with the [110] axis of the bottom and top FM layer (usually CoFeB

or Fe). The optimization of underlayer condition and sputtering condition is thus crucial. Fig. 2.3 shows an example of the (002) MgO peak measured by X-Ray micro-diffraction.

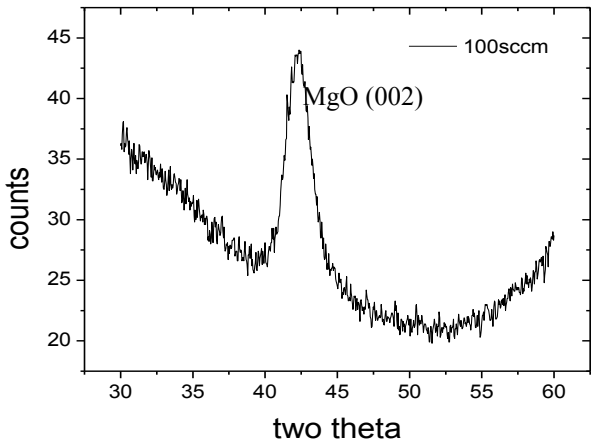

Fig. 2.3 MgO (002) peak measured by X-ray diffraction θ-2θ scan. Sample structure is Si/SiO_2 (100 nm)/MgO (12.5 nm).

2.2 Post annealing process

For the classic CoFeB/MgO/CoFeB MTJ structure deposited at room temperature, the CoFeB is amorphous and MgO is partially textured. Post annealing is required in order to get fully textured CoFeB(001)/MgO(001)/CoFeB(001) films. It can be done before or after the nanofabrication process. The CoFeB crystallization from the MgO interface starts at the temperature of 250 ºC. Another purpose of the post annealing is to get the exchange bias in the pinned layer, which means the sample has to be cooled down under magnetic field. In this work, without special annotation, we usually post anneal the sample for 2 hours at 300 ºC under 1Tesla magnetic field.

Fig. 2.4 shows the picture of the annealing system in University of Minnesota. The annealing is done inside a small glass vacuum tube to avoid oxidation. A Pfeiffer mini

turbo vacuum pumping station (TSH 071E) is used to keep the vacuum in the 10^{-7} Torr range. The sample is attached to the copper heating block by the thermal conducting grease. It is heated up by a light bulb inside the copper heating block. The annealing process is controlled by a proportional-integral-derivative (PID) multi-step temperature controller (Omega CN 7263).

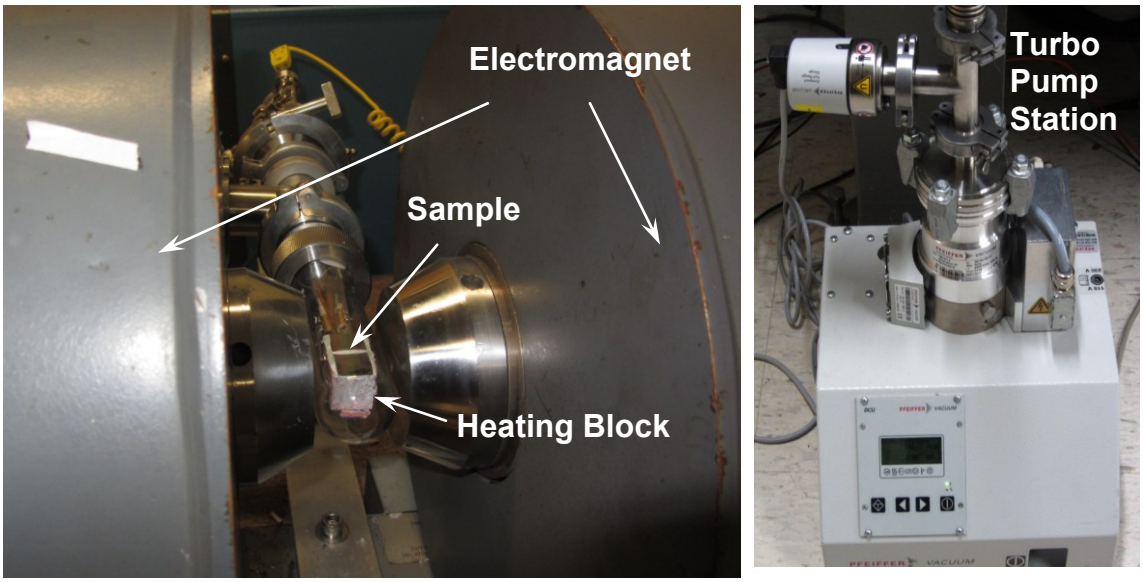

Fig. 2.4 Post annealing setup in University of Minnesota.

2.3 Nano-size magnetic tunnel junction fabrication

In this section, I will introduce the basic patterning flow used in University of Minnesota for stand-alone MTJ device fabrication.

The whole patterning flow is illustrated in Fig. 2.5 followed by a 3D view of the final device. It includes four main parts: (1) bottom electrode definition (Step 1-4); (2) MTJ pillar definition (step 5-7); (3) Planarization (step 8-10); (4) via open and electrode deposition (step 11-15). Each step is briefly introduced as follows:

Step (1): Deposite a thick Au layer (~100 nm) on top of the MTJ structure for extra protection during the lithography process. A thin Ta (~5-10 nm) layer is usually added underneath Au layer for a better adhesion between Au and MTJ stack.

Step (2): Use photo-lithography to define the bottom electrode shape. The photo-lithography process consists of the following steps: wafer cleaning, pre-bake, HDMS vapor, resist coating, soft bake, UV exposure; resist development and hard bake. Positive photo resist is used in all of our photo-lithography process for better resolution.

Step (3): Etch the bottom electrode by ion mill. The mechanism of ion mill is similar to sputtering. Ion beam is generated by the ion gun, accelerated by electrical field and finally bombards on the wafer surface. Here, the photo resist functions as the etch mask. Any surface without photo resist coverage will be etched. There are two key parameters to adjust during the ion mill process: ion bombardment angle and energy. The bombardment angle defines the final side wall slope and the possibility of material re-deposition. Large angle results in a sharp side wall slope, but may cause severe material re-deposition on the side wall. Small angle gives shallower slope and has less possibility of side wall re-deposition. In this step, a 30° etching angle is used since the feature size of bottom electrode is not critical. The bombardment energy can be controlled by ion beam power and acceleration voltage. If the energy is too high, severe side wall damage will happen during the physical bombardment. If the energy is too low, the etching rate is too low and may lead to more re-deposition. During the etching process, it is also important to monitor the wafer temperature in order to avoid photo resist over burn. We divide the whole etching process into subsections and leave 3 min cooling time between

every 3 min etching time. The end point is decided by checking a reference sample in our system.

Step (4): Photo resist cleaning.

Step (5): E-beam lithography and Ti hard mask deposition. This step defines the MTJ nano-pillar size and shape. E-beam lithography has similar procedure as photo lithography except that the exposure is done by electrical beam instead of the UV light source. In this recipe, bi-layer PMMA e-beam resist is used: 160 nm PMMA 495K A4 in the bottom and 120 nm PMMA 950K C2 on the top. The bottom resist layer (495K A4) has higher sensitivity to the e-beam dose compared to the top resist layer (950K C2). The exposure is done by Raith 150 with its maximum 30 kV beam accelerate voltage. Relative small aperture (10 μm) is chosen in order to get enough depth of focus (~10 μm) to work over the whole 4 inch wafer area. The working distance is around 10.3 mm. 200~300 uAs/cm^2 exposure dose is used. After the exposure and development, an undercut structure will form in the bi-layer resist due to different e-beam dose sensitivity of the two resists (smaller opening in top resist and wider opening in bottom resist as shown in the figure). A layer of Ti (~ 60 nm, depends on the MTJ nano pillar thickness) is then deposited on top of the resist by e-beam evaporation. The undercut structure ensures minimum side wall coverage during Ti evaporation and it helps the next lift-off process.

Step (6): Ti lift-off. This lift-off is done by soaking the sample in acetone and sonicating for 30 mins. All the Ti material on top of e-beam resist will be removed and only the

nano size Ti pillar in the central hole will be kept. It will be used as the hard mask in the next ion mill step.

Step (7): Etch MTJ nano pillar. This step is crucial for the final MTJ device quality. Multi-angle etching is chosen in order to get a sharp side wall without much re-deposition and material damage. 70º-80º angle is used in the first step for a sharp side wall profile and 20º-30º angle is used in the second step for the re-deposition cleaning. The etching time of the second step is about 10%-20% of the first step.

Step (8-10): The purpose of these three steps is to cover the bottom electrode with oxide and leave the top electrode open. Planarization and etch back technique is used here. First, the etched pillar is covered by SiO_2. This step is done by plasma enhanced chemical vapor deposition (PECVD). Second, photo resist is applied by spin-coating. Since the photo resist is much thicker (~400 nm) than the nano size SiO_2 bump, the top surface of the photo resist will be flat. Please note we use photo resist 1805 as the planarization chemical. It works well in this project for the nano pillar area. Other special planarization chemical is available on market to meet higher requirements. In step (10), the photo resist and SiO_2 are etched together by reactive ion etching (RIE). The etch rate of photo resist and SiO_2 are similar (28 nm/s) in our etching condition. Therefore, the top electrode will be exposed after the etch back process.

Step (11): 2^{nd} photo lithography for bottom electrode via open.

Step (12): Via open by RIE.

Step (13): Resist cleaning.

Step (14): 3^{rd} photo lithography for top and bottom electrode deposition.

Step (15): Deposite electrode layer by sputtering and lift-off. The electrode can be made of Ta 5 nm/Cu 100nm/Ta 20nm or Ta 5 nm/Au 100 nm.

Finally, the schematic picture of a 3D MTJ device is shown in the end of Fig. 2.5.

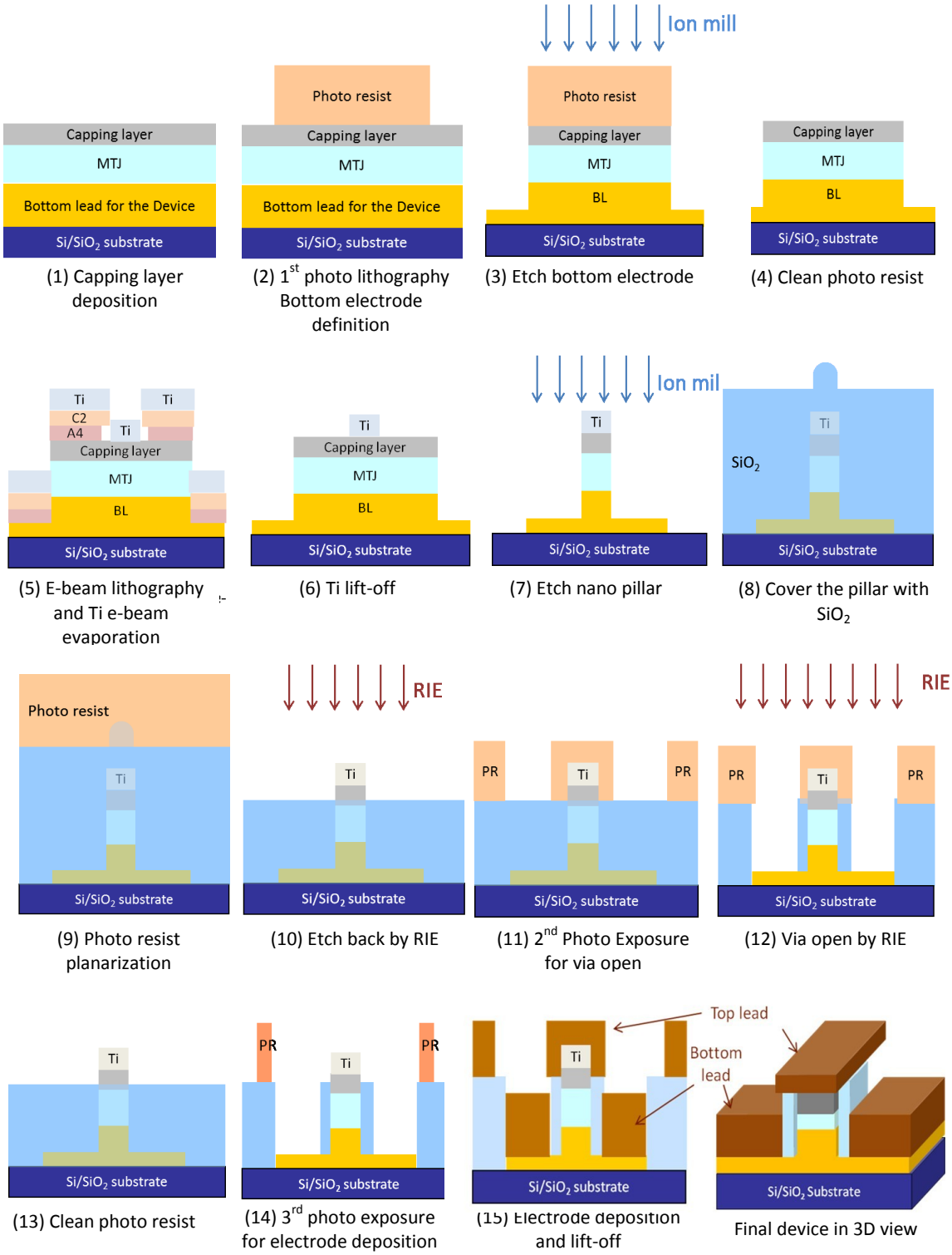

Fig. 2.5 Nano-size MTJ patterning flow and the final device 3D view.

Fig. 2.6 (a) shows the photomask design we used for MTJ device patterning on a 4 inch wafer. Every single MTJ device has the co-planar waveguide shape electrode as shown in Fig. 2.6 (b). Fig. 2.6 (c) and (d) are two SEM images of a single MTJ pillar.

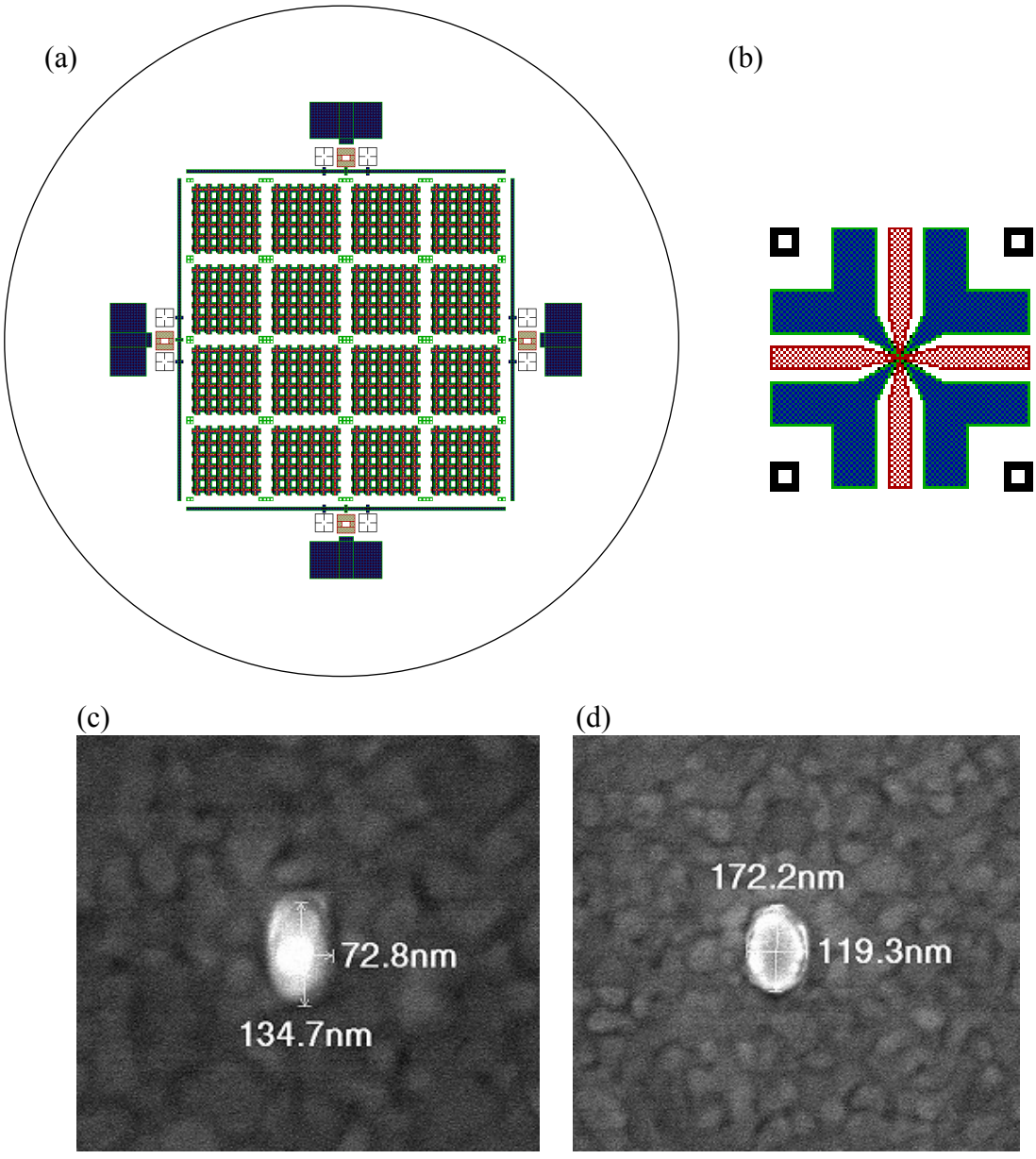

Fig. 2.6 (a) MTJ patterning mask on a 4 inch wafer. (b) Single MTJ device electrode layout. (c) and (d) SEM image of the Ti hard mask for MTJ pillar etching.

2.4 Magnetoresistance measurement setup

The resistance of MTJ device is characterized by four-probe method as shown in Fig. 2.7(a). The current is applied on one side of the electrodes and voltage is measured on another side of the electrodes. We use Cascade's DC probe and RF probe for the testing. The DC probe is a simple tungsten-rhenium needle. The RF probe is designed as air coplanar waveguide with three contacts standing for Ground Source and Ground (GSG). The model we used (ACP40) has the bandwidth of DC to 40 GHz.

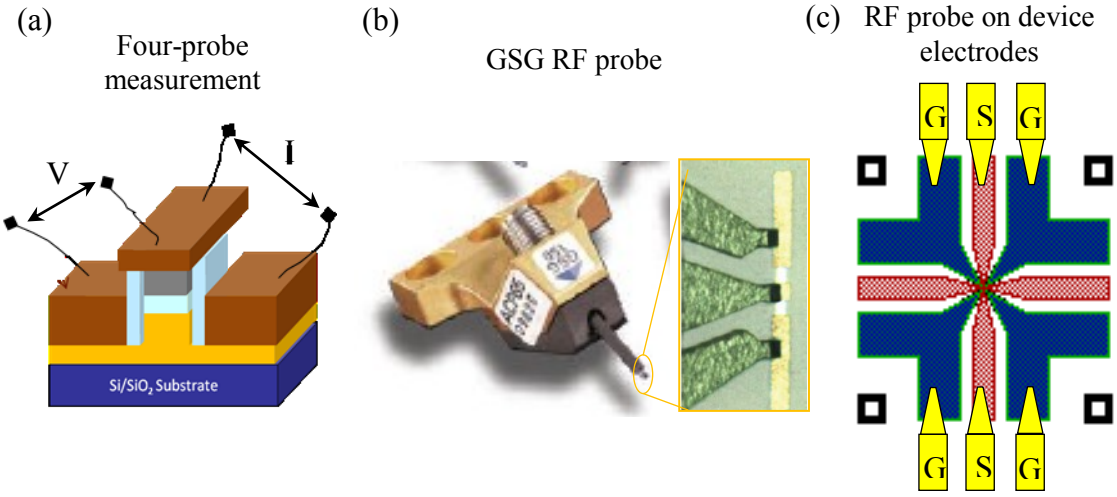

Fig. 2.7 (a) Schematic picture of the four-probe measurement method. (b) Cascade GSG probe. (c) GSG probes on our co-planar wave guide shape electrodes.

The TMR ratio is measured by testing the device resistance as a function of magnetic field. Fig. 2.8 (a) shows a typical resistance-field (R-H) loop. The parallel state resistance is 859 Ω, and anti-parallel resistance is 2018 Ω. TMR ratio is 135%. In this sample, the free layer coercivity is 48 Oe. There are three testing stages in our lab equipped with different electromagnets (Fig. 2.8 (b), (c) and (d)). The home build magnetic coils stage can supply a maximum of 220 Oe (without iron core) and 780 Oe (with iron core) in-

plane field. This stage can also use an alternative perpendicular magnetic coil with 1800 Oe maximum field. The 3D projected magnet can apply the maximum field of 3000 Oe and 2000 Oe in the in-plane direction and perpendicular direction, respectively. The big electromagnet can generate 4000 Oe maximum field with rotational sample holder. The resistance of the MTJ is measured by Keithley 2182, Keithley 6221 or Keithley 2400. All the measurements are done in computer controlled program written by Labview.

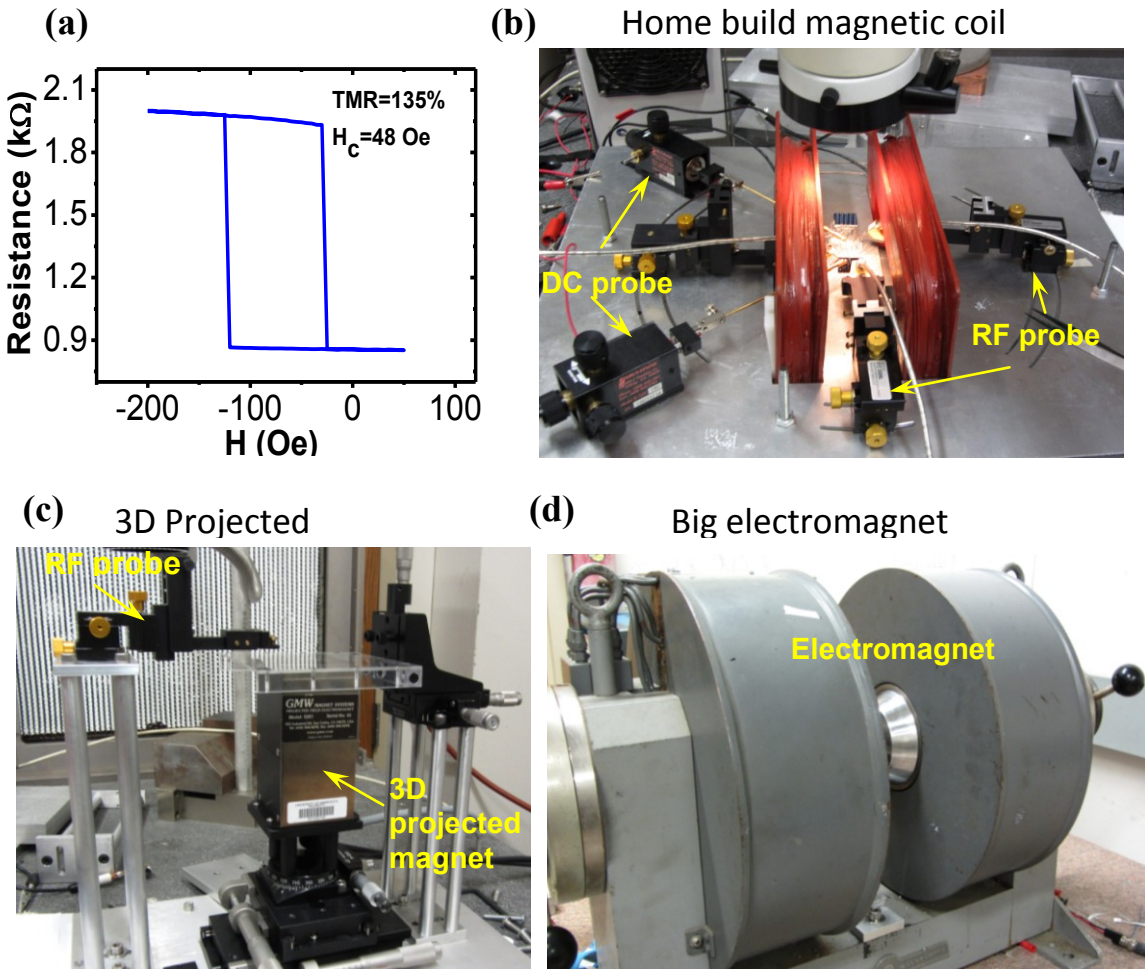

Fig. 2.8 (a) A typical resistance versus magnetic field loop measured from an in-plane MTJ. (b) Home build magnetic coils testing stage. (b) 3D projected magnet testing stage. (d) Big electromagnet testing stage.

3 Magnetic tunnel junction development for spin transfer torque induced switching

3.1 Magnetic tunnel junction device optimization

In the following three sections, I will talk about my work on the in-plane MTJ device optimization for STT-RAM application, including MgO barrier thickness, MTJ pillar size and CoFeB free layer thickness.

3.1.1 MgO barrier thickness

The resistance of the MTJ device can be calculated from the electrical tunneling effect through a potential barrier in quantum mechanics. According to Simmon's model[61], the tunneling current is

$$I = k_0 k_1 \frac{AV\sqrt{\phi}}{2t} \exp\left(-k_1 t\sqrt{\phi}\right)$$
$$k_0 = \frac{e^2}{2\pi h}, \qquad k_1 = \frac{4\pi\sqrt{2m_e}}{h}\sqrt{e} \tag{3.1}$$

where A is the device area size, t is the barrier thickness V is the applied voltage and ϕ is the barrier height. As a result, the resistance area product of the device is

$$R \cdot A = \frac{V}{I} \cdot A = \frac{2t}{k_0 k_1 \sqrt{\phi}} \exp\left(k_1 t\sqrt{\phi}\right) \tag{3.2}$$

It means the resistance area product (RA product) is a constant with the same barrier thickness and barrier height. Furthermore, since $\exp\left(k_1 t\sqrt{\phi}\right)$ is the dominant term on the right side of Eq. (3.2), the RA product increases exponentially with the battier thickness. Fig 3.1 (a) shows the antiparallel state and parallel state RA products as a function of the barrier thickness measured in our sample. The exponential increasing of RA product with

the barrier thickness is clearly stated here. For the MgO thickness below 0.8 nm, the RA product starts to deviate below the exponential prediction line. It is because that the barrier potential height starts to decrease as a result of the pinholes in the ultrathin MgO layer. Pinholes are the non-continuous regions in the oxide layer. They can come from impurities or crystal defects in the material and are the main detrimental factor to the barrier quality. It will not only affect the RA product, but also the TMR ratio. Fig 3.1 (b) shows the TMR ratio as a function of the barrier thickness. The TMR ratio starts to decrease dramatically when the MgO thickness is below 0.8 nm.

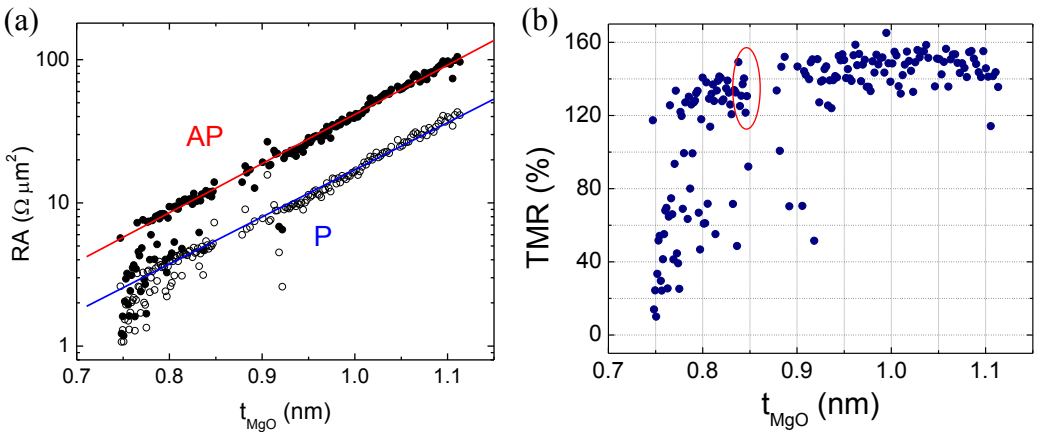

Fig 3.1 (a) RA product as a function of the MgO thickness. The black circles are the antiparallel state RA product and the open circles are the parallel state RA product. The solid lines are the fitting exponential function. (b) TMR ratio as a function of the MgO thickness. The red circle means the desired region of MgO thickness. The MTJ size of both figures are 50nm ×110nm.

For the STT-RAM application, small RA product is favored for two reasons: saving writing energy and better barrier endurance. Assuming the critical current density is constant, the smaller the RA product means lower writing voltage. Therefore, the writing process cost less energy, and it can also operate away from the high voltage stress region.

The writing energy is defined as $E_w = V^2 t/R$, where V is the writing energy, t is the pulse width and R is the device resistance. Fig 3.2 shows the writing energy as a function of the RA product in our sample[62]. In order to avoid the pinhole effect, we choose the MgO barrier thickness around 0.85 nm and the parallel RA product is around 3.0 Ω μm^2.

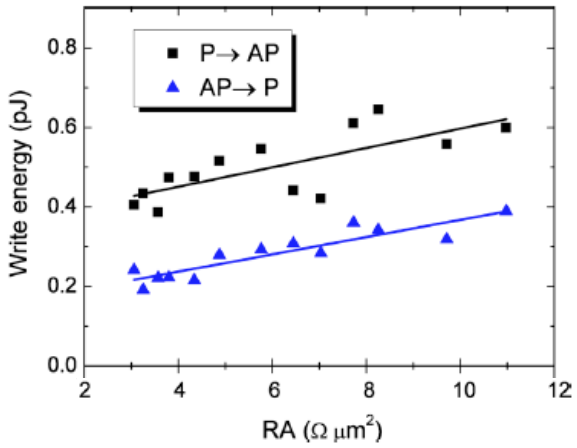

Fig 3.2 The writing energy as a function of the parallel state RA product. MTJ size is 65 nm*135 nm. Figure from Ref. 62.

3.1.2 MTJ pillar shape and size

MTJ pillar size is related to the thermal stability factor as shown in Eq. (1.9) and Eq. (1.10). For the in-plane MTJ, where the energy barrier is from the shape anisotropy, the in-plane shape anisotropy field $H_{\|k}$ is determined by the aspect ratio of the pillar's long axis and short axis. The $H_{\|k}$ value will also affect the intrinsic critical current and the thermal stability factor, as shown in Eq. (1.4) and Eq.(1.9). It is a trade-off between critical current and thermal stability factor. Therefore, the aspect ratio of the long axis and short axis should also be adjusted in the in-plane MTJs for the STT-RAM application. The measured results of the writing energy and thermal stability factor in

different size in-plane MTJs are summarized in Fig. 3.3. Depending on the requirement of the data retention time, the MTJ pillar shape and size can be chosen accordingly.

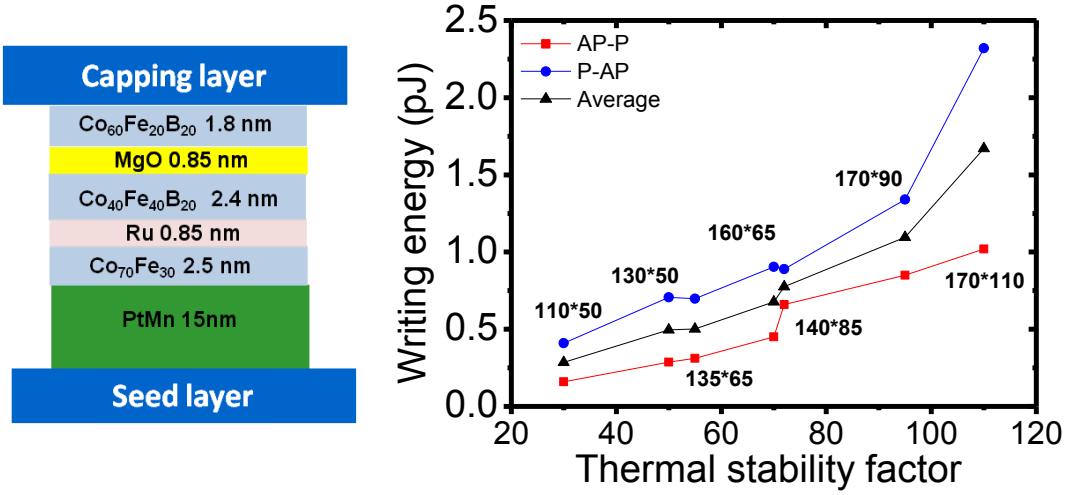

Fig. 3.3 Left: MTJ stack structure. Right: the measured writing energy and thermal stability factor in different size MTJs.

3.1.3 CoFeB free layer thickness

The CoFeB free layer thickness is also checked. According to Eq. (1.4) and Eq. (1.5), I_{c0} is proportional to the free layer volume V. Therefore, the zero temperature writing energy should decrease with the square of the free layer thickness (t_{free}^2) in theory. Meanwhile, the thermal stability factor only decreases linearly with the free layer thickness t_{free}. It means when the thermal stability factor is still acceptable, reducing the free layer thickness helps a lot in saving the writing energy. The measured writing energy as a function of the free layer thickness is shown in Fig. 3.4. The purple dash line represents the theoretical prediction of writing energy $\propto t_{free}^2$. In experiment, the writing energy decreases even faster for two reasons. First, the measurement is done at room temperature. Therefore, the measured writing energy will be further reduced from

thermal fluctuations. This reduction is stronger at the thinner CoFeB end due to its smaller thermal stability factor (Eq.(1.6)). Second, there is an extra benefit from the interface perpendicular anisotropy as the CoFeB layer goes thinner. I will talk about this effect in Chapter 3.2.2.

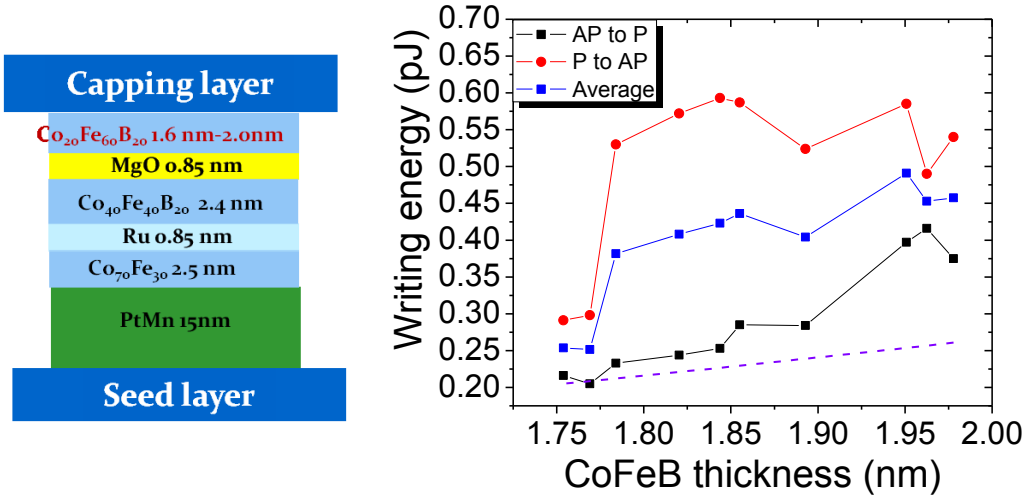

Fig. 3.4 Left: MTJ stack structure. Right: the measured writing energy as a function of the free layer thickness. MTJ size 50 nm*150 nm.

3.2 Perpendicular anisotropy in magnetic tunnel junction

There are two main advantages of the perpendicular anisotropy in MTJ for the STT-RAM application. First, the magnetic anisotropy of in-plane MTJ comes from the shape anisotropy. $K_{\|k}$ is only in the order of 10^5 erg/cm^3. When further shrinking the pillar size to sub 50 nm, it could not keep a high enough thermal stability factor for the nonvolatile requirement. While for the perpendicular MTJ, the perpendicular anisotropy can come from the crystal anisotropy. In this case, $K_{\perp k}$ can easily go to the order of 10^7 erg/cm^3. Scaling the MTJ pillar size down to sub 50 nm is possible. Another potential advantage

of the perpendicular anisotropy is that its intrinsic critical current and thermal stability factor are both directly proportional to $H_{\perp k} - 4\pi M_s$ under zero applied field (as shown in Eq. (1.4) and Eq.(1.10). On the other hand, for the in-plane MTJ, its intrinsic critical current is proportional to $H_{\|k} + 2\pi M_s$ under zero applied field, and its thermal stability is proportional to $H_{\|k}$ (as shown in Eq. (1.5) and Eq. (1.9)). Therefore, for the in-plane MTJ, the current must overcome the additional factor of $2\pi M_s$ that does not contribute to the thermal stability. The perpendicular anisotropy MTJ is thus favored for the saving writing energy and maintaining thermal stability trade-off.

In the following two sections, I will introduce my two work on the perpendicular magnetic anisotropy for MTJs: $L1_0$ phase FePd and interface perpendicular anisotropy in CoFeB.

3.2.1 $L1_0$ phase FePd

The first material I tried is the $L1_0$ phase FePd. The unit cell of the $L1_0$ FePd is shown in Fig. 3.5. It has an fct lattice structure with suppressed *c* axis. The Fe and Pd atoms are ordered in the layer by layer position. Other $L1_0$ family ferromagnetic material includes the CoPt, FePt, FePd and MnAl alloys. As we can tell from the asymmetry of its lattice structure, the $L1_0$ phase ferromagnetic material has the uniaxial magnetocrystalline anisotropy along the "easy" c axis. The anisotropy constant is reported in the range of 10^7 erg/cm^3 [63,64]. Another great advantage of some

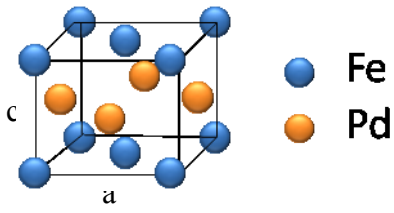

Fig. 3.5 Unit cell of the $L1_0$ phase FePd.

$L1_0$ family ferromagnetic material (FePt, FePd and CoPt) is the small lattice mismatch (~8-9%) with MTJ barrier material fcc MgO. They can be grown epitaxially on the MgO layer with the crystallographic relationship MgO(002)[100]//FePd(001)[100][65]. Furthermore, they can also be grown with the same epitaxial relationship on the $L1_0$ phase AFM material PtMn (~3-4% mismatch) for the exchange bias[66]. Therefore, they are very good candidates to be use as the perpendicular ferromagnetic layer in MgO MTJ. Among FePt, FePd and CoPt, FePd has the lowest ordering temperature. It is thus chosen here.

The full pseudo perpendicular MTJ is designed to be MgO substrate/CrRu/FePd/MgO/FePd/Capping. In this work, I started from fabricating the top ferromagnetic electrode and bottom ferromagnetic electrode separately. The top electrode is simply MgO substrate/FePd. The bottom electrode is designed as MgO substrate/CrRu/FePd. Here CrRu is used as the seed layer for the (001) FePd texture, as well as the conducting electrode for the TMR testing. It was reported that the FePt fct-(001) texture can be heteroepitaxially grown on Cr by Cr(002)[110]//FePt(001)[100][67]. Since the length of the Cr [110] axis and FePt [100] axis is 0.412 nm and 0.386 nm respectively, there will be a tensile stress on the FePt *a* axis. This stress helps to expand the *a* axis and contract the *c* axis of FePt, and thus it can reduce the chemical ordering temperature. By doping Ru into Cr (0-14% at.), the lattice constant of Cr will be expanded and it can further enhance this strain-induced fct phase formation until the epitaxial relationship fails. The optimum composition of Ru is 9.0% (at.) according to Xu

et al in their glass/CrRu/FePt films[67]. We can use the same principle here since the lattice constant of FePd *a* axis is almost the same as FePt.

The films were deposited by DC magnetron sputtering in the Shamrock system with the base pressure of 3×10^{-8} Torr. The Fe and Pd were sputtered from two separate guns at the same time with the sample rotating between each other at a speed of 33 RPM. The sputtering power of Fe and Pd were 150 W and 60 W respectively. The Cr and Ru were deposited in the same way. The sputtering power of Cr is fixed at 324 W. For Ru, I varied the power from 20 W to 85 W and found the best condition is at 55 W. After deposition, the samples were post-annealed at 410 °C in vacuum for 1 hour.

Fig. 3.6 shows the X-ray diffraction (XRD) result of the measured Cr (002) peaks. It is clear that the peak shifts to the left as the Ru sputtering power increases, which indicates the expanding of Cr lattice constant. The (001) peak of (002) peak of the FePd were measured by X-ray Microdiffraction meter. The best results of the top electrode sample (MgO substrate/FePd) and the bottom electrode sample (MgO substrate/CrRu/FePd) were plotted in Fig. 3.7 (a). The chemical ordering parameter S can be evaluated from the ratio

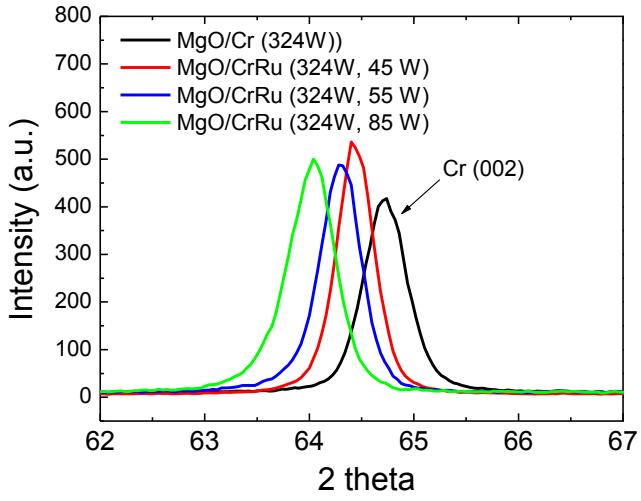

Fig. 3.6 XRD θ-2θ scanning results of the Cr (002) peak in a group of CrRu samples.

of (001) peak/(002) peak. S is defined as n_{Fe}(Fe) – n_{Pd}(Fe), where n_A(B) is the concentration of the species A on a nominal B sublattice[68]. By integrating the two peaks, the ordering parameter S is calculated to be 0.43 and 0.54 for the top electrode sample and bottom electrode sample respectively.

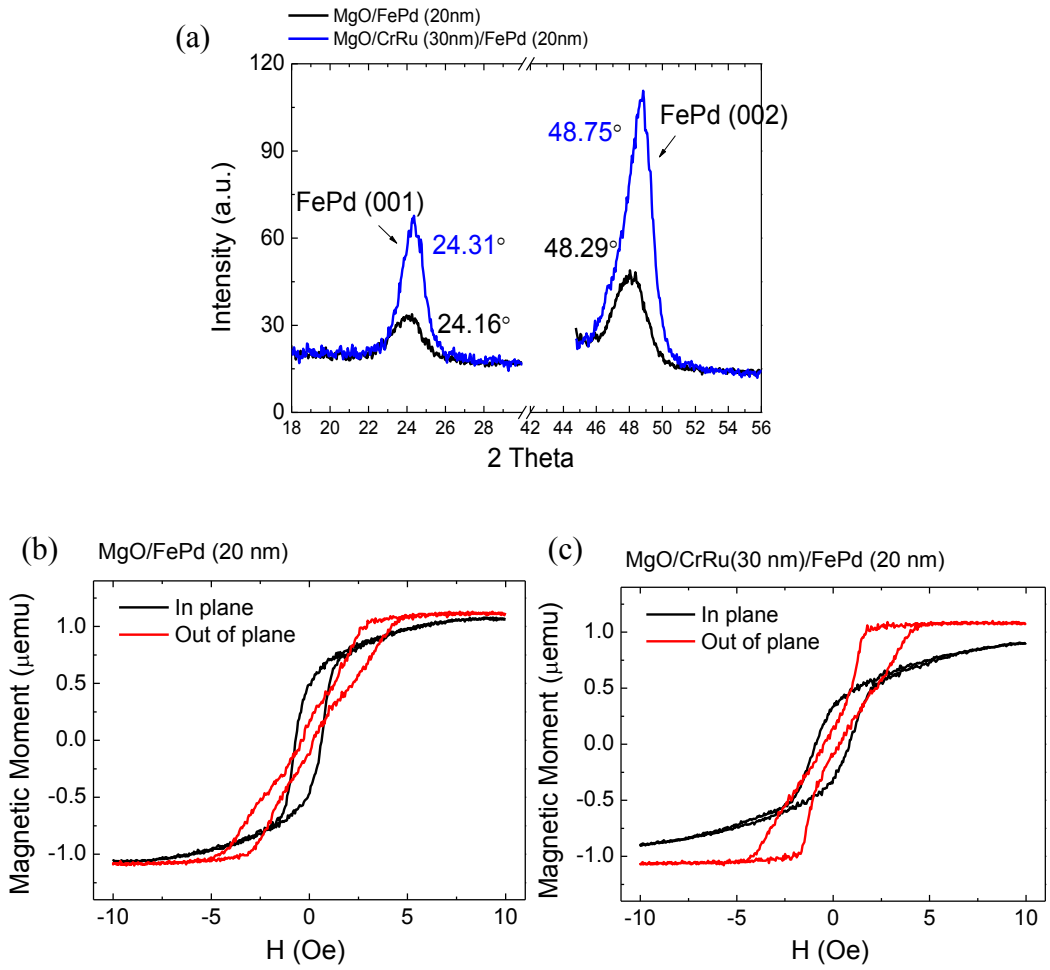

Fig. 3.7 (a) X-ray Microdiffraction results of the FePd (001) peak of FePd (002) peak. (b) and (c), in-plane and out-of-plane magnetic hysteresis loop of the top electrode sample MgO/FePd and bottom electrode sample MgO/CrRu/FePd, respectively.

The magnetic hysteresis loops of the two samples were also measured by VSM. They were plotted in Fig. 3.7 (b) and (c). The uniaxial magnetic anisotropy energy (K_u) was determined from the difference of the area enclosed between the magnetization curves in the out-of-plane and in-plane direction, with the correction of shape anisotropy energy ($2\pi M_s^2$)[65]. For the top electrode sample, K_u=8.03×10^6 erg/cm^3, and for the bottom electrode sample, K_u=8.63×10^6 erg/cm^3. Although the measured *Ku* values in our sample

are only about half of one in the fully ordered bulk material (1.8×10^7 erg/cm^3), they are already enough for the sub 20 nm MTJ application. The work of full MTJ integration and fabrication was not continued since our nano-fabrication process hasn't been optimized for sub 20 nm MTJs.

3.2.2 CoFeB with interface perpendicular anisotropy

The second work I have done is the interface perpendicular anisotropy in CoFeB layer. CoFeB MTJ with interface perpendicular anisotropy was first reported by Ikeda *et al* in 2010[69]. They claimed the interface perpendicular anisotropy is attributed to the hybridization of the Fe 3d and O 2p electrons between the $Co_{20}Fe_{60}B$ and MgO. Since this perpendicular anisotropy is an interface effect, the equivalent bulk perpendicular anisotropy can be written as $K_{\perp k}=K_i/t$, where K_i is the interface anisotropy strength and t is the magnetic layer thickness. Therefore, the equivalent bulk perpendicular anisotropy is inversely proportional to the magnetic layer thickness. It can be enhanced by reducing the film thickness. Ikeda *et al* showed that the easy axis turns from in-plane to out-of-plane when the $Co_{20}Fe_{60}B_{20}$ layer thickness is less than 1.5 nm[69]. Although this interface perpendicular anisotropy is not as large as the $L1_0$ phase magnetocrystalline anisotropy, it has the best compatibility with the current in-plane CoFeB MgO MTJ structure. Minimum material modification is required. Therefore, we also started our work on the CoFeB-MgO interface perpendicular anisotropy and successfully applied it to our MTJs.

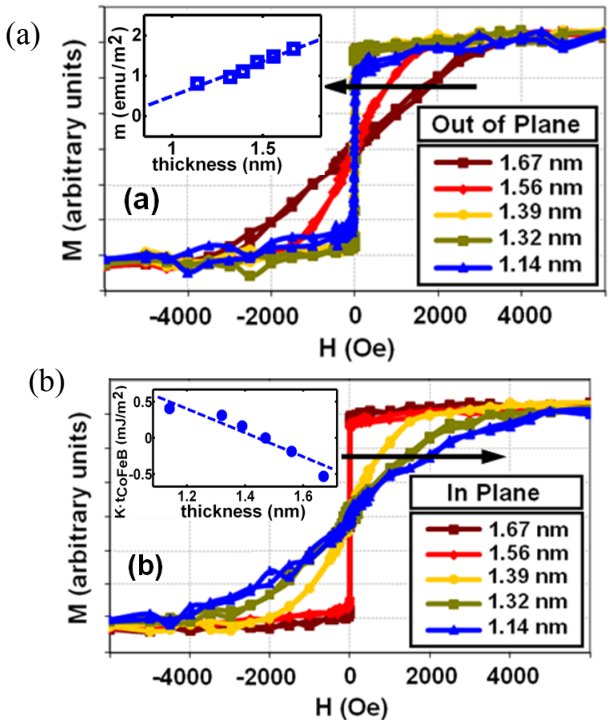

Fig. 3.8 Magnetic hysteresis loop measured by VSM in the in-plane direction (a) and out-of-plane (b) direction. Inset in (a) shows the measured magnetic moment per area as a function of the CoFeB layer thickness. Inset in (b) shows the dependence of total perpendicular anisotropy on the CoFeB layer thickness.

The material stacks were deposited in the Singulus TIMARIS sputtering system. Fig. 3.8 shows the magnetic hysteresis loop of the testing sample measured by VSM. The testing sample has the same structure as the full MTJ free layer: Ta 5nm/MgO 0.9 nm/$Co_{20}Fe_{60}B_{20}$ 1.14 nm -1.67 nm/Ta 5 nm. It is clear that we have also obtained the perpendicular anisotropy in the thinner $Co_{20}Fe_{60}B_{20}$ samples (1.14 nm, 1.32 nm, 1.39 nm). The inset in Fig. 3.8 (a) summarized the measured magnetic moment per area as a function of the $Co_{20}Fe_{60}B_{20}$ layer thickness. By extrapolating the linear fitting (dash line), we can find an approximately 0.7 nm magnetic dead layer. The inset in Fig. 3.8 (b) summarizes the measured effective perpendicular anisotropy $K_{\perp k}$ as a function of the $Co_{20}Fe_{60}B_{20}$ layer thickness. When t=1.475 nm, $K_{\perp k}$=0. The value of K_i can be fitting

from here by $K_{\perp k} = K_i / t - 2\pi M_s^2$. In our sample, K_i=1.33 erg/cm^2. Part of this work is published in *Appl. Phys. Lett.* 98, 112507, (2011)[70].

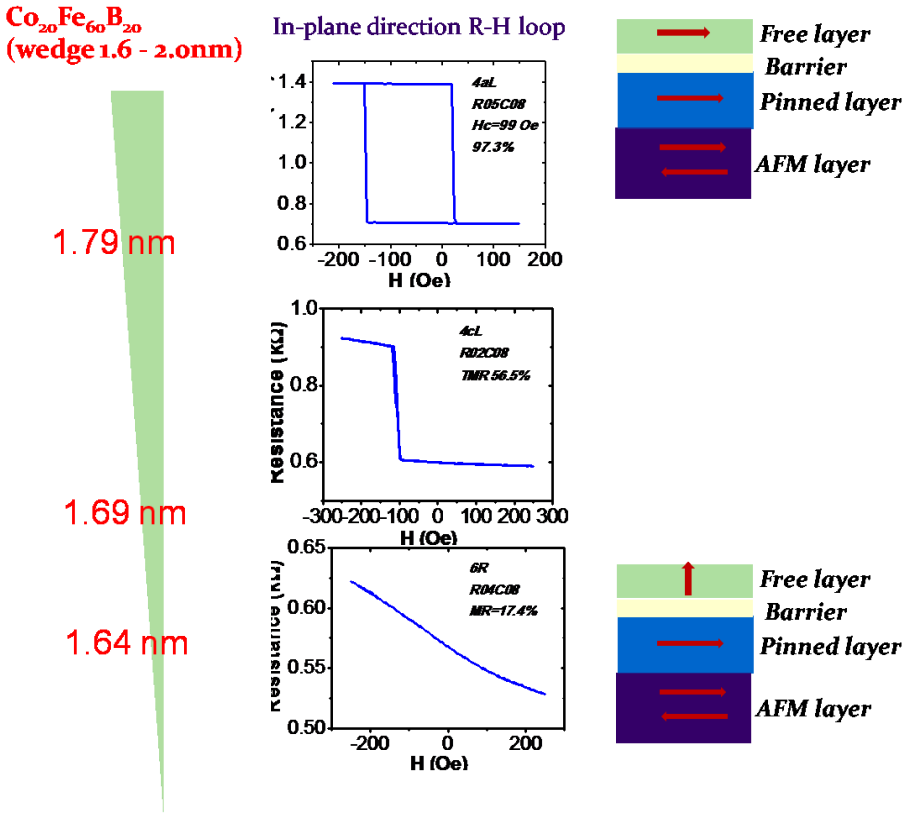

Fig. 3.9 In-plane R-H loop measured in three MTJ samples with the free layer thickness of 1.79 nm, 1.69 nm and 1.64 nm. Sample size: 50 nm *130nm.

The full MTJ device was also deposited and patterned with the structure of bottom electrode/PtMn 15 nm/CoFe 2.3 nm/Ru 0.85 nm/$Co_{40}Fe_{40}B_{20}$ 2.4 nm/MgO 0.85 nm/$Co_{20}Fe_{60}B_{20}$ (1.6 nm - 2.0 nm)/top electrode. Here the pinned layer and reference layer are still conventional in-plane MTJ structures. Fig. 3.9 shows the in-plane R-H loops measured in the patterned sample. It can be see that the in-plane R-H turns from the typical easy axis square shape to the typical hard axis linear shape as the free layer

thickness decreases. Please note although here the free layer thickness (1.64) nm is larger than the critical thickness in the thin film result (1.475 nm shown in the inset of Fig. 3.8 (b)), the interface perpendicular anisotropy still overcomes the shape anisotropy because the out-of-plane demag factor N_z is reduced in the nano size MTJ device.

Next I would like to discuss the switching current reduction effect in the in-plane MTJ as a result of the interface perpendicular anisotropy. As talked before, the dominant effect in the in-plane MTJ intrinsic critical current Eq.(1.5) is the shape anisotropy term $2\pi M_s$. When the interface perpendicular anisotropy is present, the shape anisotropy term $2\pi M_s$ can be partially canceled and thus leads to a much lower intrinsic critical current value as shown in Eq.(3.3). On the other hand, the thermal stability factor will not be affected with or without the interface perpendicular anisotropy because it is determined by the in-plane shape anisotropy field $H_{\|k} = (N_x\text{-}N_y)M_s$.

$$I_{c0} = \frac{2e\alpha M_s V(H + H_{\|k} + 2\pi M_s - H_\perp/2)}{\hbar\eta}, \quad H_\perp = \frac{2K_i}{tM_s} \tag{3.3}$$

A control experiment was done to prove the theory. From the thin film experiment, we learned that K_i can be controlled by the CoFeB composition. The iron rich $Co_{20}Fe_{60}B_{20}$ film has much larger K_i comparing to the cobalt rich $Co_{60}Fe_{20}B_{20}$ film. The intrinsic critical current density J_{c0} was thus measured in a group of two samples with the $Co_{20}Fe_{60}B_{20}$ free layer and the $Co_{60}Fe_{20}B_{20}$ free layer. The results are plotted in Fig. 3.10. For the Fe rich sample, $J_{c0\ AP\text{-}P}=1.96\times10^6$ A/cm^2, $J_{c0\ P\text{-}AP}=4.43\times10^6$ A/cm^2. For the Co rich sample, $J_{c0\ AP\text{-}P}=3.28\times10^6$ A/cm^2, $J_{c0\ P\text{-}AP}=8.86\times10^6$ A/cm^2. An average of 48% reduction in the intrinsic critical current density is found here by increasing K_i.

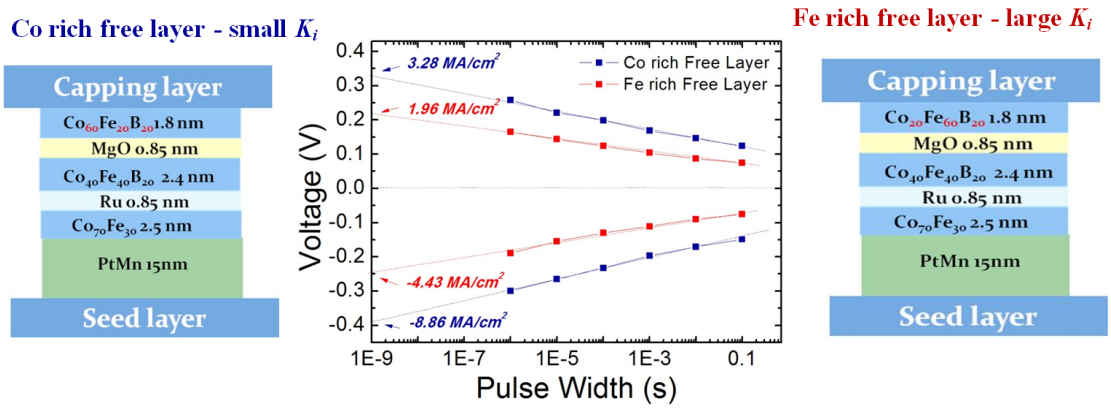

Fig. 3.10 Left and Right: the structure of the two samples. Sample size is 50nm * 130nm. Center: the measured critical switching voltage as a function of pulse width. The intrinsic critical voltage (V_{c0}) can be obtained by extrapolating the linear fitting to t=1 ns and the the intrinsic critical current is calculated from the V_{c0}/(R*A).

3.3 Summary

In summary, I have discussed my work on the MTJ material and device development for STT-RAM application. The first section mainly talks about the basic MTJ optimization. The factors of MgO barrier thickness, junction size and CoFeB free layer thickness are covered. In the second section, the advanced factor of perpendicular magnetic anisotropy is introduced. The perpendicular MTJ is favored over the conventional in-plane MTJ for its advantage in the saving writing energy and maintaining thermal stability trade-off. In my work here, $L1_0$ phase FePd is first chosen as the material to fabricate the full perpendicular MTJ. Perpendicular anisotropy is successfully developed in the $L1_0$ phase FePd top electrode and bottom electrode sample. Another system studied is the interface perpendicular anisotropy in CoF eB free layer. It is proven experimentally that by adding the interface perpendicular anisotropy to the in-plane MTJ, the critical switching current can be effectively reduced because of the partially canceled

easy plane anisotropy term $2\pi M_s$. An average of 48% reduction in the intrinsic critical current density is found here by increasing the interface perpendicular anisotropy K_i.

4 Spin transfer torque induced switching study

This chapter introduces my general study on the spin transfer torque (STT) induced switching. As discussed in Chapter 1.3, the STT induced switching is a probabilistic process at finite temperature. Therefore, my study here is based on the pulse width dependent STT induced switching probability measurement. I will discuss the three STT induced switching modes, the switching energy, the switching speed and the switching distribution based on my measurement results. In the end, the temperature dependent STT induced switching is also characterized.

4.1 Measurement setup

The working principle of the STT induced switching probability measurement is shown in Fig. 4.1. First, the MTJ is reset to its initial state (AP state for AP to P switching, or P state for P to AP switching) by applying the magnetic field or spin polarized current. Second, the switching pulse is injected. After that, the device resistance is checked to determine whether the free layer magnetization has switched or not. Cumulative switching probability is then calculated by repeating this cycle for 10^2-10^5 times in my experiment.

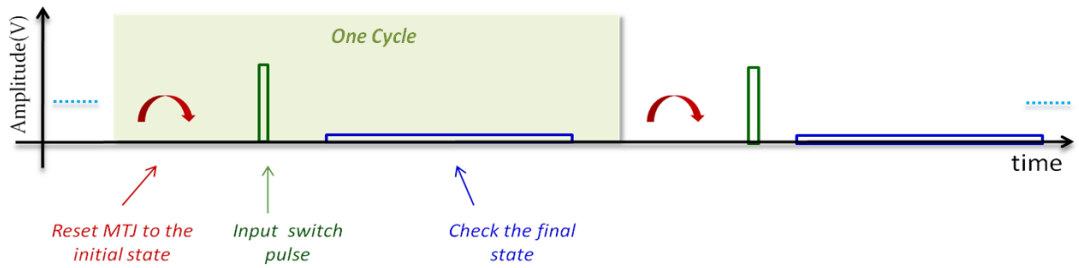

Fig. 4.1 Schematic illustration of STT induced switching probability measurement principle.

The switching probability measurement was mainly done on the home build magnetic coil stage (Fig. 2.8(b) in Chapter 2.4) with Kepco BOP 20-20 bipolar power supply. The reset pulse and switching pulse were generated from two pulse generators: HP8110A (pulse width: 10 ns-10 s) and Picosecond 10070A (pulse width: 0.1 ns-10 ns). The device resistance was measured by Keithley 2400, Kethley 6221 & Kethley 2000, or NI DAQ card PCI-6221. Bias Tee (Picosecond 5542) and power combiner (Picosecond 5331) were also used in the testing circuit. Depending on the device quality and characterization precision requirement, several different testing circuits were developed. Here I am going to introduce three main circuits.

The first one is shown in Fig. 4.2(a). It runs at relative low testing speed but can apply to a wide of range input pulse widths (10 ns-0.1s). It also applies to both the field reset case and the pulse reset case. As indicated on the figure, the reset pulse and switching pulse are generated from the two pulse generators connected by a power combiner. In the field reset case, the second pulse generator is deactivated. The resistance is read from the Kethley 2400 on the right side of the circuit through the DC port of Bias Tee. Here the Bias Tee acts as a low pass filter (cut off frequency 8 kHz). The left side and right side circuits are connected through either two GSG probes or the Tee connector. The testing time sequence is controlled by Labview program. The advantage of this circuit is the wide range of input pulse widths (10 ns-0.1s). The disadvantage is the low testing speed and not able to go down below 10 ns because of the impedance mismatch.

The second circuit is very similar to the first one, except that the Bias Tee is used to isolate the high frequency signal and low frequency signal here. The reset pulse and

(a)

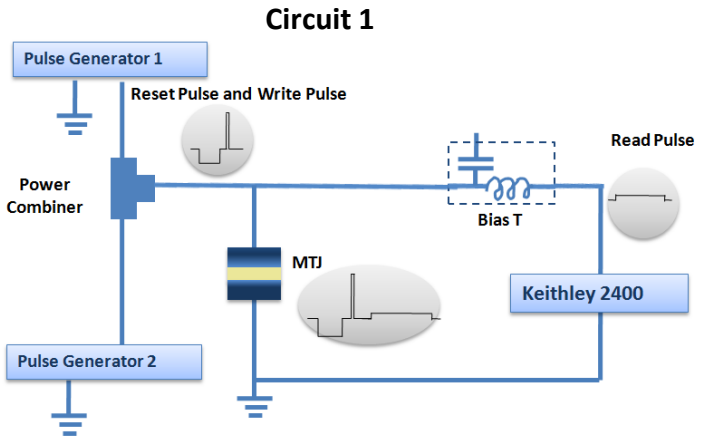

(b)

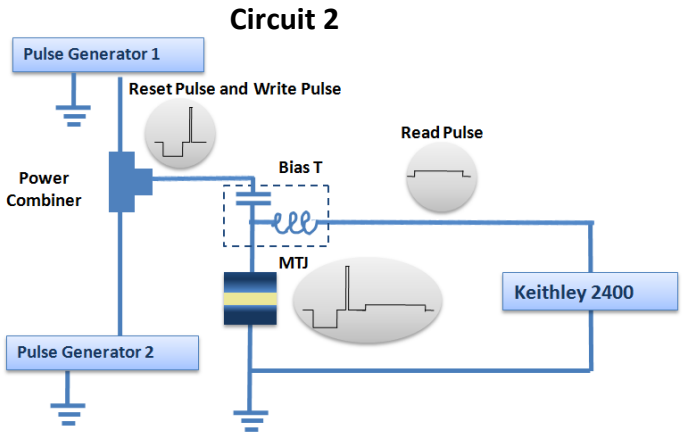

(c)

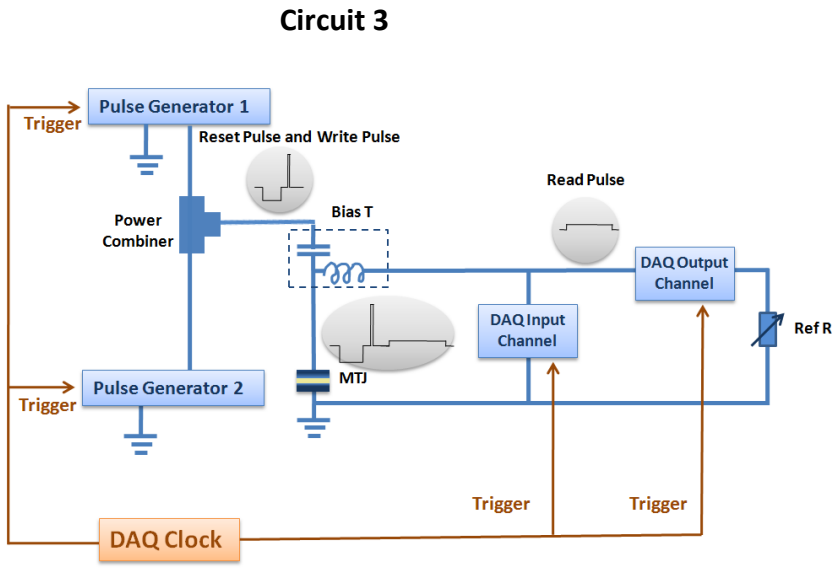

Fig. 4.2 (a), (b) and (c) STT induced switching probability measurement circuit 1, 2 and 3.

switching pulse are injected through the AC port of the Bias Tee, and the Keithley 2400 is connected to the DC port of the Bias Tee. With this modification, the input pulse width range is (100 ps – 1 μs), where the maximum pulse width is limited by the AC port cut-off frequency (3dB, 10 kHz) and the minimum pulse width is limited by the SMA connector (18 G Hz).

The third circuit is illustrated in Fig. 4.2(c). The input pulse width range is the same as the previous circuit (100 ps - 1μs). I've made two improvements. First, DAQ card is used to test the device resistance instead of the Keithley 2400. Second, all equipments are synchronized together by the DAQ clock to generate the desired arbitrary waveform sequence. Because of the synchronization, it runs at a speed of 100 cycles per second and can perform the high efficient switching probability measurement. The only drawback is that the synchronization only works for the pulse reset case, which requires higher sample quality.

The specifications of the three testing circuits are summarized in Table 4.1.

Table 4.1 Specifications of the Three Testing Circuits

	Pulse width	**Field reset**	**Pulse reset**	**Test Speed**
Circuit 1	10 ns – 0.1 s	Yes	Yes	1-5 trials per second
Circuit 2	100 ps- 1μs	Yes	Yes	1-5 trials per second
Circuit 3	100 ps- 1μs	No	Yes	100 trials per second

Another factor I would like to point out is the impedance mismatch in the circuit. All the pulse amplitude values in this work are the mean pulse voltage on device included the impedance mismatch effect. It is calculated by the following equation.

$$V_{MTJ} = (1+\Gamma)V_{in} = \left(1+\frac{R_{MTJ}-Z_0}{R_{MTJ}+Z_0}\right)V_{in} = \frac{2R_{MTJ}}{R_{MTJ}+Z_0}V_{in} \quad (4.1)$$

where Z_0 is the transmission line impedance 50 Ω.

4.2 Result and discussion

4.2.1 Three switching modes

As discussed in Chapter 1.3, there are three STT induced switching modes at different the switching pulse width regime. In this section, I am going to show my measurement on that.

The in-plane MTJ samples were prepared using the Singulus TIMARIS sputtering system with a stacking structure of (bottom electrode)/PtMn (15 nm)/$Co_{70}Fe_{30}$ (2.5 nm)/Ru(0.85 nm)/$Co_{40}Fe_{40}B_{20}$ (2.4 nm)/MgO (0.83 nm)/$Co_{60}Fe_{20}B_{20}$(1.8 nm)/(top electrode). It was postannealed at 300 ºC under 1 T magnetic field for 2 h. The wafer was then patterned into elliptical nanopillars with different sizes and aspect ratios. The results in this section and next section were measured in the same MTJ with the size of 130 × 50 nm^2.

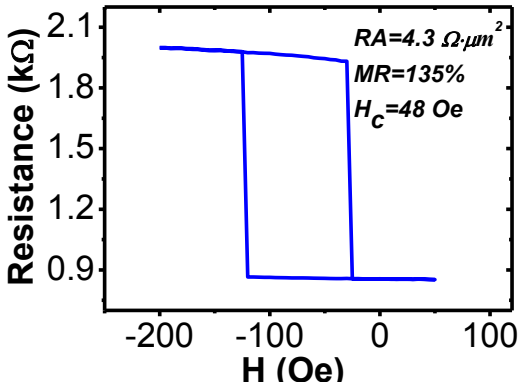

Fig. 4.3 Resistance versus magnetic field loop of a MTJ with the size of 50×130 nm^2.

Fig. 4.3 shows the R-H loop for the MTJ sample. The TMR ratio of this junction is 135%, the free layer coercivity is 48 Oe at room temperature, and the RA product at P state is 4.3 Ω μm^2. The abrupt switching in this R-H loop means the free layer acts as a single magnetic domain unit.

The switching probability measurement was done on the first circuit with the initial state reset by the magnetic field. 100 switching attempts were used for each measured switching probability data point. An external field of -75 Oe was applied during the STT induced switching process in order to compensate the free layer offset field from interlayer coupling.

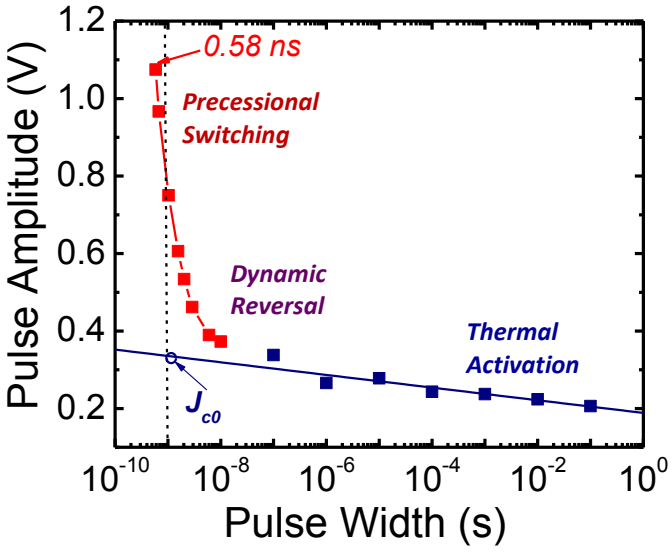

Fig. 4.4 Switching time versus pulse amplitude at 50% switching probability from 0.5 ns to 0.1 s for AP to P switching. The red and blue dots are experimental data, which follow the precessional switching model and thermal activation model, respectively. The red line and blue line is the precessional model and thermal activation model fitting curves respectively. The vertical black dotted line is the guild line of 1 ns.

Fig. 4.4 shows the measured critical switching pulse amplitude as a function of the pulse width. Each data point corresponds to the pulse amplitude and pulse width at 50%

switching probability. For short pulses (red points in the figure), the STT induced switching process is in the precessional switching mode. It is a dynamic reversal process driven by the spin momentum transfer, almost independent of the thermal agitation. The switching probability distribution is mainly caused by the initial position dispersion from thermal fluctuation. The red solid curve indicates the fitting by Eq.(1.7). J_{c0} is found to be 2.98×10^{6} A/cm^2. While for the long pulse (blue points in the figure), the STT induced switching is in the thermal activation mode, mainly driven by thermal agitation. The initial position distribution from thermal fluctuation does not make much difference on the final switching probability. The blue solid line shows the fitting according to Eq.(1.6). The thermal stability factor $\Delta(I)=K_uV/k_BT$ fitting by this method of this sample is 50. Here, J_{c0}=3.82×10^{6} A/cm^2, higher than the previous value estimated from the precessional switching mode. It is probably because the last several points in the precessional mode fitting are already in the dynamic mode. Dynamic reversal mode is an intermediate regime between the precessional mode and the thermal activation mode. The magnetization reversal is contributed by a combination of spin momentum transfer and thermal agitation. The exact boundaries of the three STT induced switching modes are difficult to determine because of this mixed dynamic reversal mode. Moreover, I believe the boundaries also differ from sample to sample as a result of different thermal stability factor. In Chapter 4.2.3, I will propose a new characterization method to define the boundaries.

4.2.2 Spin transfer torque induced switching energy and switching speed

In this section, I will show the how the STT induced switching energy (writing energy) and switching speed (writing speed) is characterized. The testing was done on Circuit 2.

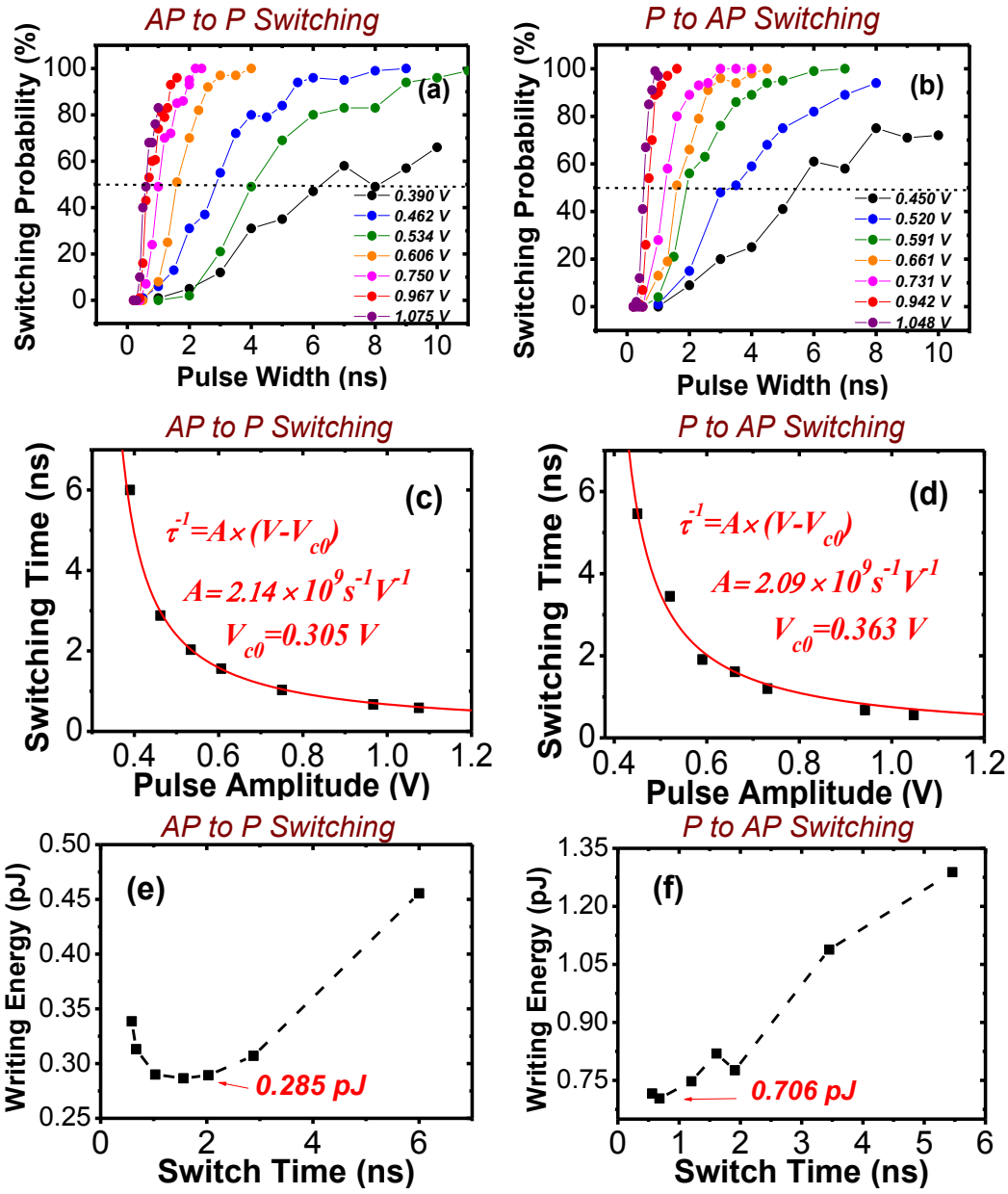

Fig. 4.5 (a) and (b) Switching probability dependence on writing pulse width of different pulse amplitude; (c) and (d) switching time versus pulse amplitude at 50% switching probability; (e) and (f) writing energy dependence on switching time.

The switching probability as a function of pulse width and pulse amplitude is shown in Fig. 4.5 (a) and (b). Both the writing energy and switching time are defined at 50% switching probability corresponding to the dashed line in the figure. From the two figures, we can see that ultrafast switching around 0.5 ns is achievable when the pulse amplitude is about 1 V (purple curve and red curve). For AP to P switching, the measured shortest writing pulse width is 580 ps at 1.075 V, and for P to AP switching, the shortest writing pulse width is 560 ps at 1.048 V. Further increase of the pulse amplitude will reduce the switching time more. However, 1 V is already close to the breakdown voltage. There is a large chance to breakdown the thin MgO barrier.

The pulse amplitude and pulse width corresponding to the 50% switching probability are plotted in Fig. 4.5 (c) and (d). In the nanosecond regime, the spin torque transfer switching is a precessional process. According to precessional mode macrospin model Eq.(1.6), the switching speed is inversely proportional to the pulse amplitude as follows:

$$\tau \propto \frac{\ln(\pi/2\theta_0)}{V_c - V_{c0}} \quad \text{or} \quad \tau^{-1} \propto A \times (V_c - V_{c0}), \quad \textit{where } A = 1/\ln(\pi/2\theta_0). \tag{4.2}$$

V_{c0} is defined as the intrinsic critical voltage analogous to the intrinsic critical current. In the figure, the red dashed curve is the fitted curve according to the above formula. We can see the data fit well with this model in the regime from 0.5 to 6 ns in both figures, which is similar to other reports[71]. The fitting parameters are $A_{ap\text{-}p}$=2.14×10^9 s^{-1} V^{-1} and $V_{c0\ ap\text{-}p}$=0.305 V for the AP to P switching, and $A_{p\text{-}ap}$=2.09×10^9 s^{-1} V^{-1} and $V_{c0\ p\text{-}ap}$=0.363 V for the P to AP switching. Those values can be converted to the intrinsic critical current and intrinsic critical current density as $I_{c0\ ap\text{-}p}$=0.152 mA, $J_{c0\ ap\text{-}p}$=2.98×10^6 A/cm^2, and $I_{c0\ p\text{-}ap}$ =0.427 mA, $J_{c0\ p\text{-}ap}$=8.37×10^6 A/cm^2.

Now we can determine the minimum AP to P writing energy for a single bit from the correlation between switching pulse voltage and pulse width. The writing energy is calculated by

$$E = V^2 \tau / R_{MTJ} \ . \tag{4.3}$$

Therefore, the writing energy equals

$$E = \frac{V^2 \tau}{R_{MTJ}} = \frac{\left(\frac{1}{A\tau} + V_{c0} \right)^2 \tau}{R_{MTJ}} . \tag{4.4}$$

It has the minimum when $\tau_{ap-p} = 1/AV_{c0\ ap\text{-}p} = 1.53\ ns$ or $\tau_{p-ap} = 1/AV_{c0\ p\text{-}ap} = 1.31\ ns$.

The measured writing energy is shown in Fig. 4.5 (e) and (f). A minimum writing energy is found at 1.56 ns for AP to P switching, and 0.68 ns for P to AP switching, which is in good agreement with the prediction. The optimal 50% switching probability writing energy is as low as 0.286 pJ for AP to P switching and 0.706 pJ for P to AP switching. This result proves that low writing energy consumption can be achieved with GHz writing rate in a simple in-plane MgO MTJ sample.

Based on the above switching probability data, we can plot the whole phase diagram of the STT switching in Fig. 4.6 (a) and (b). The switching probability distribution is shown by the color as labeled next to the figure. So in both figures, the blue color area represents a stable parallel state and red color area stands for a stable antiparallel state. Between the two areas, there is a switching probability distribution from 0% to 100%.

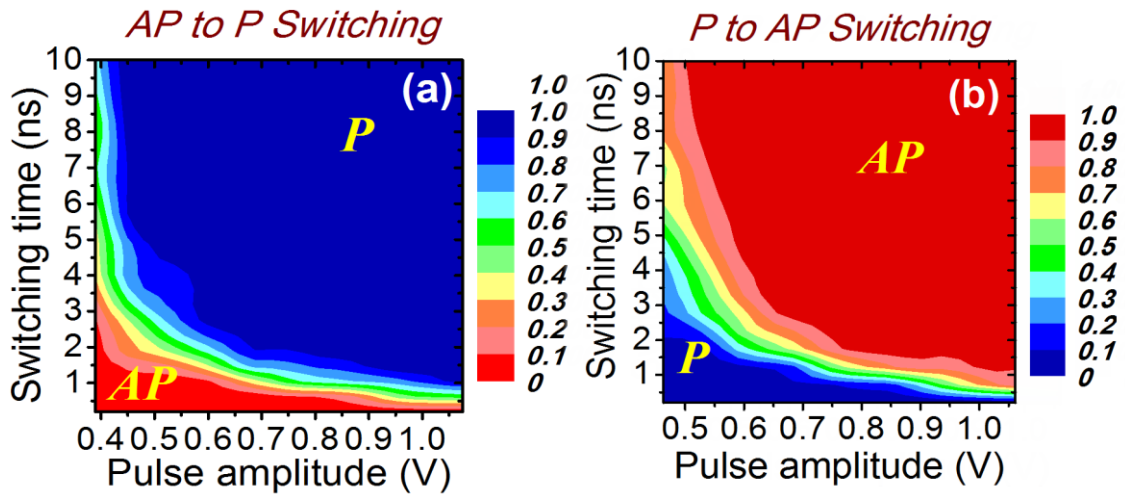

Fig. 4.6 (a) and (b) Spin torque transfer switching phase diagram in nanosecond regime.

In conclusion, the writing energy and writing speed in an in-plane MTJ were studied here. The device has the parameters of RA=4.3 Ω μm^2, TMR = 135% and thermal stability factor $\Delta(I)$=50 (by current measurement). The optimal writing energy was found to be 0.286 pJ per bit at 1.54 ns for AP to P switching, and 0.706 pJ per bit at 0.68 ns for P to AP switching. Sub ns STT switching was also observed in this sample at 580 ps (AP to P) and 560 ps (P to AP). As a result, 0.6–1.3 GHz was determined to be the optimal writing rate from writing energy consumption of view. These results show that in-plane MgO MTJs are still a viable candidate as a fast memory cell for STT-RAM. The work in Chapter 4.2.1 and Chapter 4.2.2 were published in *J. Appl. Phys.,* 109, 07C720, (2011)[72].

4.2.3 Spin transfer torque induced switching distribution

The STT induced magnetization switching distribution is one of the key factors for STT-RAM development. For functional operation, the probability that free layer switches during the low voltage read process is referred as the read disturb rate (RDR), and the

probability that the free layer does not switch under large voltage during write process is defined as write error rate (WER)[57,73]. Both of the two parameters are directly related to the distribution of switching voltage. Several studies have been done recently to understand the switching voltage distribution by analyzing the RDR, WER or the mean and variation of the switching voltage for STT-RAM application[52,74–79]. In this section, I studied the switching voltage distribution more systematically by characterizing the switching probability density function (PDF) with good statistics (10^5 trials) across a wide range of time scales from 5 ns to 1 μs. The asymmetry of PDF is discussed.

The presented measurement results are chosen from an in-plane MgO MTJ sample with the structure of (bottom electrode) / PtMn (15 nm) / $Co_{70}Fe_{30}$ (2.5 nm) / Ru (0.85 nm) / $Co_{40}Fe_{40}B_{20}$ (2.4 nm) / MgO (0.83 nm) / $Co_{20}Fe_{60}B_{20}$ (1.8 nm) / (top electrode). The thin film stack was deposited by a Singulus TIMARIS sputtering system with 2 hours post annealing at 300°C under 1 T magnetic field. The planar shape of this particular sample is a 50 nm×150 nm ellipse. The TMR ratio, RA product and room temperature coercivity are 101%, 5.2 $\Omega\cdot\mu m^2$, and 105 Oe respectively. The switching probability measurement was done on the third circuit as introduced in Chapter 4.1. The free layer shift field was canceled by an external field during the switching probability measurement in order to center the hysteresis loop.

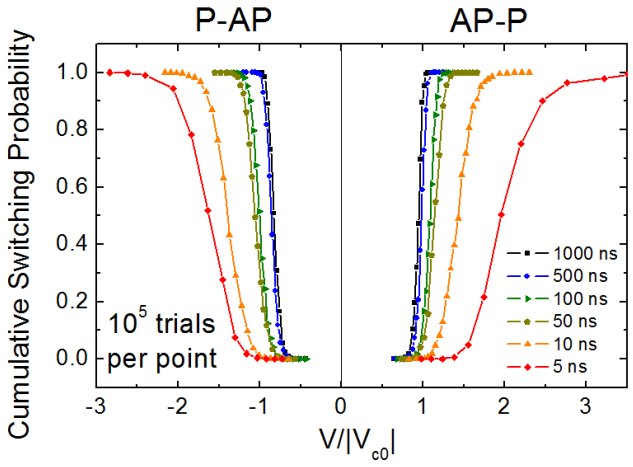

Fig. 4.7 Switching probability cumulative distribution function (CDF) from 5 ns to 1 μs with 10^5 trials per point;

Fig. 4.7 shows the measured STT switching probability cumulative distribution function (CDF) from 5 ns to 1 μs with 10^5 trials per point. Both AP to P switching and P to AP switching are characterized. The switching voltage is normalized by $V/|V_{c0}|$ in the figure, where V_{c0} is the intrinsic critical voltage fitted from the thermal activation model $V= V_{c0}[1-ln(t_p/\tau_0)/\Delta]$ in the long pulse regime (1μs-0.1s). In this sample, $V_{c0,\ AP\text{-}P}$=0.215 V and $V_{c0,\ P\text{-}AP}$=-0.273 V.

The switching PDF, defined as the derivative of the CDF, is plotted in Fig. 4.8(a). As the pulse width decreases, on both the AP-P and P-AP sides, V/V_{c0} increases gradually from below 1 to above 1. Meanwhile, the width of the switching PDF curve is broadened rapidly.

The enlarged PDF curves of P-AP switching at 1 μs and 5 ns are plotted in Fig. 4.8(b) and (c) respectively. Three distribution types are used to fit the experimental data. First, as expected, the classic STT switching distribution function (blue curves in Fig. 4.8 (b) and (c)) from thermal activation model (Eq. (4.5) [31,58,59]) can only fit the data up to V/V_{c0}

= 0.8.

$$p\left(\frac{V}{V_{c0}}\right) = \Delta \frac{t_p}{\tau_0 \exp\left(\Delta\left(1 - V/V_{c0}\right)\right)} \cdot \exp\left(\frac{-t_p}{\tau_0 \exp\left(\Delta\left(1 - V/V_{c0}\right)\right)}\right), \qquad \Delta = \frac{K_U V}{k_B T}. \tag{4.5}$$

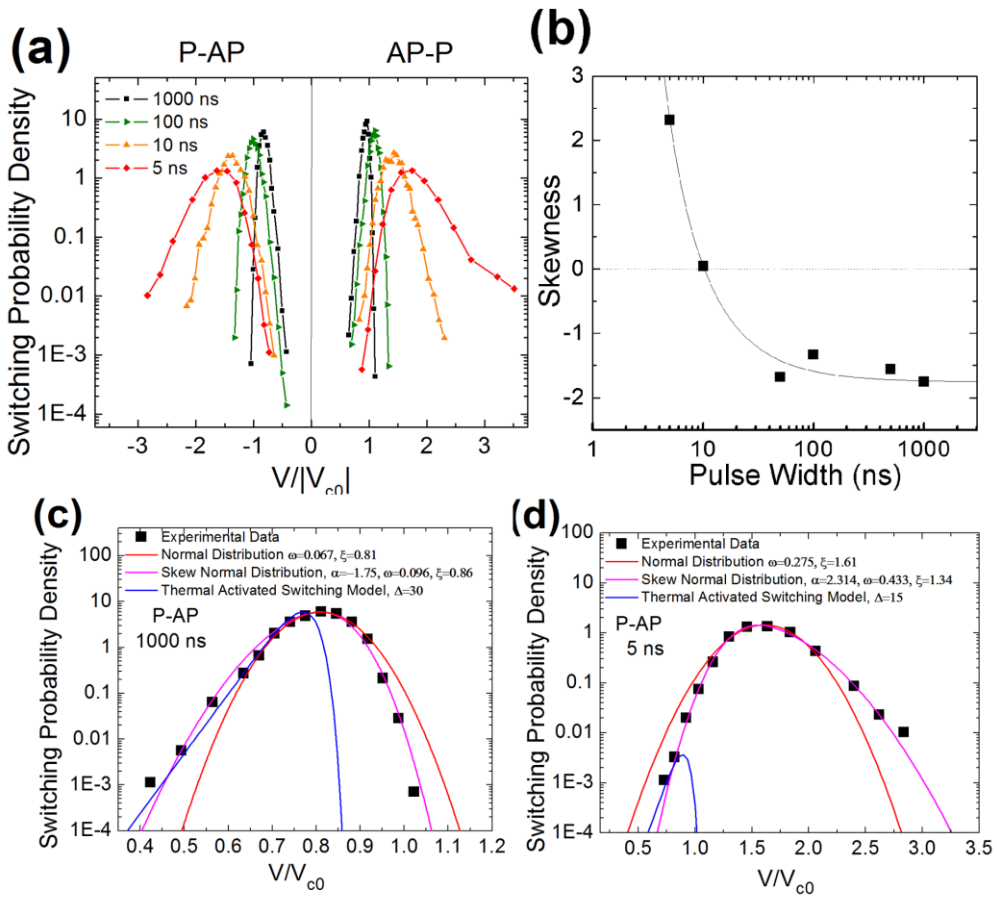

Fig. 4.8 The switching probability density function (PDF) as the derivative of the CDF in Fig. 4.7; (b) Skewness value as a function of pulse width. The symbols are the experiment data fitted from the P-AP switching PDF curves and the solid curve is the guideline; (c), (d) The PDF of P-AP switching at 1μs and 5 ns respectively. The solid lines are the fitting of normal distribution (red), skew normal distribution (pink) and thermal activation model distribution (blue). For the thermal activation model, we used the delata value from the RDR fitting in Fig. 4.9(c).

Second, by comparing to the Gaussian function (red curves in Fig. 4.8 (b) and (c)); we can see that the measured PDF curves are not symmetric. Instead, the skew normal

distribution (Eq.(4.6)) fits the experimental data quite well down to 10^{-3} in both tails (pink curves in Fig. 4.8 (b) and (c)), and the fitted α value represents the skewness of PDF asymmetry.

$$f(x)=\frac{2}{\omega}\phi\left(\frac{x-\xi}{\omega}\right)\Phi\left(\alpha\left(\frac{x-\xi}{\omega}\right)\right)$$
$$where,\ \ \phi(x)=\frac{1}{\sqrt{2\pi}}e^{-\frac{x^2}{2}},\quad \Phi(x)=\int_{-\infty}^{x}\phi(x)dt=\frac{1}{2}\left[1+erf\left(\frac{x}{\sqrt{2}}\right)\right] \tag{4.6}$$

One interesting point is that the asymmetry of PDF curves switches from left skew to right skew for 1 μs and 5 ns pulses. The same trend was observed both in AP-P and P-AP sides. I've excluded the Ohmic heating effect in our result since no obvious temperature rising (>3°C) was found in the pulsed switching probability measurement. The perpendicular spin torque term may have some effect on the switching probability distribution, but it cannot explain the asymmetric flip unless its magnitude does not have monatomic dependence on the bias voltage in both the positive or negative directions. No such experimental result has been reported yet.

Therefore, the asymmetry flip is understood as a sign of the fluctuation mechanism transition from the thermal agitation to the initial magnetization trajectory dispersion. In the thermal activation mode, the switching distribution is mainly determined by the thermal agitation during the switching process. The switching CDF follows the modified Néel-Brown relaxation theory $P=1-exp(t_p/t)$, where $t = \tau_0 exp[E_0(1-V/V_0)]$. Mathematically, the modified Néel-Brown relaxation formula has a shape that the cumulative probability converges to 1 much faster in the high voltage end than it converges to 0 in the low voltage end. Therefore, the PDF is always left skewed (the blue

curve in Fig. 4.8 (c)) as determined by Eq. (4.5). In the precessional switching mode, the switching voltage variation is mainly dependent on the magnetization dispersion the initial state. The smaller the switching voltage, the more precessional circles the switching trajectory will go through, and the more initial trajectory dispersion will be averaged out. As a result, there is less uncertainty in the low voltage end, leading to a steeper left tail in the plotted PDF figure. In other words, the PDF is right skewed. Therefore, we conclude that the switching voltage distribution comes from two fluctuation mechanisms: thermal agitation during the switching process and the initial magnetization trajectory dispersion. Since the two fluctuation mechanisms have the opposite asymmetry in the switching PDF figure, we propose to use the fitted skewness value to estimate the contribution from the two fluctuation mechanisms at certain pulse width. It is particularly useful for the dynamic reversal regime, where the STT switching depends both on the thermal agitation and the initial magnetization dispersion. According to Diao *et al*., the boundary between the dynamic reversal regime and the thermal activation regime is around 30 ns[73]. We can see that in Fig. 4.8 (b), as the pulse width increases, the skewness has a sharp drop at first, and then reaches a relative flat stage from t>50 ns. This transition point is very close to the proposed boundary. Furthermore, the PDF is symmetric (α =0) around 10 ns, corresponding to equal contributions from the two fluctuation mechanisms.

The left tail and right tail of PDF also correspond to two crucial parameters of STT-RAM: the RDR and the WER respectively. Fig. 4.9 (a) and (c) show the measured RDR and WER, based on Fig. 4.7. In both figures, the RDR and WER tails become much

shallower as V/V_{c0} increases to be larger than 1. It's against the fast read and write operation in ns regime for STT-RAM device as pointed out by R. Heindl *et al*[75]. Meanwhile, we noticed a weak "low probability bifurcated branch" in the WER curve of AP-P 5 ns in Fig. 4.9 (b) (red curve on right), similar to the case reported by Min *et al*[52]. The bifurcated branch was found in 3 of 5 measured identical samples when $V/V_{c0}>2$.

With the RDR tail down to 10^{-5}, we can also fit the thermal stability factor (Δ) from the RDR slope as proposed by Heindl *et al* [75]. The fitting of 10 ns, 100 ns and 1000 ns curves are shown in Fig. 4.9 (c). To check the fitting validation, we need to verify the premise $t_p/t<<1$, where t_p is the applied pulse width and $t=\tau_0 exp(\Delta(1-V/V_{c0}))$, τ_0=1 ns [75]. Taking the P-AP side for example, when t_p =1000 ns, Δ=30, V/V_{c0}=0.70, t_p/t = 0.1234, when t_p =100 ns, Δ=25, V/V_{c0}=0.75, t_p/t = 0.1930, and when t_p =10 ns, Δ=18, V/V_{c0}=0.80, t_p/t = 0.2732. All the three cases do not meet the criteria $t_p/t<<1$. Therefore, the smaller the t_p/t value, the more close the fitted thermal stability factor is compared to the statistic thermal stability factor value. It is important to do a careful check of fitting premise in order to get reasonable thermal stability factor by this method.

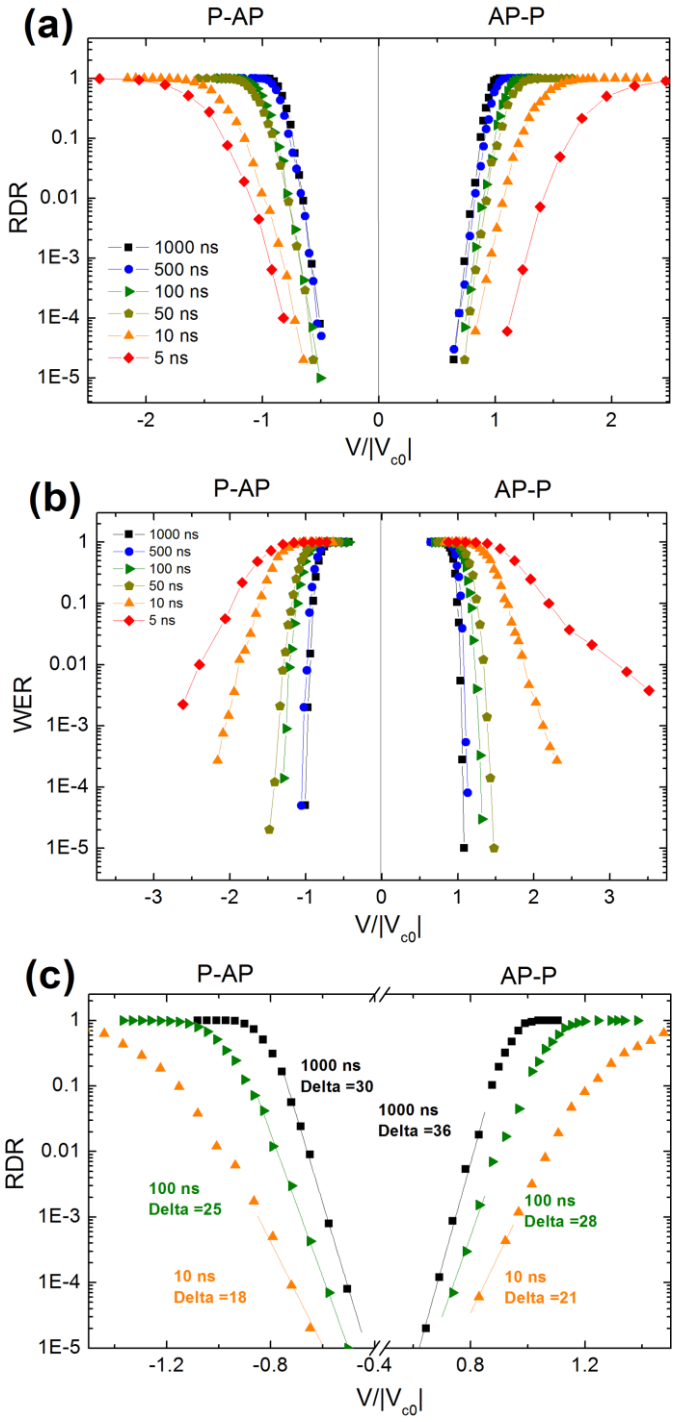

Fig. 4.9 (a) the Read Disturb Rate (RDR) as a function of $V/|V_{c0}|$; (b) Write Error Rate (WER) as a function of $V/|V_{c0}|$; (c) Evaluation of thermal stability factor from the RDR slope.

In summary, the STT switching voltage distribution in MgO MTJ is studied here by characterizing the switching PDF systematically with good statistics (10^5 trials) in a broad time range from 5 ns to 1 μs. It is found that the measured switching PDF can be fitted well by the skew normal distribution function down to 10^{-3}, so we can use this as a guideline to extrapolate the RDR and WER in STT-RAM design. Furthermore, the measured results also show that the switching PDF curve changes from right skew to left skew as the pulse width decreases. We propose that this phenomenon is due to the fluctuation mechanism transition from the thermal agitation to the initial magnetization trajectory dispersion. The fitted skewness value from the switching PDF is related with the contribution from the two fluctuation mechanisms. In the end, the RDR and WER tails under various pulse widths were also plotted and discussed. The work in this section was published in *IEEE Trans Magn.,* 48(11), 3818, (2012)[80].

4.2.4 Temperature dependent spin transfer torque induced switching

It is also crucial to understand the temperature-dependent performance of MTJ cells and STT switching for real STT-RAM applications, since the STT-RAM often has to work in a heated environment above room temperature, especially when it is used as an embedded memory. Until now, most of the previous reports were performed at room temperature (RT) or low temperature. Myer *et al.* studied the switching current dependence at low temperature from 180 K to 220K in nanomagnets with a pseudo spin valve stack structure[58]. Krivorotov *et al.* reported the temperature dependence of the dwell time for the resistance fluctuation with spin polarized current injection from 4.2K to 295 K in a similar structure[81]. To my best knowledge, no experimental work on MTJ

based STT switching performance has been reported at the potential working temperature for STT-RAM above RT.

In this section, the STT switching performance of MTJs above the room temperature (25 ºC-80 ºC) is studied. The particular temperature range is chosen to imitate the real working environment of STT-RAM. The TMR ratio, coercivity, thermal stability and switching current density are studied. In particular, I will show the mean and distribution values of STT switching current density for pulse widths ranging from 1 ns to 0.1 s at various temperatures. The effects of the environmental temperature on the distribution of the switching current density will be experimentally analyzed and correlated with different switching modes.

The samples studied here have a standard in-plane stack structure, MgO MTJ structure of (bottom electrode) / PtMn (15 nm) / $Co_{70}Fe_{30}$ (2.5 nm) / Ru (0.85 nm) / $Co_{40}Fe_{40}B_{20}$ (2.4 nm) / MgO (0.83 nm) / $Co_{20}Fe_{60}B_{20}$ (2.0 nm) / (top electrode). They were deposited using a Singulus TIMARIS sputtering system followed by a post annealing process at 300°C under 1 T magnetic field for 2 hours. The results shown in this section were measured in MTJs with two lateral dimensions, 50 nm×110 nm and 50 nm×170 nm. The switching CDF was collected on the first circuit and second circuit in Chapter 4.1 under zero effective bias field (free layer offset field canceled). 100 trials were used in the measurement for each probability data point.

The whole sample chip was heated by a film resistance heater (maximum power density $10W/in^2$) attached on the back side of the chip. Meanwhile, I also attached a reference chip on the same film resistance heater and monitored its temperature by a

thermocouple during the heating process. Since the reference chip was chosen to have the same size and material as the sample chip, the temperature of the two chips should be the identical. The heating process was controlled by the PID feedback mechanism with less than 1 °C temperature fluctuation. The temperature dependence of TMR ratio and coercivity was tested from 25 to 80 °C. The STT switching CDF from AP state to P state was characterized in a broad time range from 1 ns to 0.1 s and at three environmental temperatures: 25 °C, 50 °C and 75 °C.

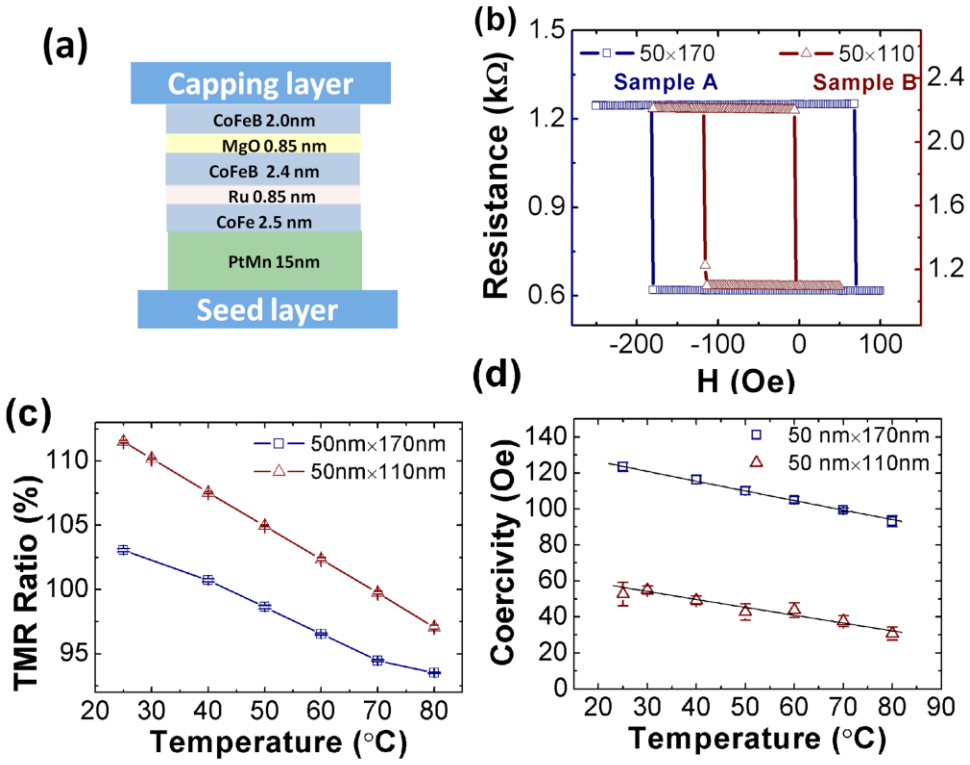

Fig. 4.10 (a) Schematic of an MTJ device stack structure. (b) Resistance versus magnetic field loop of Sample A (50 nm × 170 nm) and Sample B (50 nm × 110 nm). (c) and (d) TMR ratio and coercivity dependence on temperature of the two samples.

The resistance versus magnetic field loops of MTJ samples (Sample A: 50 nm×170 nm and Sample B: 50 nm×110 nm) at room temperature are given in Fig. 4.10 (b). With

the increase in aspect ratio from 2.2 to 3.4, the free layer coercivity doubles from 53 Oe to 123 Oe. A shift in the free layer R-H loop was found due to the coupling with the reference layer. Since the two samples were patterned from the same wafer, the shift (offset field) values are similar (~57 Oe for Sample A, and ~60 Oe for Sample B). An external field was applied during the STT switching probability measurement in order to cancel the offset field. The TMR ratio and coercivity dependence on temperature are shown in Fig. 4.10 (c) and (d), respectively. The mean and standard deviation are calculated from 10 measured R-H loops at each temperature point. The TMR ratio decreases by 10% (Sample A) and 14% (Sample B) from RT to 80 °C. The main reduction is in the AP state resistance, while the resistance of the P state remains almost constant. In Fig. 4.10 (d), we can see that for Sample A, the coercivity decreases from 123 Oe to 93 Oe (24.3%); and for Sample B, it decreases from 53 Oe to 31 Oe (41.5%). The smaller thermal stability of Sample B results in a higher relative coercivity reduction. Thermal stability factors are estimated to be 72 for Sample A and 29 for Sample B at RT according to the fitting in Fig. 4.10 (d) by Eq.(4.7) [82].

$$H_C = H_K \left[1 - \left(\frac{k_B T}{K_u V} \ln\left(\frac{\tau}{\tau_0} \right) \right)^{2/3} \right] \tag{4.7}$$

We further examine the temperature dependence of STT switching for those MTJ samples. Fig. 4.11 (a) and (b) show the switching current density value at 50% switching probability in the short time regime and long time regime, respectively. It is clear that in the ns time scale, the switching current densities at three temperatures overlap with each other, while in the long time regime (>1μs), there is an obvious switching current density

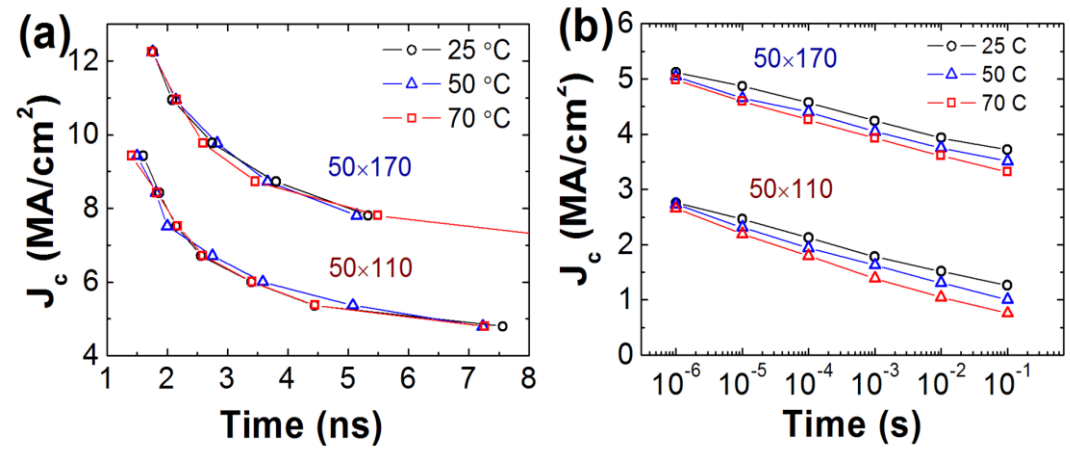

Fig. 4.11 (a) and (b) Switching current density at 50% switching probability versus pulse widths at short time scale (1–8 ns) and long time scale (1 μs–0.1 s).

reduction with the increase of the environmental temperature. The longer the switching time, the more the switching current decreases. Before further analysis, the Ohmic heating effect should be estimated. Since the anti-parallel state resistance has a strong dependence on temperature as discussed in Fig. 4.10 (c), it is used as a reference to determine the sample temperature during pulse onset period. We measured the anti-parallel resistance under 0.8 V continuously (corresponding to J=*8* MA/cm^2 and 10 MA/cm^2 for Sample B and Sample A) and found no detectable resistance reduction with the time for 1s (measurement error ±0.65 Ω). It means the temperature rises during this 1s period is negligible. In the switching probability measurement as shown in Fig. 4.11, the pulse widths are below 0.1 s and there is enough idle time (>0.5 s) between each pulse for heat dissipation. Therefore, the Ohmic heating is not the main reason for the strong dependence of STT switching current on the environmental temperature in the long pulse regime. These results could be explained by the two classic STT switching modes. In the long time regime, the free layer reversal happens by a thermally activated STT switching,

so the environmental temperature has more contribution during the switching process. On the other hand, in the short time regime, it is mainly a dynamic precessional switching process that is determined by the spin momentum transfer, relatively independent from the environmental temperature. We also estimate the thermal stability factor at three temperatures by the data presented in Fig. 4.11 (b) according Eq.(1.6).

The fitted thermal stability factors are 47 (at 25ºC), 46 (at 50ºC), and 41 (at 70ºC) for Sample A and 32 (at 25ºC), 30 (at 50ºC), and 28 (at 70ºC) for Sample B. We notice that the fitted thermal stability factor for Sample A here is much smaller compared to the previous value (72) fitted by Eq. (4.7). A similar discrepancy has been reported in several other works as summarized in Table 4.2.

It seems that the current ramping method usually gives an underestimated thermal stability factor compared to other methods which measure the thermal stability factor from magnetic characterization. The most possible reason for this discrepancy is that STT may induce non-uniform switching. Therefore, Eq.(1.6) derived from the macrospin model may not be valid. This can also explain the observation that a larger discrepancy was found in more thermally stable samples according to Table 4.2.

Table 4.2 Compare the thermal stability factors

Our Result			**Grandis**[50]			**MagIC-IBM**[52]		
$\Delta(I)^a$	$\Delta(H)^b$	$\Delta(H):\Delta(I)$	$\Delta(I)^a$	$\Delta(H)^b$	$\Delta(H):\Delta(I)$	$\Delta(I)^a$	$\Delta(H)^b$	$\Delta(H):\Delta(I)$
32	29	0.906	32	40	1.25	58.3	120	2.06
47	72	1.53	36	65	1.81	63.5	135	2.13

[a] Thermal stability factor measured by current ramping method Eq. (1.6).

[b] Thermal stability factor measured by magnetic characterization. Eq. (4.7).

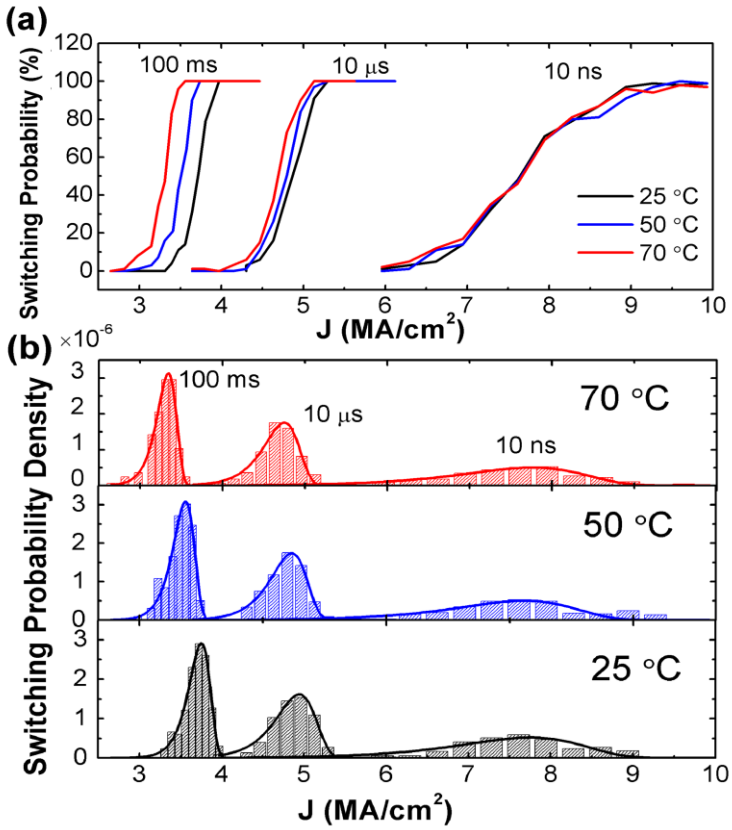

Fig. 4.12 (a) Switching probability as a function of current density measured in Sample A at 100 ms, 10 μs and 10 ns. (b) Switching probability density of sample A. The bars are experimental data and solid curves are fitted data.

The measured STT switching probability CDF curves of Sample A at 100 ms, 10 μs and 10 ns under three temperatures are shown in Fig. 4.12(a). The PDF curves calculated from the derivative of CDF curve are plotted in Fig. 4.12(b). It is notable that not only the median point of the switching current density decreases with increasing temperature as mentioned before, but also the whole switching PDF shifts together to the left when the sample is heated. This shift is more obvious for long pulses. The width of the switching PDF remains almost constant at all temperatures. The switching PDFs are fitted by Eq.(4.5). These fitted results are indicated by the solid curve in Fig. 4.12 (b). Although Eq.(4.5) was deduced from the thermal activation model, the shape of the switching PDF

still agrees very well with it in all time scales. However, in order to describe the increasing of the distribution width with the decreasing of the pulse width, the fitted thermal stability values have to be 46, 31, and 14 for 100 ms, 10 μs and 10 ns respectively. This may imply that modifications are possibly required for Eq.(4.5) when using it to carry out the design margin estimation for STT-RAM applications[57,83].

The mean and standard deviation (1σ) of Sample A from 10 ns to 0.1 s are summarized in Fig. 4.13(a). Similar to the result by Wang *et al*[84] and Driskill-Smith *et al*[50], the standard deviation increases dramatically with the reduction of pulse width especially below 1 μs. A simple explanation is that the variation from thermal fluctuation gets more chance to be averaged out in a longer time. A complete picture of switching current variation versus time was given by solving the stochastic LLG equation numerically[84]. In Fig. 4.13 (b) and (c), we also notice that the decreased energy barrier by the environmental temperature has more impact on the median point rather than the variation of switching current. This maybe because in the particular temperature range (25 ºC - 70 ºC) that we are interested, the decrease in the thermal stability is too small (from 47 to 41) to have a large influence on the switching current variation. As a result, the pulse width is the more important factor to be concerned with compared to the working temperature regarding the switching current variation in STT-RAM design.

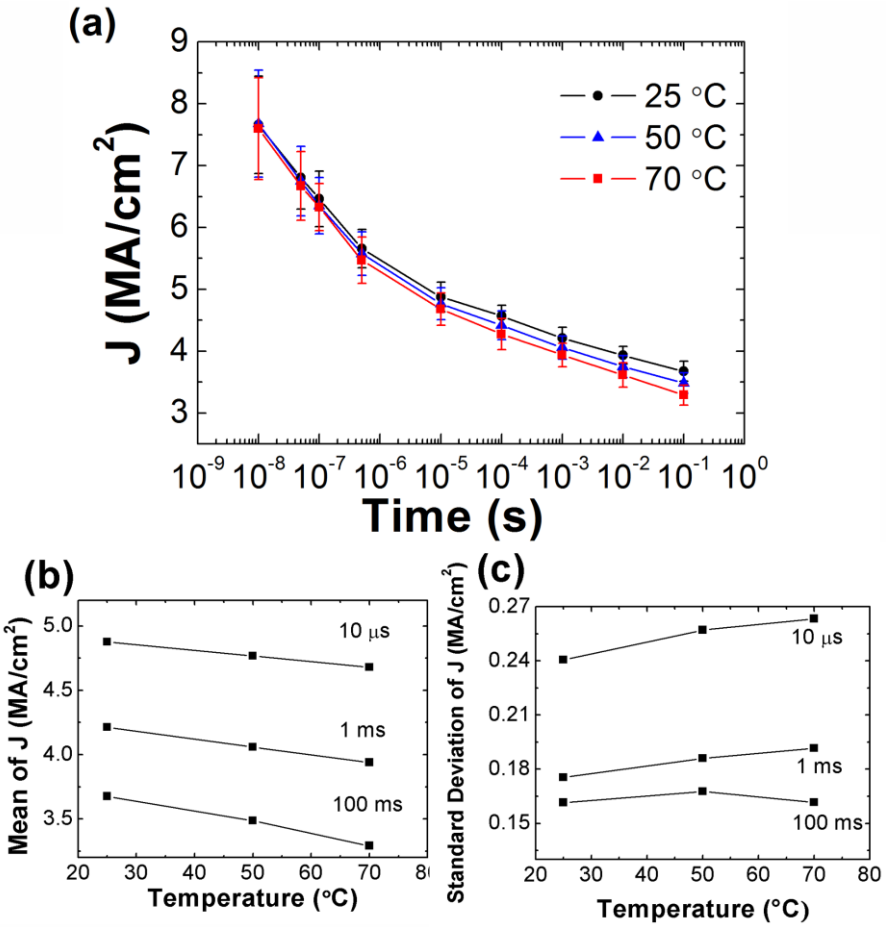

Fig. 4.13 (a) The current density from 10 ns to 0.1 s measured in Sample A. Each symbol represents the mean value and error shows the standard deviation. (b) and (c) Mean and Standard deviation of switching current density as a function of temperature measured in Sample A.

In conclusion, I investigated the MTJ memory cell performance in a temperature range close to the possible working environment for the STT-RAM application (25 ºC-80 ºC). The temperature dependences of TMR ratio, coercivity, thermal stability factor and STT switching current density distribution were studied. One important observation was that, due to the distinct STT switching modes, the influence of the environmental temperature on the switching current greatly depended on the switching time. As the temperature increases, the switching current density reduction with temperature was only

found in the long pulse range (>1μs), not in the short pulse range (<10 ns). Furthermore, in the particular temperature range we are interested, the switching current density variation was found to be less sensitive to the environmental temperature compared to the switching time, which means the latter is the more important factor to consider in STT-RAM design. This work was published in *IEEE Magn. Lett., 3,* 3000304, (2012)[85].

4.3 Summary

In this chapter, I discussed my general study on the STT induced switching, including the three STT induced switching modes, the switching energy, the switching speed and the switching distribution based on my measurement results. In the end, the temperature dependent STT induced switching behavior was also characterized.

First, the three STT induced switching modes were demonstrated experimentally and they agreed with the STT macrospin model. Key parameters such as the intrinsic critical current density and thermal stability factor were obtained by fitting the experimental data with the macrospin model equations. I also explained the switching mechanism and switching distribution mechanism of the three switching modes.

Second, I characterized the writing energy and writing speed in an in-plane MTJ and provided a group of complete parameters related to the STT induced switching process for the STT-RAM design. The device here has the parameters of RA=4.3 Ω μm^2, TMR = 135% and thermal stability factor $\Delta(I)$=50 (by current ramping measurement). The optimal writing energy is 0.286 pJ per bit at 1.54 ns for AP to P state switching, and 0.706 pJ per bit at 0.68 ns for P state to AP state switching. The minimum switching speeds in this sample are 580 ps (AP to P) and 560 ps (P to AP). As a result, 0.6–1.3 GHz

was determined to be the optimal writing rate from writing energy consumption of view. These results show that in-plane MgO MTJs are still a viable candidate as the fast memory cell for STT-RAM. The work in first and second section were published in *J. Appl. Phys.,* 109, 07C720, (2011)[72].

Third, the STT induced switching voltage distribution was studied by characterizing the switching PDF with large statistics (10^5 trials) across a wide time scale from 5 ns to 1 μs. The skew normal distribution function is found to be a good one to fit the measured switching PDF down to low values, which would be used as a guideline to extrapolate the RDR and WER in STT-RAM design. Moreover, the asymmetry of switching probability density function is observed to flip when the pulse width decreases. It is related to the fluctuation mechanism transition from the thermal agitation to the initial magnetization trajectory dispersion. The work in this section was published in *IEEE Trans Magn.,* 48(11), 3818, (2012)[80].

Last but not the least, I studied the temperature dependences of the TMR ratio, coercivity, thermal stability factor and switching current distribution in the temperature range of 25–80 ◦C, the most probable working environment for STT-RAM application. Two distinct temperature dependence of the switching current density are apparent due to the two switching modes: a switching current density decrease with increasing temperature in the long-pulse (>1 μs) regime, a result of thermally activated switching, but no decrease in the short-pulse (<10 ns) regime, as a result of precessional switching. In the temperature range studied, the switching current density variation is less sensitive to environmental temperature than it is to switching time. Thus, switching time is the

more important factor to consider in STT-RAM design. This work was published in *IEEE Magn. Lett., 3,* 3000304, (2012)[85].

5 Ultrafast sub 200 ps spin transfer torque induced switching demonstration

One of the crucial limitations for ultrafast STT induced switching is the incubation delay induced by pre-switching oscillation[86]. Several approaches have been proposed to minimize pre-switching oscillations in order to improve the switching speed in spin valves, such as developing all perpendicular structures[71], applying hard axis field to set the free layer equilibrium away from easy axis[87], and adding an extra perpendicular polarizer[88–90]. As of now, limited work has been done on sub-nanosecond STT switching in MTJs. Minimum switching times of 400 ps – 580 ps at 50% switching probability has been reported in conventional in-plane MTJs[72,91]. By adding a perpendicular polarizer, H. Liu *et al* showed 100% switching at 500 ps with external field assistance in their MTJ+spin value device[92]. G. Rowlands *et al* achieved 50% switching probability at 120 ps under zero bias field in the full orthogonal MTJ[93].

In this chapter, I will demonstrate the ultrafast STT induced switching (165 ps – 10 ns) under zero bias field in CoFeB-MgO MTJs with good TMR ratio around 100% and large coercivity (100 Oe). With a basic conventional stack structure, the sample exhibits ultrafast switching in the sub-200ps regime while maintaining all the requirements for STT-RAM application.

5.1 Sample Information and Measurement setup

The MTJs' stacking structure is as follows: (bottom electrode) / PtMn (15 nm) / $Co_{70}Fe_{30}$ (2.3 nm) / Ru (0.85 nm) / $Co_{40}Fe_{40}B_{20}$ (2.4 nm) / MgO (0.83 nm) / $Co_{20}Fe_{60}B_{20}$ (1.7-2.0 nm) / (top electrode). Here an Fe-rich free layer is used, which has a strong interface perpendicular anisotropy as discussed in Chapter 3.2.2. The thickness of the free layer is 1.7 nm - 2.0 nm, and therefore still retains its easy axis in plane[69,70]. The sample was post-annealed at 300°C under 1 T magnetic field for two hours. MTJ devices in this paper were patterned into 50 nm × 150nm elliptical nanopillars.

The switching probability measurement was performed on Circuit 2 as shown in Chapter 4.1 at room temperature. Each probability value was calculated by 200 switching trials with the free layer magnetization preset by a 1 μs reset pulse. A small magnetic field is applied to center the free layer R-H loop during the switching probability measurement. The 100 ps to 10 ns switching pulse was generated by the Picosecond bipolar voltage pulse generator 10070A, which has a rise and fall time of 65 and 85 ps, respectively.

5.2 Result and discussion

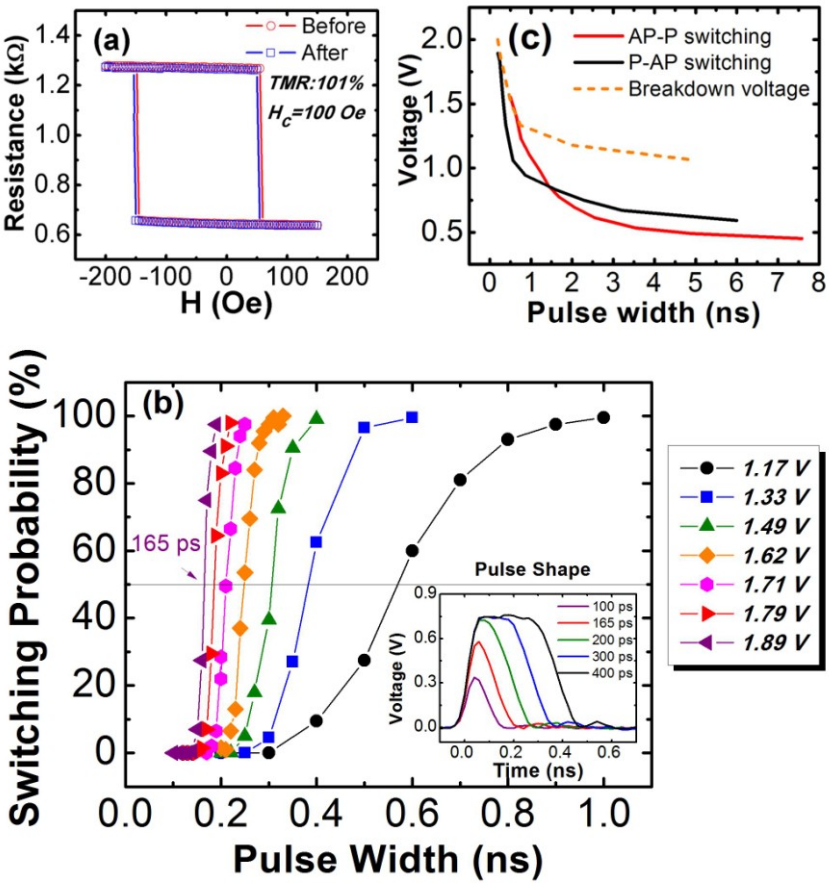

Fig. 5.1 (a) MTJ resistance versus magnetic field loop at room temperature. Red curve is tested before switching probability measurement and blue curve is obtained after switching probability measurement. (b) Switching probability dependence on pulse width with various pulse amplitudes on P-AP side. Each curve corresponds to the same setting voltage on pulse generator. The inset figure shows the change of pulse shape from 100 ps to 400 ps with the same setting amplitude. Because of the pulse peak attenuation, the labeled voltage in (b) is the peak voltage at the pulse duration corresponding to 50% switching probability. For example, the first curve (purple, triangle-to-left) has the nominal pulse amplitude at 2.4 V for long pulses. The labled value is 1.89 V, which means the peak value at 165 ps pulse width with 50% switching probability. All of the pulse voltage values used in this paper are the peak voltage measured by Tektronix DPO72004BO scilloscope (20 GHz bandwidth and 50 GHz sampling rate) multiplied by the reflection coefficient at the MTJ end ($\Gamma=2R_{MTJ}/(R_{MTJ}+Z_0)$) (c) Pulse voltage as a function of pulse width at 50% switching probability for AP-P and P-AP switching. And the dash line is the breakdown voltage at different pulse widths.

Fig. 5.1 (a) shows the R-H loop of a MTJ sample with 2.0 nm free layer. The sample has a TMR ratio of 101% and a coercivity of 100 Oe. By averaging from a group of similar devices, the thermal stability is estimated to be above 65 k_BT according to the hard-axis magnetoresistance curve fitting method[94]. The loop is centered at -45 Oe due to the coupling with pinned layer, which is compensated by an external field during all the following switching probability measurements. The nearly overlapping blue and red R-H loops were obtained before and after the switching probability measurement, respectively, and showed that no partial breakdown of the barrier or change of magnetic properties had occurred.

The switching probability as a function of pulse width is plotted in Fig. 5.1 (b), where each curve represents the setting same pulse amplitude. The labeled voltage is the pulse peak voltage on the device at the pulse duration corresponding to 50% switching probability. Please find more description in the figure caption of Fig. 5.1 (b). The sample is found to have 50% switching probability at 165 ps and 98 % switching probability at 190 ps. Moreover, the switching probability curves were very steep and did not display a switching probability plateau because of the half precession period jitter as observed in some metallic spin valves[86]. The observed sub 200 ps switching implies that incubation delay did not occur as a result of pre-switching oscillation. To calculate the writing energy, I did an integration based on the pulse shape for each pulse width by $E_w = \int V^2(t)/R\, dt$. The minimum writing energy of P-AP switching for 50% and 98% switching probabilities are 0.16 pJ and 0.21 pJ, respectively. During the measurement, the samples can generally survive 10^3 – 10^4 writing cycles for the sub 200 ps switching. I

also calculated the endurance in our sample according to Ref. 52, with 1.107 V, 500 ps pulse width. The failure rate is 3.25×10^{-4}.

The same switching probability measurement was also done for AP-P switching. I plot the pulse amplitude versus pulse width at 50% probability in Fig. 5.1 (c) together with the breakdown voltage, which was measured from 20 MTJs' breakdown point with identical barrier thickness at various pulse widths. The figure shows that the achievable minimum switching time is limited by the breakdown voltage of the device. With the same applied voltage, the current through the device in the P state is about twice of the value in the AP state due to the resistance difference in each state. Therefore, for P-AP switching higher voltages can be reached, thus allowing shorter switching times, as shown Fig. 5.1 (c).

Two other MTJs of the same size but with thinner free layers (1.90 nm, 1.73 nm) were also measured for ultrafast switching probabilities in the sub-ns regime. The results were summarized in Fig. 5.2. The red line indicates the current density at which the oxide barrier breaks down at different pulse widths. Again, the minimum measured switching time is limited by the breakdown voltage, especially in the AP-P switching case due to its higher resistance. For the 1.73 nm free layer sample, I found 50% switching probability at 195 ps for AP-P switching, and 190 ps for P-AP switching, corresponding to 0.12 pJ and 0.23 pJ writing energy respectively.

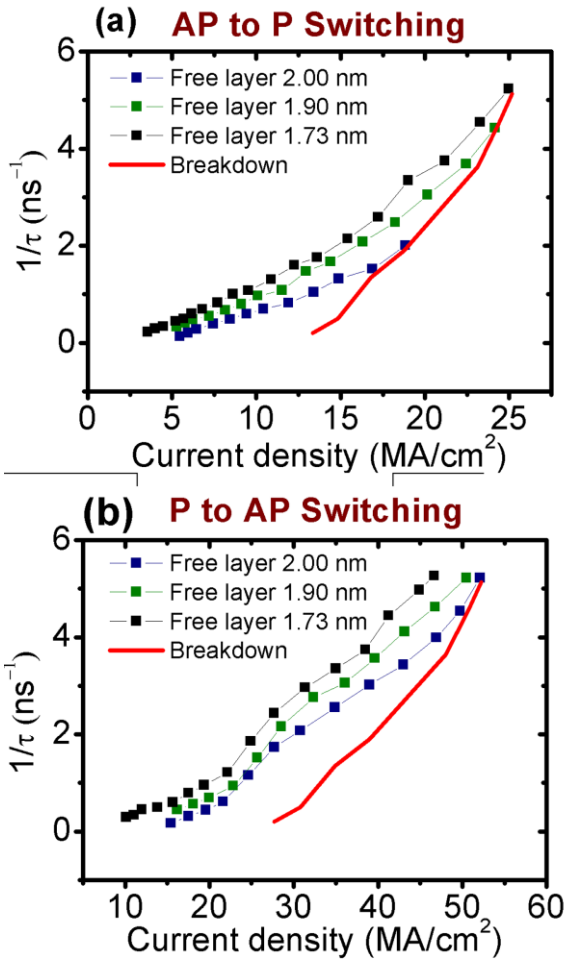

Fig. 5.2 the inverse of pulse width as a function of current density for AP-P switching (a) and P-AP switching (b). Red curve indicates equivalent breakdown current density at various pulse widths.

According to the Macrospin approximation of STT switching theory, the precessional switching time is inversely proportional to the applied current density (Eq.(4.2)).

The linear relationships in Fig. 5.2 (a) and (b), between τ^{-1} and J at $\tau^{-1}>1\ ns^{-1}$ show that with such a short pulse duration, the switching process is mainly precessional switching. In the regime *of* $\tau^{-1}<1\ ns^{-1}$, thermal activation starts to contribute to STT switching, leading the tails near zero to gradually become more shallow as less current

density is needed for switching. Furthermore, as the free layer thickness decreases from 2.00 nm to 1.73nm, the curves shift from right to the left indicating a reduction of J_{c0}.

It is noteworthy to point out that in our basic in-plane MgO MTJ structure, the demonstrated switching speed of 165 ps (50%) and 190 ps (98%) is surprisingly similar to the value in orthogonal MTJs[92,93]. I propose here that the observed ultrafast STT switching mainly benefits from interface perpendicular anisotropy between the MgO layer and $Co_{20}Fe_{60}B_{20}$ layer. As a result of that, the out-of-plane demagnetizing field in the free layer is partially canceled. In our sample, interface perpendicular anisotropy K_i is calibrated by VSM measurement as 1.33 erg/cm (Chapter 3.2.2). We define H_d as the out-of-plane demagnetizing field, and $H_\perp$ as the free layer perpendicular interface anisotropy field corresponding to $2K_i/M_st$. Therefore, assuming H_d is $4\pi M_s$ in all areas, H_d - $H_\perp$ is 5106 Oe, 4317 Oe and 2765 Oe for 2.00 nm, 1.90 nm and 1.73 nm free layers respectively. It means the effective out-of-plane demagnetizing field is mostly canceled. This can affect the STT switching in two aspects: the reduction of J_{c0} and the canted local magnetization on edges.

First of all, it has been shown in Chapter 3.2.2 that the interface perpendicular anisotropy in in-plane MTJ devices can effectively reduce the critical current density Eq.(3.3)). It is because the dominant easy plane shape anisotropy term $2\pi M_s$ in Eq.(3.3) can be partially canceled by $H_\perp/2$. In my measurement, the averaged J_{c0} in the $Co_{20}Fe_{60}B_{20}$ free layer sample (*High* K_i) is 48% lower than the value in $Co_{60}Fe_{20}B_{20}$free layer sample (*Low* K_i) (Chapter 3.2.2). Therefore, with the same maximum input voltage (defined by the barrier breakdown voltage), lower J_{c0} means higher J/J_{c0} ratio.

Second, in the localized areas of devices such as the two edges of free layer along long axis, the demagnetizing effect that keeps the magnetization in-plane is weaker. Therefore, when there is a large interface perpendicular anisotropy component present, the local magnetization on the two ends of long axis may start to cant out of plane very easily. I have calculated the local magnetization direction of the 2.0 nm and 1.7 nm free layers by OOMMF[95]. The canted local magnetizations on two ends of the free layer are shown in Fig. 5.3. It is possible that these areas could act as the magnetization nucleation starting points of STT switching because of the larger initial angle θ_0 between the free layer and the pinned layer. Ultrafast switching of the entire free layer may be induced by the quick onset of switching at these hotspots.

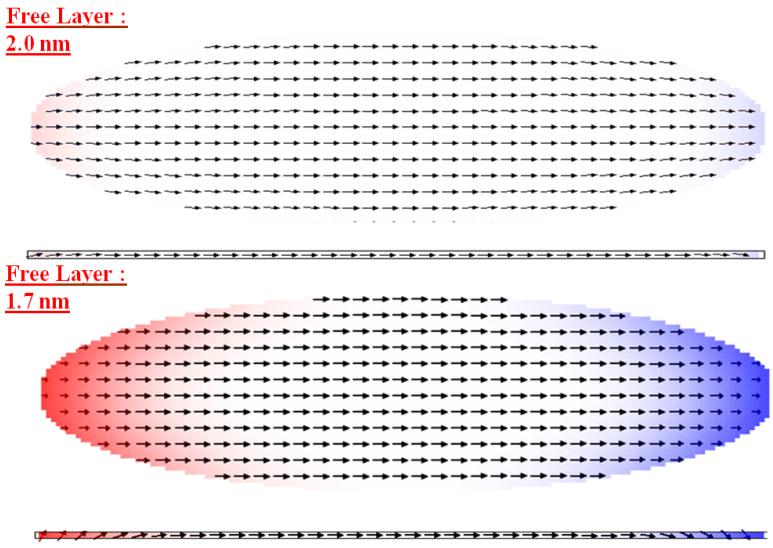

Fig. 5.3 Local magnetization direction of a single free layer under demag-field by micromagnetic simulation (OOMMF). The color represents magnetization components in out-of-plane direction.

5.3 Summary

In conclusion, I demonstrated the ultrafast STT switching of 165 ps and 190 ps with 50% and 98% switching probabilities, respectively, in conventional MgO MTJ structures without field assistance. No plateau of switching probability versus pulse width appeared in our data as found in some metallic spin valves for sub-ns STT switching. My device also showed a 101% TMR ratio and room temperature thermal stability factor of more than 65 k_BT, which make it a good candidate for STT-RAM application. The effect of free layer thickness on ultrafast switching performance was discussed and we found 190-195 ps switching in both AP-P and P-AP testing from the same sample. The observed ultrafast switching is believed to occur because of partially canceled out-of-plane demagnetizing field in the free layer from interface perpendicular anisotropy between the MgO layer and $Co_{20}Fe_{60}B_{20}$ layer. High J/J_{c0} ratio and magnetization nucleation at the edge of free layer, which both result from the reduced perpendicular demagnetizing field, are possibly two major factors that contribute to the ultrafast spin transfer torque switching. This work was published in *J. Phys. D.* 45(2), 025001, (2012)[96].

6 Dynamic energy barrier reduction under high frequency fluctuation

Fluctuation induced escape over a potential barrier is a common problem in nature. According to Kramers' classical theory, the escape rate of a thermally equilibrium system is proportional to $f_0 e^{-\delta\varepsilon/k_B T}$ where f_0 is the attempt frequency depending on the particular system, $\delta\varepsilon$ is the energy barrier, k_B is the Boltzmann constant and T is the temperature[97]. However, for a non-equilibrium system under both random thermal fluctuation and external periodic excitation, this scheme cannot apply and the escape rate must be calculated from the system dynamics with the complicated interplay between periodic excitation and thermal noise[98,99]. It has been shown that with the periodic excitation, the escape rate can be effectively increased[100,101]. The most well-known example is called resonance activation[102–104], which refers to the significant escape rate increase in the presence of periodic excitations at the system's resonant frequency. This was demonstrated experimentally by Cui *et al.*[105] and Chen *et al.*[106] in the magnetic systems.

However, besides the resonant activation effect, the escape rate enhancement caused by non-resonant frequency excitations has usually been neglected in magnetic systems[107–109]. This effect leads to quite different conclusions beyond the conventional understanding based on Kramer's classical theory, which means the long time magnetization nonvolatility, *i.e.* reversal probability is only described by the ratio of magnetization stability energy barrier over thermal energy. In this chapter, I will show that the conventional approach based upon the energy barrier over thermal Boltzmann

factor is insufficient to characterize the long time magnetization nonvolatility under high frequency excitations. An extra dynamic energy barrier reduction is observed due to the high frequency excitations. A concept based upon the large angle nonlinear magnetization dynamics, such as magnetization logarithmic susceptibility[110] (defined as the ratio of dynamic energy barrier reduction to the external excitation magnitude), is required to describe the magnetization nonvolatility under high frequency excitations. These reported experimental results and theoretical analysis are not only critical for understanding the magnetization dynamics under combined external forces and thermal fluctuations, but also helpful in designing and engineering emerging spintronic devices for practical applications.

In this chapter, I will first present the conventional and the proposed theory that will be used to explain our experiment results. Then I will show detailed experiment measurements of long time thermal magnetization switching and magnetization logarithmic susceptibility up to 2 GHz. Our measurements demonstrate the inconsistency of conventional energy barrier approach for describing high frequency excitation on thermally activated magnetization switching. Magnetic properties of MTJs are also characterized through the magnetization logarithmic susceptibility measurements by fitting the experimental data with modeling results.

6.1 Theoretical background

A. The Time Dependent Energy Barrier [110, 111]

As described before, according to the conventional energy barrier approach, the magnetization switching probability is given by a transition rate (γ) as follows:

$$\gamma = f_0 e^{-\delta\varepsilon / k_B T} \quad (6.1)$$

Both $\delta\varepsilon / k_B T$ and f_0 depend on temperature T and external forcing magnitude h as $\delta\varepsilon = \delta\varepsilon(h), f_0 = f_0(h,T)$. The probability of magnetization decay is determined by the master equation as

$$\frac{dp}{dt} = -\gamma(h,T)p \quad (6.2)$$

where p is the probability of the magnetization still remaining in the initial state. For magnetization evolving between two metastable states ($m = \pm 1$) with the initial state m=1, the averaged magnetization is $m = (+1)\cdot p + (-1)\cdot(1-p) = 2p - 1$. The magnetization decay as a function of time can then be derived by the integration of Eq.(6.2)

$$-\int_{t_i}^{t_f} \gamma(h,T)dt = \ln\frac{p_f}{p_i} = \ln\frac{m_f + 1}{m_i + 1} \quad (6.3)$$

where "i" means the initial state and "f" means the final state.

Now apply Eq.(6.3) to two special cases, where the two periodic excitations have the same scaled shapes but k times difference in period. For example, in the simplest case of two sinusoid excitations, the two excitations are $h_1(t)=A*\sin(2\pi t/T_1)$ and $h_2(t)=A*\sin(2\pi t/T_2)$ and $T_2=kT_1$. Therefore, $h_2(t) = h_1(t/k)$ leads to $\gamma_2(t) = \gamma_1(t/k)$. For the magnetization decay under the above two self-similar periodic excitations, Eq.(6.3) can be integrated over N period of T_2 as

$$\ln\frac{m_{2f}(NT_2)+1}{m_{2i}(NT_2)+1}=-\int_0^{NT_2}\gamma_2(t)dt$$
$$=-\int_0^{NT_2}\gamma_1(t/k)dt=-k\int_0^{NT_2/k}\gamma_1(t')dt'=-k\int_0^{NT_1}\gamma_1(t')dt' \quad (6.4)$$
$$=-\int_0^{NkT_1}\gamma_1(t')dt' \quad =-\int_0^{NT_2}\gamma_1(t')dt'=\ln\frac{m_{1f}(NT_2)+1}{m_{1i}(NT_2)+1}$$

If Eq.(6.4) is true, it means the magnetization decay of two self-similar excitations is identical after a time duration of NT_2. This equivalence holds true independent of the detailed pulse shape, periodicity, magnetic properties and temperature.

However, our experimental results in this chapter demonstrated that the thermal magnetization decay strongly depends upon the excitation frequency. Eq.(6.4) could not hold true for the magnetization decay over a wide range of excitation frequencies. This inconsistency roots in the conventional energy barrier approach neglecting the detailed magnetization dynamics. This inconsistency is also described as “a scale dilemma” in Ref. 111.

Therefore, the concept of magnetization logarithmic susceptibility is proposed. It is defined as the energy barrier reduction from the static energy barrier divided by the external excitation magnitude. More detail about the magnetization logarithmic susceptibility concept can be found in the next section. It should be pointed out here that the term “energy barrier” in Eq.(6.1) and Eq.(6.2) is the true static energy barrier based on the energy surface analysis. In the concept of magnetization logarithmic susceptibility, the “energy barrier reduction” term is not the static energy barrier from energy surface analysis. Instead, it is the equivalent static energy barrier reduction when considering the contribution of external excitations through fast magnetization dynamics.

B. Magnetization Logarithmic Susceptibility Theory [110, 111]

The free layer of MTJ is considered as a macrospin with the normalized energy density of

$$\varepsilon = \frac{E_M}{M_s^2 V} = \frac{1}{2}\left(D_x m_x^2 + D_y m_y^2 + D_z m_z^2\right), \qquad \text{with } D_z < D_x \text{ and } D_y \tag{6.5}$$

where M_s is the saturation magnetization, V is the volume, and D_x, D_y and D_z are modified demagnetization factors including all anisotropy components.

At finite temperature, the stochastic LLG equation is used to describe the magnetization dynamics. In the long time thermal activated switching mode, when the thermal fluctuation $\delta = k_B T/\Delta\varepsilon_0 \ll 1$ and the applied spin current excitation is well below the critical current, the magnetization switching trajectory is mainly determined by the system's intrinsic optimal reversal path. The optimal path can be obtained by the minimization of the proper action functional in the stochastic LLG equation. When the spin current excitation is applied, the change of the reversal energy barrier $(\Delta\varepsilon_0+\delta\varepsilon)$ as a result of the spin torque effect is calculated to be [110]

$$\begin{aligned} \delta\varepsilon &= \min_{t_c} \int_{-\infty}^{\infty} \left[\chi(t)\beta(t-t_c)\right]dt \\ \chi(t) &= \left[1-z_0^2(t)\right]\left\{-z_0(t)\left[D_x \cos^2\varphi_0(t) + D_y \sin^2\varphi_0(t)\right] + D_z z_0(t)\right\}, \end{aligned} \tag{6.6}$$

where β is the normalized spin torque polarization magnitude proportional to current. t_c is the "best" time for the magnetization reversal to happen. $\chi(t)$ is time domain magnetization logarithmic susceptibility (TD-MLS), which is defined as $(d\delta\varepsilon/dt)/\beta(t)$, meaning the ratio of work done by the spin torque per unit time to the normalized spin torque polarization magnitude. $\varphi_0(t)$ and $z_0(t)$ are coordinates of the magnetization

optimal reversal path in cylindrical coordinate system: $\overrightarrow{m(t)} = \left(\sqrt{1-z_o(t)^2}\cos\varphi_0(t), \sqrt{1-z_o(t)^2}\sin\varphi_0(t), z_o\right)$. Please note $\delta\varepsilon$ is a negative value in this case.

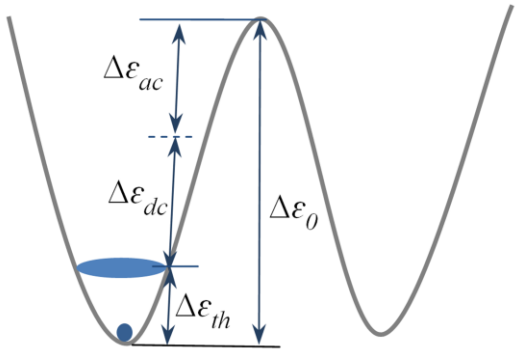

Fig. 6.1 The schematic picture of the static energy barrier, the thermal fluctuation and the dynamic energy barrier reduction.

Fig. 6.1 is a schematic picture of the system. The static energy barrier between two metastable states is $\Delta\varepsilon_0$. At finite temperature the particle will be lifted by an average of $\Delta\varepsilon_{th}=k_BT$ from the thermal fluctuation. $\delta\varepsilon$ is the maximum energy it gained from the periodic excitation as discussed above, in other words, the dynamic reversal barrier reduction. As a result, the final energy barrier seen by the particle is $\Delta\varepsilon_0$ - $\delta\varepsilon$ - k_BT.

On the other hand, the energy barrier reduction can also be calculated in frequency domain as listed in Eq.(6.7), where $\hat{\chi}(\omega)$ and $\hat{\beta}(\omega)$ are the Fourier transform of TD-MLS and the normalized spin torque polarization, respectively. When only the single frequency harmonic AC current is applied, the physical meaning of $\left|\hat{\chi}(\omega)\right|$ can be understood as the ratio of the energy barrier reduction to the magnitude of the normalized

AC spin torque polarization as shown in Eq.(6.7). In the rest of the paper, the frequency domain magnetization logarithmic susceptibility (FD-MLS) refers to $\left|\hat{\chi}(\omega)\right|$.

$$\begin{aligned} &|\delta\varepsilon| = \max_{t_c} \int_{-\infty}^{\infty} \left|\hat{\chi}(\omega)\hat{\beta}(\omega)e^{i\omega t_c}\right| d\omega \\ &if\ \beta(t) = \beta_0 \cos\omega_0 t,\ |\delta\varepsilon| = \beta_0 \left|\hat{\chi}(\omega_0)\right|,\ \left|\hat{\chi}(\omega_0)\right| = |\delta\varepsilon|/\beta_0 \end{aligned} \tag{6.7}$$

In a system with rotational symmetry along z direction ($D_z < D_x = D_y$), $\chi(t)$ has an analytical solution as shown in Eq. (6.8), where α is the damping constant. For systems without rotational symmetry such as an elliptical thin film layer in MTJ, the principle is the same, but the optimal reversal path has to be calculated numerically, as do the TD-MLS and FD-MLS. The decay of the FD-MLS data means that the reversal barrier reduction effect decreases with the driving frequency. This roll-off tail can be used to obtaining the damping constant and the magnetic symmetry (D_x, D_y, D_z). It's also interesting to note that the optimal path is an intrinsic property of the magnetic system, which is only determined by magnetic system parameters D_x, D_y and D_z and α as shown in Eq. (6.8). Therefore, $\chi(t)$ and $\hat{\chi}(\omega)$ are also independent from any external excitation sources. This could lead to a reliable measurement method of *Dx, Dy, Dz* and *α*.

$$\chi(t) = (D_x - D_z)\cos\left[\tan^{-1}\left(e^{\alpha(D_x - D_z)t}\right)\right]\left\{1 - \cos^2\left[\tan^{-1}\left(e^{\alpha(D_x - D_z)t}\right)\right]\right\} \tag{6.8}$$

Fig. 6.2 (a) and (c) show two examples of the optimal reversal path for a rotational symmetric case with its easy axis along the z direction (D_z = 0.48, $D_x = D_y$= 6.04, *Ms*=1000 emu/cc, damping=0.0055), and a non-rotational symmetric case also with its easy axis along the z direction (D_z=0.2116, D_x=0.4330, D_y=11.92, *Ms*=1000 emu/cc, damping=0.0055), respectively. The rotational symmetric case can be understood as a

circular thin film with the easy axis out-of-plane. The non-rotational symmetric case can be understood as an elliptical thin film with the easy axis along the long axis in-plane.

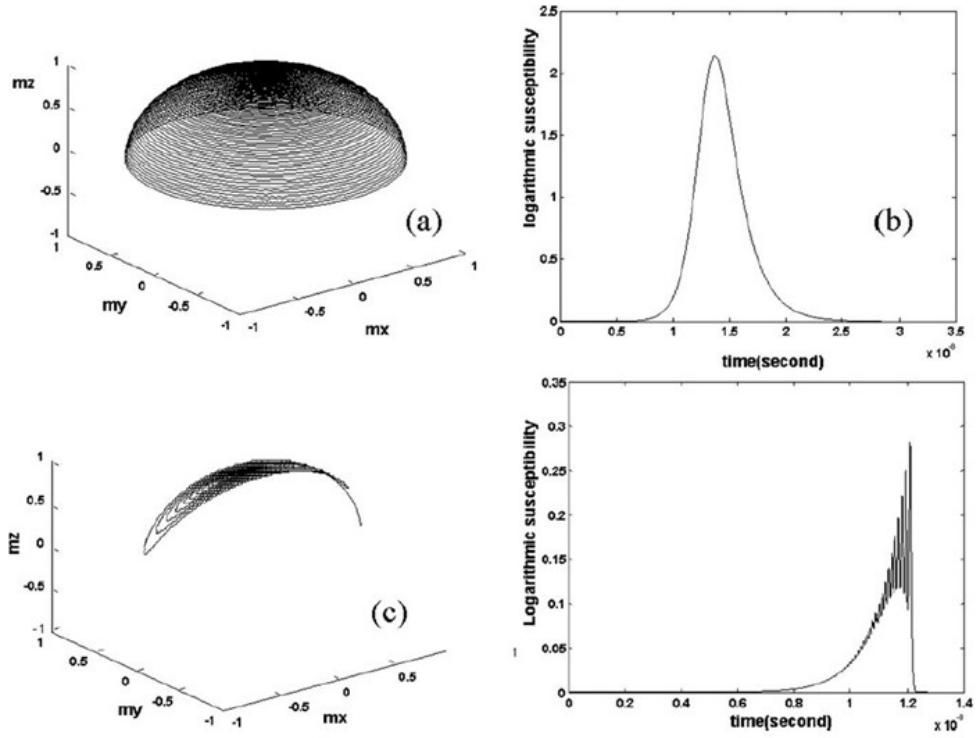

Fig. 6.2 (a) the optimal reversal path and (b) its TD-MLS of a magnetic element with rotational symmetry (D_z =0.48, $D_x = D_y$=6.04, Ms=1000 emu/cc, damping=0.0055). (c), the optimal reversal path and (d) its TD-MLS of a magnetic element with non-rotational symmetry (D_z=0.2116, D_x=0.4330, D_y=11.92, Ms=1000 emu/cc, damping=0.0055). Figure is from Ref. 111.

The time-domain magnetization logarithmic susceptibility (TD-MLS) is calculated by substituting the optimal reversal path in Eq. (6.8). The corresponding TD-MLS ($\chi(t)$) of the rotational symmetric case and the non-rotational symmetric case are plotted in Fig. 6.2 (b) and (d), respectively. Unlike the optimal path in the rotational symmetric case, the optimal path in the non-rotational symmetric case is highly confined in the x-z plane with an elliptical-like shape because $D_y \gg D_x$. As a result, its TD-MLS shows fluctuations around its ferromagnetic resonance frequency (4.51 GHz). The frequency-domain

magnetization logarithmic susceptibility (FD-MLS) ($\chi(\omega)$) is the Fourier transform of the TD-MLS ($\chi(t)$). The FD-MLS ($\chi(\omega)$) of both cases are shown in Fig. 6.3. Since we are only interested in the low frequency roll-off tail (< 2 GHz) of the FD-MLS ($\chi(\omega)$), those high frequency fluctuations in the TD-MLS ($\chi(t)$) of the non-rotational symmetric case do not show up in Fig. 6.3 (b).

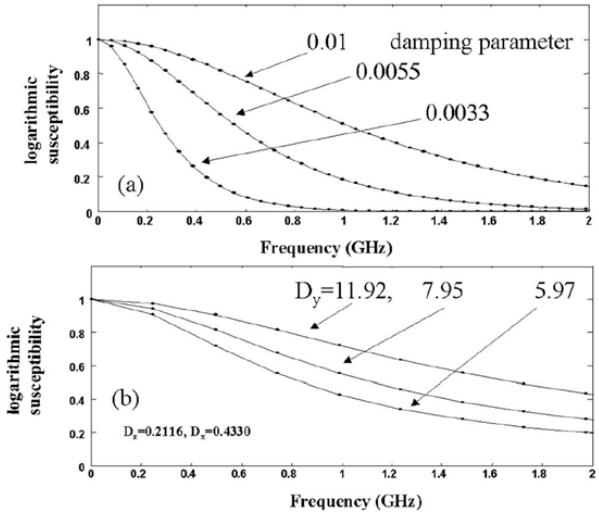

Fig. 6.3 the FD-MLS of magnetic elements with rotational symmetry (a) and rotational symmetry (b). In (a), D_z =0.48, $D_x = D_y$=6.04, Ms=1000 emu/cc. In (b), damping =0.0055. Figure is from Ref. 111.

6.2 Sample Information and Measurement setup

The MTJ sample I measured has a structure of (bottom electrode) / PtMn (15 nm) / $Co_{70}Fe_{30}$ (2.5 nm) / Ru (0.85 nm) / $Co_{40}Fe_{40}B_{20}$ (2.4 nm) / MgO (0.83 nm) / $Co_{20}Fe_{60}B_{20}$ (1.75-2.0 nm) / (top electrode). The free layer has a strong interface perpendicular anisotropy (K_i=1.33 erg/cm^2) which turns its easy axis from in-plane to out-of-plane at t=1.475 nm. The samples we measured still have the free layer easy axis in-plane since the thickness (1.75-2.0 nm) is above the transition point (Chapter 3.2.2).

(a)

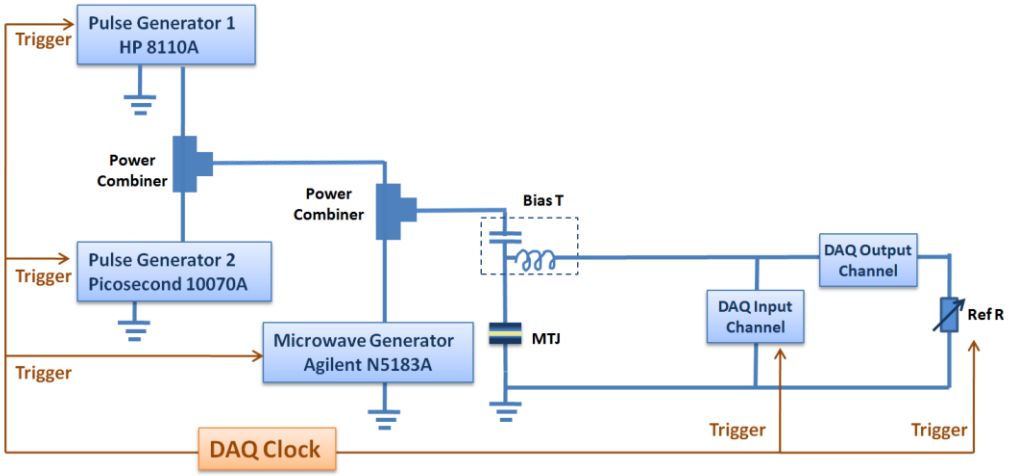

(b)

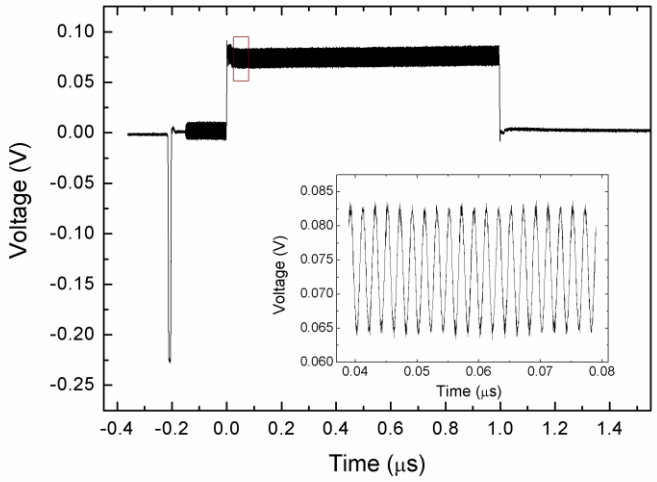

Fig. 6.4 (a) measurement circuit of Section IV and V. (b) the real input pulse waveform measured by Tektronix DPO72004B storage oscilloscope with 50GHz sampling rate. The inset figure shows the enlarged waveform between 0.04 μs and 0.08 μs.

The measurement circuit is shown in Fig. 6.4(a). It is similar to Circuit 3 in Chapter 4.1. The reset pulse is generated by Picosecond 10070A with 10 ns pulse width. The

switching pulse is output by H-P 8110A. The microwave is generated by Agilent N5183A. The outputs of the three generators are connected through two RF power combiners. The combined input pulse waveforms are then applied to the MTJ through the AC port of bias tee. The MTJ resistance state is tested by a DAQ card (NI-6221). All the three generators and the DAQ card are synchronized together by the same clock signal. The final input waveform is captured at the AC+DC port of bias tee by the Tektronix DPO72004B storage oscilloscope with 50GHz sampling rate. It is plotted in Fig. 6.4 (b).

6.3 Results and discussion

Fig. 6.5 (a) shows the schematic figure of the waveforms we applied during the experiment. As marked in the figure, the amplitude of the square pulse is named as V_{dc} and the pulse width t_{pulse} is fixed as $1\ \mu s$. The sinusoid wave magnitude is V_{ac}. Another shorter square pulse is applied before the switching pulse to reset the sample. The R-H loop of the device (50 nm×130nm×2nm) is given in Fig. 6.5 (b) with the TMR ratio of 104.5% and coercivity of 42 Oe. During the switching probability measurement, a small external field is applied to center the hysteresis loop.

Since the STT induced magnetization switching is probabilistic, I characterized the switching probability (1000 trials per point) in order to precisely determine the switching voltage. The results are plotted in Fig. 6.5 (c) and (d). All the labeled voltage values are the actual voltage on the sample by multiplying the setting voltage with transmission coefficient (Eq.(4.1)).

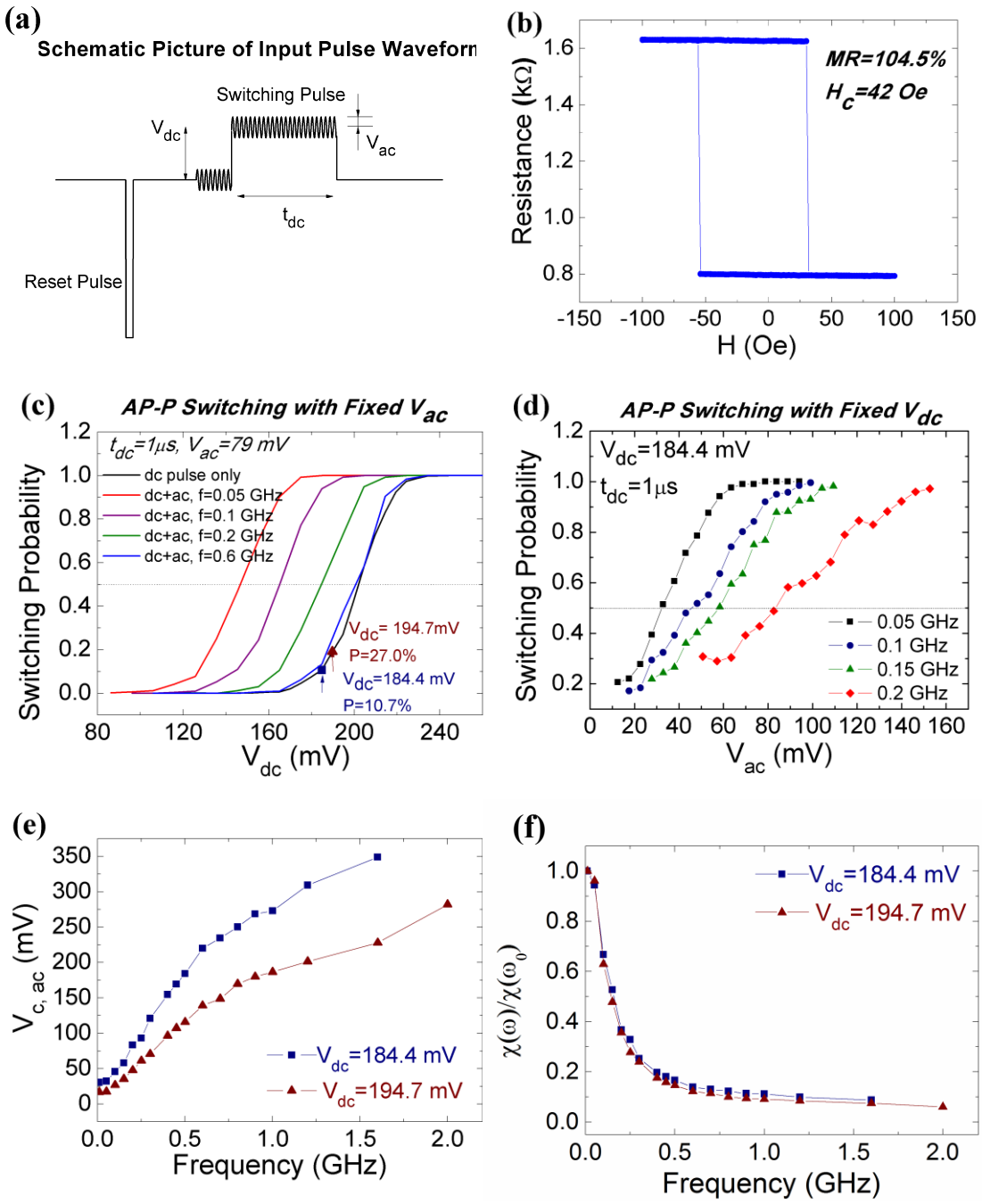

Fig. 6.5 (a) the schematic picture of the input pulse waveform; (b) MTJ resistance versus magnetic field loop, sample size; 50nm*130nm*2nm; (c) the switching probability curve of AP-P switching with fixed V_{ac}; (d) the switching probability curve of AP-P switching with fixed V_{dc}; (e) the AC critical voltage $V_{c,ac}$ as a function of AC excitation frequency; (f) the normalized FD-MLS value as a function of AC excitation frequency.

First, check the AP-P switching probability with a fixed AC wave magnitude (Fig. 6.5(c)). At V_{dc}=170 mV, with the AC excitations of 0.1 GHz and 0.2 GHz, the switching probabilities (p) are 0.604 and 0.158 respectively. This example shows the invalidation of Eq.(6.4). The two AC waves have the same amplitude of 79 mV, but different frequencies $f_2=2f_1$. The initial states and the total excitation time are the same m_i=1, NT=1 μs. If Eq.(6.4) is valid, the final states m_f will also be the same. However, the measured final states (m_f= 2p-1) are 0.208 and -0.684 for the two AC waves respectively. This example shows clearly that the simple approach based on the static energy barrier analysis is insufficient. The detailed magnetization dynamics in time-domain should also be considered.

The data in Fig. 6.5 (c) can further be used to estimate the dynamic reversal barrier reduction under different frequency excitations. The critical voltage is defined as the voltage value at 50% switching probability. Without the AC excitation, the DC critical voltage $V_{c,dc}$ is 202.0 mV at 1 μs (black curve). The intrinsic critical voltage $V_{c0,dc}$ of this sample is 328.0 mV by extrapolating the critical voltage versus time curve to t=1 ns. Assuming the static reversal barrier reduction is scaled by the DC pulse amplitude as $\Delta\varepsilon_0(1-V_{dc}/V_{c0,dc})$[31,112], we are able to approximately estimate the dynamic reversal barrier reduction from the AC excitation. For example, without the AC wave, the reversal barrier reduction as a result of DC voltage and thermal noise are $(V_{c,dc}/V_{c0,dc})\Delta\varepsilon_0$=0.616$\Delta\varepsilon_0$ and $(1-V_{c,dc}/V_{c0,dc})\Delta\varepsilon_0$=0.384$\Delta\varepsilon_0$, respectively. When the AC wave is present, the curves shift to left, which means that the DC voltage induced reversal barrier reduction is smaller than 0.616$\Delta\varepsilon_0$. Thus, there must be an extra reduction of the dynamic reversal barrier

results from the AC excitations. Moreover, the dynamic reversal barrier reduction from the AC excitation is proportional to the DC critical voltage drop, i.e. $ac\ reduction = \Delta\varepsilon_0\left(V_{c,dc}(without\ ac) - V_{c,dc}(with\ ac)\right)/V_{c0,dc}$. For example, in Fig. 6.5 (c), for the AC excitation with frequencies of 0.05 GHz, 0.1 GHz, 0.2 GHz and 0.6 GHz, the dynamic reversal barrier reductions are $0.232\Delta\varepsilon_0$, 0.155 $\Delta\varepsilon_0$, $0.075\Delta\varepsilon_0$ and $0.007\Delta\varepsilon_0$, respectively. This agrees well with the previous discussion that the reversal barrier reduction effect decreases with the driving frequency.

To better calibrate the effect of the AC excitation induced reversal barrier reduction, I fix the DC pulse amplitude and vary and the AC wave magnitude, so the linearly scaling assumption used in the previous paragraph ($\Delta\varepsilon_0(1-V_{dc}/V_{c0,dc})$) can be avoided. Two DC pulse amplitude values (184.4 mV and 194.7 mV) are chosen with less than 50% switching probability as marked on the black curve in Fig. 6.5 (c). Fig. 6.5 (d) shows four example switching probability curves with fixed V_{dc} (184.4 mV). We still define the critical AC voltage $V_{c,ac}$ as the value at 50% switching probability. The results are plotted in Fig. 6.5 (e). Now the reversal barrier reduction from the thermal fluctuation and DC pulse are both fixed; thus, the contribution from the AC excitation should also be constant at various frequencies. According to Eq.(6.7), for two different AC excitations (ω_1 and ω_2), we have

$$\left|\delta\varepsilon_{ac}\right| = \beta_1\left|\hat{\chi}(\omega_1)\right| = \beta_2\left|\hat{\chi}(\omega_2)\right|$$
$$so,\quad \frac{\left|\hat{\chi}(\omega_2)\right|}{\left|\hat{\chi}(\omega_1)\right|} = \frac{\beta_1}{\beta_2} = \frac{V_{ac1}}{V_{ac2}} \quad . \tag{6.9}$$

Therefore, the FD-MLS can be obtained through the measured critical AC voltage $V_{c,ac}$. The normalized FD-MLS ($\hat{\chi}(\omega)/\hat{\chi}(\omega_0)$,where $\omega_0=2\pi \times 0.05$ GHz) is shown in Fig. 6.5 (f). The roll-off trend of the measured FD-MLS agrees with the theoretical predictions in Ref. 110. It is also worth noting that despite the large discrepancy of $V_{c,ac}$ under the two DC pulse amplitudes in Fig. 6.5 (e), the normalized FD-MLS values are consistent. This proves the previous discussion that $\chi(t)$ and $\hat{\chi}(\omega)$ are intrinsic properties and independent from any external excitation sources.

Next, we continue to verify the magnetization logarithmic susceptibility theory by comparing the simulated magnetization logarithmic susceptibility value with experimental results. The magnetization logarithmic susceptibility simulation was done by Dr. Xiaobin Wang. It is proved as an effective method to characterize the magnetic properties of MTJ samples and provide insights to understand its STT switching dynamics.

I repeated the measurement in the previous section on three other MTJs with various lateral aspect ratios. The normalized FD-MLS values versus frequency were plotted for all three samples together in Fig. 6.6. It's clear that the roll-off of the FD-MLS with frequency is insensitive to the device lateral aspect ratio. This is understandable since the shape anisotropy is dominated by the out-of-plane demagnetization field. To compare the experimental result with theory, the theoretical FD-MLS curves are also shown in Fig. 6.6. They were calculated with the input parameters of *Ms*=1200 emu/cc, size=50 nm×150nm×2nm, interface anisotropy field =10732 Oe, and α=0.01, 0.015, 0.02. Unlike its response to the lateral aspect ratio, the FD-MLS is very sensitive to the damping

constant. We can thus use it to estimate the damping constant of our samples. The damping constant of CoFeB thin film at this thickness is about 0.01 as reported by Ikeda *et al*[69]. In our measurement, we can see that the measured results are also close to the α =0.01 curve. The slight discrepancy between the theory and experiment may come from the spin wave generation or side-wall damage in the patterned MTJ nano-pillar. It is also worth pointing out that our present model does not include the non-coherent switching effect[96,113], which may further account for the deviation between the experimental data and theoretical curve.

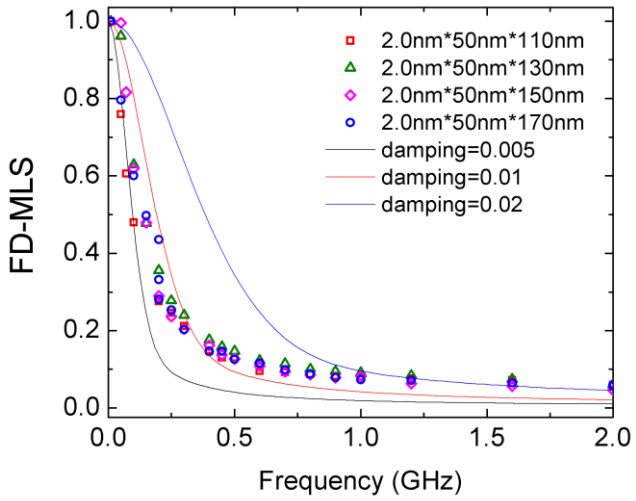

Fig. 6.6 The normalized FD-MLS dependence on frequency. For each sample, the curve is normalized by its own $\hat{\chi}(\omega_0)$. The points are experimental data and the solid curves are the theoretical results with Ms=1000 emu/cc and $H_{\perp}$=10732 Oe.

We further apply this method to investigate the interface perpendicular anisotropy of these MTJs. The normalized FD-MLS data measured in MTJs with different free layer thicknesses are shown in Fig. 6.7 (a). As the theory predicts (Fig. 6.7 (b)), the larger the interface perpendicular anisotropy field, the quicker the FD-MLS value decreases with

the frequency. Our experimental results show the same trend as the theory, but cannot be fitted well enough by the current model. The experiment data show less sensitivity to the free layer thickness or $H_{\perp}$ comparing to the simulation results. The discrepancy may come from the limitation of the macrospin model which treats the free layer as a single spin. One hypothesis is the micromagnetic non-uniformity of the free layer local spins. Although we use $H_{\perp}$ to describe the perpendicular interface anisotropy strength of the free layer, it is calculated from averaging the intrinsic perpendicular anisotropy by the free layer thickness: $H_{\perp}=2K_i/M_st$, where K_i is the interface perpendicular anisotropy, M_s is the saturation magnetization and t is the free layer thickness. The local spins near the interface always sense the same intrinsic perpendicular interface anisotropy energy K_i regardless of the free layer thickness. Therefore, those local spins near the interface has less sensitivity to the thin film thickness when we treat the free layer micromagnetically instead of as a macrospin. Considering the STT effect is dominant exactly by those local spins near the interface, the experimental data thus depends less on the free layer thickness comparing to the macrospin modeling results. Another hypothesis is the non-coherent STT switching when the out-of-plane demagnetization field is almost canceled by the perpendicular interface anisotropy in the case of the thinner free layer[96].

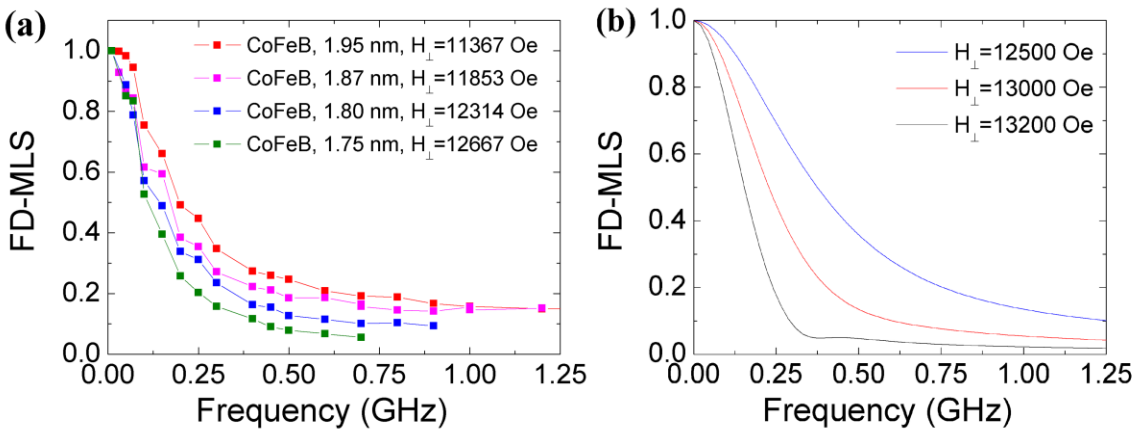

Fig. 6.7 (a) The normalized FD-MLS dependence on frequency with free layer thickness from 1.75 nm to 1.95 nm. Lateral size: 150nm*50nm. (b) Theoretical FD-MLS with various interface perpendicular anisotropy. Ms=1200 emu/cc, α=0.01.

6.4 Summary

We proved both theoretically and experimentally that the conventional escape rate estimation based on the static energy barrier over thermal Boltzmann factor without considering detailed magnetization dynamics is insufficient to characterize the long time nonvolatility of a magnetic system under high frequency excitations. Direct and compelling experimental evidence was provided to show the large dynamic energy barrier reduction induced by high frequency spin current excitations. This finding is useful for many magnetic and spintronic device applications that work in frequently disturbed conditions such as the memory bit in STT-RAM, the read head in hard disk drive, and other magnetic sensors. For those cases, dynamic energy barrier reduction caused by the extra disturbance in its working condition should be included when evaluating its thermal stability performance.

The concept of magnetization logarithmic susceptibility, which stands for the ratio of the dynamic energy barrier reduction to the sinusoid excitation amplitude, was proposed here to describe this dynamic effect. It was measured by calibrating the magnetization switching probabilities under radio frequency spin current excitations. The measured logarithmic susceptibility frequency response was used to characterize the magnetic properties of MTJs and understand the spin-transfer torque induced magnetization switching dynamics.

7 Conclusion

This thesis describes experimental studies of the spin transfer torque induced switching in MTJ for the application of STT-RAM.

In the material development; I started from the in-plane MTJ optimization in MgO barrier thickness, junction size and CoFeB free layer thickness in order to meet the requirement of STT-RAM application. Since the perpendicular anisotropy MTJ is favored over the conventional in-plane MTJ for its advantage in further scaling down the device and saving writing energy while maintaining thermal stability, I also worked on developing the perpendicular anisotropy in $L1_0$ phase FePd and CoFeB thin films. In the first work, perpendicular $L1_0$ phase FePd top MTJ electrode and bottom MTJ electrode were successfully fabricated in our sputtering system. In the second work, full CoFeB MTJ with interface perpendicular anisotropy was developed. It has been proven that the interface perpendicular anisotropy can effective reduce the intrinsic critical current density by canceling the out-of-plane demagnetizing field. An average of 48% reduction in the intrinsic critical current density was found by increasing the interface perpendicular anisotropy. Because of this successful material development, I was also able to demonstrate the sub 200 ps ultrafast STT induced switching in the CoFeB MTJs with partially canceled out-of-plane demagnetizing field. High J/J_{c0} ratio and magnetization nucleation at the edge of free layer, which both result from the interface perpendicular anisotropy are possibly two major factors that contribute to the ultrafast spin transfer torque switching.

In the STT induced switching study; I did systematic characterization of the probabilistic STT induced switching process. It started from the measurement of the three STT induced switching modes, the writing energy and writing speed. The results agree with the classic macrospin model. The work was continued by the high precision switching probability density function characterization. Based on the results, the skew normal distribution function was proposed to be used to fit the PDF function and extrapolate the read disturb rate and write error rate. Moreover, I also studied the temperature dependences of the TMR ratio, coercivity, thermal stability factor and switching current distribution in the temperature range of 25–80 ◦C, the most probable working environment for STT-RAM application. In the end, I discussed the large dynamic energy barrier reduction induced by high frequency spin current excitations. The concept of magnetization logarithmic susceptibility, which stands for the ratio of the dynamic energy barrier reduction to the sinusoid excitation amplitude, was proposed here to describe this dynamic effect. By comparing with the simulation results, the measured logarithmic susceptibility frequency response was used to characterize the magnetic properties of MTJs and understand the spin-transfer torque induced magnetization switching dynamics.

Bibliography

1. Julliere, M. Tunneling between ferromagnetic films. *Physics Letters A* **54,** 225–226 (1975).
2. Miyazaki, T. & Tezuka, N. Giant magnetic tunneling effect in Fe/Al2O3/Fe junction. *Journal of Magnetism and Magnetic Materials* **139,** L231–L234 (1995).
3. Miyazaki, T. & Tezuka, N. Spin polarized tunneling in ferromagnet/insulator/ferromagnet junctions. *Journal of Magnetism and Magnetic Materials* **151,** 403–410 (1995).
4. Moodera, J. S., Kinder, L. R., Wong, T. M. & Meservey, R. Large Magnetoresistance at Room Temperature in Ferromagnetic Thin Film Tunnel Junctions. *Physical Review Letter*s **74,** 3273–3276 (1995).
5. Wang, D., Nordman, C., Daughton, J. M., Qian, Z. & Fink, J. 70% TMR at room temperature for SDT sandwich junctions with CoFeB as free and reference Layers. *IEEE Transactions on Magnetics* **40,** 2269 – 2271 (2004).
6. Yuasa, S., Nagahama, T., Fukushima, A., Suzuki, Y. & Ando, K. Giant room-temperature magnetoresistance in single-crystal Fe/MgO/Fe magnetic tunnel junctions. *Nature materials* **3,** 868–871 (2004).
7. Parkin, S. S. *et al.* Giant tunnelling magnetoresistance at room temperature with MgO (100) tunnel barriers. *Nature materials* **3,** 862–867 (2004).
8. Ikeda, S. *et al.* Tunnel magnetoresistance of 604% at 300 K by suppression of Ta diffusion in CoFeB/MgO/CoFeB pseudo-spin-valves annealed at high temperature. *Applied Physics Letters* **93,** 082508–3 (2008).
9. Butler, W. H., Zhang, X.-G., Schulthess, T. C. & MacLaren, J. M. Spin-dependent tunneling conductance of Fe| MgO| Fe sandwiches. *Physical Review B* **63,** 054416 (2001).
10. Mathon, J. & Umerski, A. Theory of tunneling magnetoresistance of an epitaxial Fe/MgO/Fe(001) junction. *Physical Review B* **63,** 220403 (2001).
11. Berger, L. Low-field magnetoresistance and domain drag in ferromagnets. *Journal of Applied Physics* **49,** 2156–2161 (1978).
12. Berger, L. Domain drag effect in the presence of variable magnetic field or variable transport current. *Journal of Applied Physics* **50,** 2137–2139 (1979).

13. Freitas, P. P. & Berger, L. Observation of s-d exchange force between domain walls and electric current in very thin Permalloy films. *Journal of Applied Physics* **57,** 1266–1269 (1985).

14. Hung, C.-Y. & Berger, L. Exchange forces between domain wall and electric current in permalloy films of variable thickness. *Journal of Applied Physics* **63,** 4276–4278 (1988).

15. Myers, E. B., Ralph, D. C., Katine, J. A., Louie, R. N. & Buhrman, R. A. Current-Induced Switching of Domains in Magnetic Multilayer Devices. *Science* **285,** 867–870 (1999).

16. Gan, L., Chung, S. H., Aschenbach, K. H., Dreyer, M. & Gomez, R. D. Pulsed-current-induced domain wall propagation in Permalloy patterns observed using magnetic force microscope. *IEEE Transactions on Magnetics* **36,** 3047 –3049 (2000).

17. Ono, T. *et al.* Magnetization reversal and electric transport in ferromagnetic nanowires. *Materials Science and Engineering: B* **84,** 126–132 (2001).

18. Grollier, J. *et al.* Switching the magnetic configuration of a spin valve by current-induced domain wall motion. *Journal of Applied Physics* **92,** 4825–4827 (2002).

19. Kläui, M. *et al.* Domain wall motion induced by spin polarized currents in ferromagnetic ring structures. *Applied Physics Letters* **83,** 105–107 (2003).

20. Tsoi, M., Fontana, R. E. & Parkin, S. S. P. Magnetic domain wall motion triggered by an electric current. *Applied Physics Letters* **83,** 2617–2619 (2003).

21. Beach, G. S. D., Tsoi, M. & Erskine, J. L. Current-induced domain wall motion. *Journal of Magnetism and Magnetic Materials* **320,** 1272–1281 (2008).

22. Parkin, S. S. P. Shiftable magnetic shift register and method of using the same. (2004). at <http://www.google.com/patents/US6834005>

23. Parkin, S. S. P., Hayashi, M. & Thomas, L. Magnetic Domain-Wall Racetrack Memory. *Science* **320,** 190–194 (2008).

24. Slonczewski, J. C. Conductance and exchange coupling of two ferromagnets separated by a tunneling barrier. *Physical Review B* **39,** 6995 (1989).

25. Berger, L. Emission of spin waves by a magnetic multilayer traversed by a current. *Physical Review B* **54,** 9353–9358 (1996).

26. Slonczewski, J. C. Current-driven excitation of magnetic multilayers. *Journal of Magnetism and Magnetic Materials,* **159,** L1–L7 (1996).

27. Slonczewski, J. C. Currents, torques, and polarization factors in magnetic tunnel junctions. *Physical Review B* **71,** 024411 (2005).

28. Tsoi, M. *et al.* Excitation of a Magnetic Multilayer by an Electric Current. *Physical Review Letter,* **80,** 4281–4284 (1998).

29. Sun, J. Z. Current-driven magnetic switching in manganite trilayer junctions. *Journal of Magnetism and Magnetic Materials.* **202,** 157–162 (1999).

30. Katine, J. A., Albert, F. J., Buhrman, R. A., Myers, E. B. & Ralph, D. C. Current-Driven Magnetization Reversal and Spin-Wave Excitations in Co /Cu /Co Pillars. *Physical Review Letters* **84,** 3149–3152 (2000).

31. Koch, R. H., Katine, J. A. & Sun, J. Z. Time-Resolved Reversal of Spin-Transfer Switching in a Nanomagnet. *Physical Review Letters,* **92,** 088302 (2004).

32. Katine, J. A. & Fullerton, E. E. Device implications of spin-transfer torques. *Journal of Magnetism and Magnetic Materials* **320,** 1217–1226 (2008).

33. Huai, Y. Spin-transfer torque MRAM (STT-MRAM): Challenges and prospects. *AAPPS Bulletin* **18,** 33–40 (2008).

34. Kawahara, T. *et al.* 2 Mb SPRAM (SPin-Transfer Torque RAM) With Bit-by-Bit Bi-Directional Current Write and Parallelizing-Direction Current Read. *IEEE Journal of Solid-State Circuits* **43,** 109 –120 (2008).

35. Silva, T. J. & Rippard, W. H. Developments in nano-oscillators based upon spin-transfer point-contact devices. *Journal of Magnetism and Magnetic Materials* **320,** 1260–1271 (2008).

36. Wang, C. *et al.* Sensitivity of spin-torque diodes for frequency-tunable resonant microwave detection. *Journal of Applied Physics* **106,** 053905–053905–6 (2009).

37. Xia, K., Kelly, P. J., Bauer, G. E. W., Brataas, A. & Turek, I. Spin torques in ferromagnetic/normal-metal structures. *Physical Review B* **65,** 220401 (2002).

38. Stiles, M. D. & Zangwill, A. Anatomy of spin-transfer torque. *Physical Review B* **66,** 014407 (2002).

39. Zwierzycki, M., Tserkovnyak, Y., Kelly, P. J., Brataas, A. & Bauer, G. E. W. First-principles study of magnetization relaxation enhancement and spin transfer in thin magnetic films. *Physical Review B* **71,** 064420 (2005).

40. Kubota, H. *et al.* Quantitative measurement of voltage dependence of spin-transfer torque in MgO-based magnetic tunnel junctions. *Nature Physics* **4,** 37–41 (2008).

41. Sankey, J. C. *et al.* Measurement of the spin-transfer-torque vector in magnetic tunnel junctions. *Nature Physics* **4,** 67–71 (2008).

42. Li, Z. *et al.* Perpendicular Spin Torques in Magnetic Tunnel Junctions. *Physical Review Letters* **100,** 246602 (2008).

43. Zhang, S., Levy, P. M. & Fert, A. Mechanisms of Spin-Polarized Current-Driven Magnetization Switching. *Physical Review Letters* **88,** 236601 (2002).

44. Landau, L. D. & Lifshitz, E. M. On the Theory of the Dispersion of Magnetic Permeability in Ferromagnetic Bodies. *Physics Z. Sowjetunion* **8,** 153 (1935).

45. Gilbert, T., L. Armour research foundation project No. A059, Supplementary Report. (1956).

46. Gilbert, T. L. A phenomenological theory of damping in ferromagnetic materials. *IEEE Transactions on Magnetics* **40,** 3443 – 3449 (2004).

47. Sun, J. Z. Spin-current interaction with a monodomain magnetic body: A model study. *Physical Review B* **62,** 570 (2000).

48. Mangin, S. *et al.* Current-induced magnetization reversal in nanopillars with perpendicular anisotropy. *Nature Materials* **5,** 210–215 (2006).

49. Raychowdhury, A., Somasekhar, D., Karnik, T. & De, V. Design space and scalability exploration of 1T-1STT MTJ memory arrays in the presence of variability and disturbances. *Electron Devices Meeting (IEDM), 2009 IEEE International* 1 –4 (2009). doi:10.1109/IEDM.2009.5424242

50. Driskill-Smith, A. *et al.* Non-volatile spin-transfer torque RAM (STT-RAM): Data, analysis and design requirements for thermal stability. *2010 Symposium on VLSI Technology (VLSIT)* 51 –52 (2010). doi:10.1109/VLSIT.2010.5556124

51. Lee, Y. M. *et al.* Highly scalable STT-MRAM with MTJs of top-pinned structure in 1T/1MTJ cell. *2010 Symposium on VLSI Technology (VLSIT)* 49 –50 (2010). doi:10.1109/VLSIT.2010.5556123

52. Min, T. *et al.* A Study of Write Margin of Spin Torque Transfer Magnetic Random Access Memory Technology. *IEEE Transactions on Magnetics* **46,** 2322 –2327 (2010).

53. Heindl, R., Rippard, W. H., Russek, S. E., Pufall, M. R. & Kos, A. B. Validity of the thermal activation model for spin-transfer torque switching in magnetic tunnel junctions. *Journal of Applied Physics* **109,** 073910–5 (2011).

54. Nowak, J. J. *et al.* Demonstration of Ultralow Bit Error Rates for Spin-Torque Magnetic Random-Access Memory With Perpendicular Magnetic Anisotropy. *IEEE Magnetics Letters* **2,** 3000204 (2011).

55. Gajek, M. *et al.* Spin torque switching of 20 nm magnetic tunnel junctions with perpendicular anisotropy. *Applied Physics Letters* **100,** 132408–132408–3 (2012).

56. Kawahara, T., Ito, K., Takemura, R. & Ohno, H. Spin-transfer torque RAM technology: Review and prospect. *Microelectronics Reliability* **52,** 613–627 (2012).

57. Chen, E. *et al.* Advances and Future Prospects of Spin-Transfer Torque Random Access Memory. *IEEE Transactions on Magnetics* **46,** 1873 –1878 (2010).

58. Myers, E. B. *et al.* Thermally Activated Magnetic Reversal Induced by a Spin-Polarized Current. *Physical Review Letters* **89,** 196801 (2002).

59. Li, Z. & Zhang, S. Thermally assisted magnetization reversal in the presence of a spin-transfer torque. *Physical Review B* **69,** 134416 (2004).

60. at <http://www.d2inlinesolutions.com/technology/sputtering.html>

61. Simmons, J. G. Generalized Formula for the Electric Tunnel Effect between Similar Electrodes Separated by a Thin Insulating Film. *Journal of Applied Physics* **34,** 1793–1803 (1963).

62. Zeng, Z. M. *et al.* Effect of resistance-area product on spin-transfer switching in MgO-based magnetic tunnel junction memory cells. *Applied Physics Letters* **98,** 072512–072512–3 (2011).

63. Weller, D. *et al.* High Ku materials approach to 100 Gbits/in2. *IEEE Transactions on Magnetics* **36,** 10–15 (2000).

64. Klemmer, T., Hoydick, D., Okumura, H., Zhang, B. & Soffa, W. A. Magnetic hardening and coercivity mechanisms in L10 ordered FePd ferromagnets. *Scripta Metallurgica et Materialia* **33,** 1793–1805 (1995).

65. Ha, J. G. *et al.* Structure and magnetic anisotropy in L10 ordered FePd thin films. *physica status solidi (a)* **204,** 4045–4048 (2007).

66. Chiang, C. C., Lai, C.-H. & Wu, Y. C. Low-temperature ordering of L1[sub 0] FePt by PtMn underlayer. *Applied Physics Letters* **88,** 152508 (2006).

67. Xu, Y., Chen, J. S. & Wang, J. P. In situ ordering of FePt thin films with face-centered-tetragonal (001) texture on Cr100−xRux underlayer at low substrate temperature. *Applied Physics Letters* **80,** 3325–3327 (2002).

68. Ravelosona, D. *et al.* Chemical ordering at low temperatures in FePd films. *Journal of Applied Physics* **91,** 8082–8084 (2002).

69. Ikeda, S. *et al.* A perpendicular-anisotropy CoFeB–MgO magnetic tunnel junction. *Nature Materials* **9,** 721–724 (2010).

70. Khalili Amiri, P. *et al.* Switching current reduction using perpendicular anisotropy in CoFeB–MgO magnetic tunnel junctions. *Applied Physics Letters* **98,** 112507 (2011).

71. Bedau, D. *et al.* Ultrafast spin-transfer switching in spin valve nanopillars with perpendicular anisotropy. *Applied Physics Letters* **96,** 022514–3 (2010).

72. Zhao, H. *et al.* Low writing energy and sub nanosecond spin torque transfer switching of in-plane magnetic tunnel junction for spin torque transfer random access memory. *Journal of Applied Physics* **109,** 07C720–07C720–3 (2011).

73. Diao, Z. *et al.* Spin-transfer torque switching in magnetic tunnel junctions and spin-transfer torque random access memory. *Journal of Physics: Condensed Materials.* **19,** 165209 (2007).

74. Heindl, R., Rippard, W. H., Russek, S. E. & Kos, A. B. Physical limitations to efficient high-speed spin-torque switching in magnetic tunnel junctions. *Physical Review B* **83,** 054430 (2011).

75. Heindl, R., Rippard, W. H., Russek, S. E., Pufall, M. R. & Kos, A. B. Validity of the thermal activation model for spin-transfer torque switching in magnetic tunnel junctions. *Journal of Applied Physics,* **109,** 073910–5 (2011).

76. Seki, T. Switching-probability distribution of spin-torque switching in MgO-based magnetic tunnel junctions. *Applied Physics Letters,* **99,** 112504 (2011).

77. Wang, X., Zheng, Y., Xi, H. & Dimitrov, D. Thermal fluctuation effects on spin torque induced switching: Mean and variations. *Journal of Applied Physics,* **103,** 034507 (2008).

78. Pakala, M. Critical current distribution in spin-transfer-switched magnetic tunnel junctions. *Journal of Applied Physics,* **98,** 056107 (2005).

79. Higo, Y. Thermal activation effect on spin transfer switching in magnetic tunnel junctions. *Applied Physics Letters,* **87,** 082502 (2005).

80. Zhao, H. *et al.* Spin-Torque Driven Switching Probability Density Function Asymmetry. *IEEE Transactions on Magnetics* **48,** 3818–3820 (2012).

81. Krivorotov, I. N. *et al.* Temperature Dependence of Spin-Transfer-Induced Switching of Nanomagnets. *Physical Review Letters,* **93,** 166603 (2004).

82. Victora, R. H. Predicted time dependence of the switching field for magnetic materials. *Physical Review Letters,* **63,** 457–460 (1989).

83. Takemura, R. *et al.* TMR design methodology for SPin-transfer torque RAM (SPRAM) with nonvolatile and SRAM compatible operations. in *Non-Volatile Semiconductor Memory Workshop, 2008 and 2008 International Conference on Memory Technology and Design (NVSMW/ICMTD 2008)* 54–56 (2008).

84. Wang, X., Zhu, W., Siegert, M. & Dimitrov, D. Spin Torque Induced Magnetization Switching Variations. *IEEE Transactions on Magnetics,* **45,** 2038–2041 (2009).

85. Zhao, H. *et al.* Spin-Transfer Torque Switching Above Ambient Temperature. *IEEE Magnetics Letters* **3,** 3000304–3000304 (2012).

86. Devolder, T., Chappert, C., Katine, J. A., Carey, M. J. & Ito, K. Distribution of the magnetization reversal duration in subnanosecond spin-transfer switching. *Physical Review B* **75,** 064402 (2007).

87. Devolder, T. *et al.* Magnetization switching by spin torque using subnanosecond current pulses assisted by hard axis magnetic fields. *Applied Physics Letters* **88,** 152502–3 (2006).

88. Beaujour, J. M. L., Bedau, D. B., Liu, H., Rogosky, M. R. & Kent, A. D. Spin-transfer in nanopillars with a perpendicularly magnetized spin polarizer. in *Spintronics II* (Razeghi, M., Drouhin, H.-J. M. & Wegrowe, J.-E.) **7398,** 73980D–11 (SPIE, 2009).

89. Lee, O. J. *et al.* Ultrafast switching of a nanomagnet by a combined out-of-plane and in-plane polarized spin current pulse. *Applied Physics Letters* **95,** 012506–3 (2009).

90. Papusoi, C. *et al.* 100 ps precessional spin-transfer switching of a planar magnetic random access memory cell with perpendicular spin polarizer. *Applied Physics Letters* **95,** 072506–3 (2009).

91. Aoki, T., Ando, Y., Oogane, M. & Naganuma, H. Reproducible trajectory on subnanosecond spin-torque magnetization switching under a zero-bias field for MgO-based ferromagnetic tunnel junctions. *Applied Physics Letters* **96,** 142502–3 (2010).

92. Liu, H. *et al.* Ultrafast switching in magnetic tunnel junction based orthogonal spin transfer devices. *Applied Physics Letters* **97,** 242510–3 (2010).

93. Rowlands, G. E. *et al.* Deep subnanosecond spin torque switching in magnetic tunnel junctions with combined in-plane and perpendicular polarizers. *Applied Physics Letters* **98,** 102509–102509–3 (2011).

94. Upadhyaya, P. *et al.* Thermal Stability Characterization of Magnetic Tunnel Junctions Using Hard Axis Magnetoresistance Measurement. *55th MMM conference* **FP-13,** (2010).

95. Donahue, M. J. & Porter, D. G. *OOMMF User's Guide, Version 1.0*. (Interagency Report NISTIR 6376, National Institute of Standards and Technology, Gaithersburg, MD (Sept 1999)). at <http://math.nist.gov/oommf>

96. Zhao, H. *et al.* Sub-200 ps spin transfer torque switching in in-plane magnetic tunnel junctions with interface perpendicular anisotropy. *Journal of Physics D: Applied Physics,* **45,** 025001 (2012).

97. Kramers, H. A. Brownian motion in a field of force and the diffusion model of chemical reactions. *Physica* **7,** 284–304 (1940).

98. Graham, R. & Tél, T. Weak-noise limit of Fokker-Planck models and nondifferentiable potentials for dissipative dynamical systems. *Physical Review. A* **31,** 1109–1122 (1985).

99. Hänggi, P., Talkner, P. & Borkovec, M. Reaction-rate theory: fifty years after Kramers. *Review Modern Physics* **62,** 251–341 (1990).

100. Lehmann, J., Reimann, P. & Hänggi, P. Surmounting oscillating barriers. *Physical Review Letters,* **84,** 1639–1642 (2000).

101. Smelyanskiy, V. N., Dykman, M. I. & Golding, B. Time oscillations of escape rates in periodically driven systems. *Physical Review Letters,* **82,** 3193–3197 (1999).

102. Devoret, M. H., Martinis, J. M., Esteve, D. & Clarke, J. Resonant activation from the zero-voltage state of a current-biased Josephson junction. *Physical Review Letters,* **53,** 1260–1263 (1984).

103. Devoret, M. H., Esteve, D., Martinis, J. M., Cleland, A. & Clarke, J. Resonant activation of a Brownian particle out of a potential well: Microwave-enhanced escape from the zero-voltage state of a Josephson junction. *Physical Review B* **36,** 58–73 (1987).

104. Doering, C. R. & Gadoua, J. C. Resonant activation over a fluctuating barrier. *Physical Review Letters,* **69,** 2318–2321 (1992).

105. Cui, Y. T. *et al.* Resonant spin-transfer-driven switching of magnetic devices assisted by microwave current pulses. *Physical Review B* **77,** 214440 (2008).

106. Chen, W. *et al.* Effects of radio-frequency current on critical fields for magnetization reversal in spin-torque devices. *Physical Review B* **84,** 054459 (2011).

107. Florez, S. H. *et al.* Effects of radio-frequency current on spin-transfer-torque-induced dynamics. *Physical Review B* **78,** 184403 (2008).

108. Carpentieri, M., Finocchio, G., Azzerboni, B. & Torres, L. Spin-transfer-torque resonant switching and injection locking in the presence of a weak external microwave field for spin valves with perpendicular materials. *Physical Review B* **82,** 094434 (2010).

109. Finocchio, G., Krivorotov, I. N., Cheng, X., Torres, L. & Azzerboni, B. Micromagnetic understanding of stochastic resonance driven by spin-transfer-torque. *Physical Review B* **83,** 134402 (2011).

110. Wang, X., Zhu, W., Xi, H., Gao, Z. & Dimitrov, D. Magnetization logarithmic susceptibility, damping parameter, and dynamics symmetry extraction. *Applied Physics Letters* **93,** 182506–3 (2008).

111. Wang, X., Fernandez-de-Castro, J., Gao, K. & Jin, Z. Thermal reversal of magnetic grains under time varying pulse field. *IEEE Transactions on Magnetics* **42,** 2294–2296 (2006).

112. Li, Z. & Zhang, S. Thermally assisted magnetization reversal in the presence of a spin-transfer torque. *Physical Review B* **69,** 134416 (2004).

113. Sun, J. Z. *et al.* Effect of subvolume excitation and spin-torque efficiency on magnetic switching. *Physical Review B* **84,** 064413 (2011).

114. Zhu, J. *et al.* Voltage-Induced Ferromagnetic Resonance in Magnetic Tunnel Junctions. *Physical Review Letters* **108,** 197203 (2012).

115. Meng, H. *et al.* Electric field effects in low resistance CoFeB-MgO magnetic tunnel junctions with perpendicular anisotropy. *Applied Physics Letters* **100,** 122405–3 (2012).

Appendix A: MTJ nano-fabrication Run Sheet

NanoSize Spin-Dependent Tunneling Junction Fabrication Run-Sheet

Wafer: 4" Si No: Singulus 4.1.5 Date: 11th. Nov –

Step 1: Si wafer oxidation (clean-room bay 1)

Equipment: Tube 1

Conditions:

1000^{o} C in pure O_2

4 hours for 1000 Å SiO_2

Comment:

Step 2: MTJ structure and calibration sample deposition.

Equipment:

Conditions: (recipe, flow, sequence name, power, time, oxidation conditions, etc)

Flow name: MTJ

Recipe

Substrate

1. Ta (3 nm)
2. CuN (60 nm)
3. Ta (5 nm)
4. PtMn (15 nm)
5. $Co_{70}Fe_{30}$ (2.5 nm)
6. Ru (0.85 nm)
7. $Co_{40}Fe_{40}B_{20}$ (2.4 nm)
8. MgO
   (RA=8 ohm* um^2)
9. $Co_{60}Fe_{20}B_{20}$ (1.8 nm)
10. Ru (2 nm)
11. Ta (10 nm)
12. Au (150 nm)
13. Ta (10 nm)

Comment: total thickness=253.5 nm

Step 6: AJA deposite capping layer

Equipment: AJA

Condition:

☐Pre-sputter #3 -Ta #4-Au

☐Deposit #3 Ta

☐Deposit #4 Au

Comments:

Base Pressure 5 x10^{-8} Torr

Ta/Au/Ta 1700 A

Step 3: MTJ bottom electrode mask exposing. (clean-room, bay2)

Photo Resist Coating: (PR 1813)

Equipment: CEE Photo-resist Spinner

Condition:

☐Pre-bake 115^{o}C for 1 minute

☐Program 4: Coat PR1813 at 4000RPM 30 seconds (around 18000Å thick).

☐Soft Bake 105^{o}C for 1 minute

Comments: Soft bake is used before exposure. CEE **vacuum** test first!

Mask exposing (mask name: B-E LⅡ):

Equipment: KARL SUSS MA6

Condition: Program: Hard-Ct/cont.

☐ Time: 5.5 seconds, Distance 20 *u*m.

Comments: Facing words is film side. When loading mask, put film side up.
(First align mask, then move wafer to match the mask, and then look both sides.)
Check the initial position of the wafer holder.

Photo Resist developing:

☐Solution: H_2O:351=5:1 (wet bench) Time= 30 sec

☐Rinse tank, DI wafer rinse and N2 blow dry

☐Hard Bake: 120 ^{o}C time=1 minute

Comments:

Step 4: Bottom electrode definition (clean-room, bay3, ion milling).

Equipment: Ion Mill II ☐

Conditions: Base pressure: 8×10^{-6} Torr, Etching pressure: 8×10^{-5} Torr.
Beam voltage: 301V, Accelerate voltage: 100V, Current:9 mA.
Angle: 60^{o}

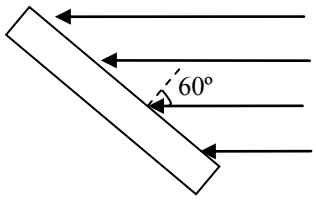

Ration: 4RPM, Time: 40 minutes (depend on total bottom layer thickness).

Comment: Etch till reaching SiO_2 substrate. Etch 3 min and stop 3 min.
over-etching may happen during the process, try best to protect it.

Total: 3 min *12 times +2 min = 38 min
Current: 72-74 mA

Step 5: Photo Resist Re-movement (clean-room, Bay 2)

Solution: Acetone.

Condition: Put Acetone into Ultrasonic(48%) for 10 minutes; DI water tank, DI water rinse, N2 blow dry ☐

Comments:

Recipe: O2CLN_50W, O_2 99.0 ±20%, no Ar, Power 50W, 1 min

Step 7: Step measurement

Equipment: surface profile

Step height: 1833A, 1855A, 1710A, 1712A, 1709A, 1720A, 1687A, 1708A

Step8: PMMA coating (spinner)

☐prebake 180°C-2 min;
☐**P.R 495K A4** 500RPM-8sec-3000RPM-45s,
☐softbake@180°C-1min;
☐**P.R. 950K PMMA C2** 500RPM-8sec-3000RPM-45s,
☐softbake@180°C-1min;

Comments:

Step 9: NanoSize MTJ masks exposing (clean-room, bay2).

Mask exposing (Raith 150) :

1) mark the XY axis using diamond pen (for whole wafer pattern, DONOT mark)

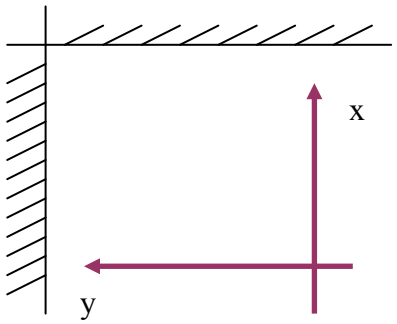

30KV, 10 um, I=__0.026___nA; dose=~250 uC/cm^2;
active "autofocus" function
High Res. Sample: **W=16mm**; WD=_10.9708_____mm;
Aper. X=_-14.9___%; Y=_16.299_____%;
Stig. X=_1.71423_____%; Y=__-3.7242_____%;
Sample surface, use **W=10.15 mm**; WD=_10.745-11.031____mm;

Comments:

- adjust focus, aperture, astigmatism using high resolution reference sample
- find origin in the sample, and focus the surface of the sample
- adjust the UV coordinates
- For large sample, adjust writing field alignment using three-point alignment

Point 1 (right 11)
U=24.54
V= - 0.2125
WD=10.745

Point 2 (left 11)
U= - 25.46
V= - 0.2125
WD=10.675

Point 3 (top 11)
U= - 0.46
V=24.7875
WD=11.03168

Step10 Ebeam Resist developing

Developer: IPA: DI water = 7:3,

☐ultrasonics bath @ 50% power for 50s.

☐ Immediately IPA clean for> 3 min, change rinse direction & angle

☐soft N2 blow dry; microscope

☐ STS Etching to clean the resist at the bottom. Recipe: Plannr 12, Time: 6 s

Comments:

Step11: Ti deposition (EB evaporator)

Ti thickness: ~60 nm (depend on etched layer thickness);
rate: 0.2 nm/sec

Put a test sample to monitor Ti thickness
Test the thickness of the Ti. (The thermal evaporate deposition made the film rough and the pro16 can't measure the thickness well. The XRR is recommended for this thickness measurement.)

Step 12 Lift-off

- Sonicate the sample @ Acetone bath with 44% power for ~30 min +
- DI rinse, soft N2 blow dry

Comment： Checked pillar by SEM (Raith 150).

Step13: Pillar Etching (clean room, bay3, ion mill)

Equipment: Ion Mill
Pillar etching = top lead + pillar
Conditions: Base pressure: _6×10^{-6} Torr, Etching pressure: _8×10^{-5} Torr.
Beam voltage: _300__V, Accelerate voltage: _100_V,
Current: _72-74_mA.
Angle: 30^{o} +60^{o}
Ration: 4RPM

Comments: put the ref sample to etch together. Etch 3 min and stop 3 min.

- Started at 30^{o}
  - 3 min * 4 times - Reaches CuN layer
  - + 3 min * 2 times - CuN layer totally gone.
  - + 3 min - Ref sample very thin
- Switched to 30^{o}
  - + 3 min - ref sample gone
  - + 3 min - done.

Step14: Step height measurement and thickness measurement

Measure the BL height (in Å):

Center: 891, 883
Midway between center and edge": 940, 980, 954
Edge: 973, 1124, 1053

Shoulder: 369, 410

Measure the testing pillar height (in Å):
2414, 2298, 2205, 2303, 2365,2304
Ave: 2314

the remaining thickness of the SiO_2 (in Å):

Center: 668, 665,650,662,653
Edge: 518, 414, 453, 450, 451

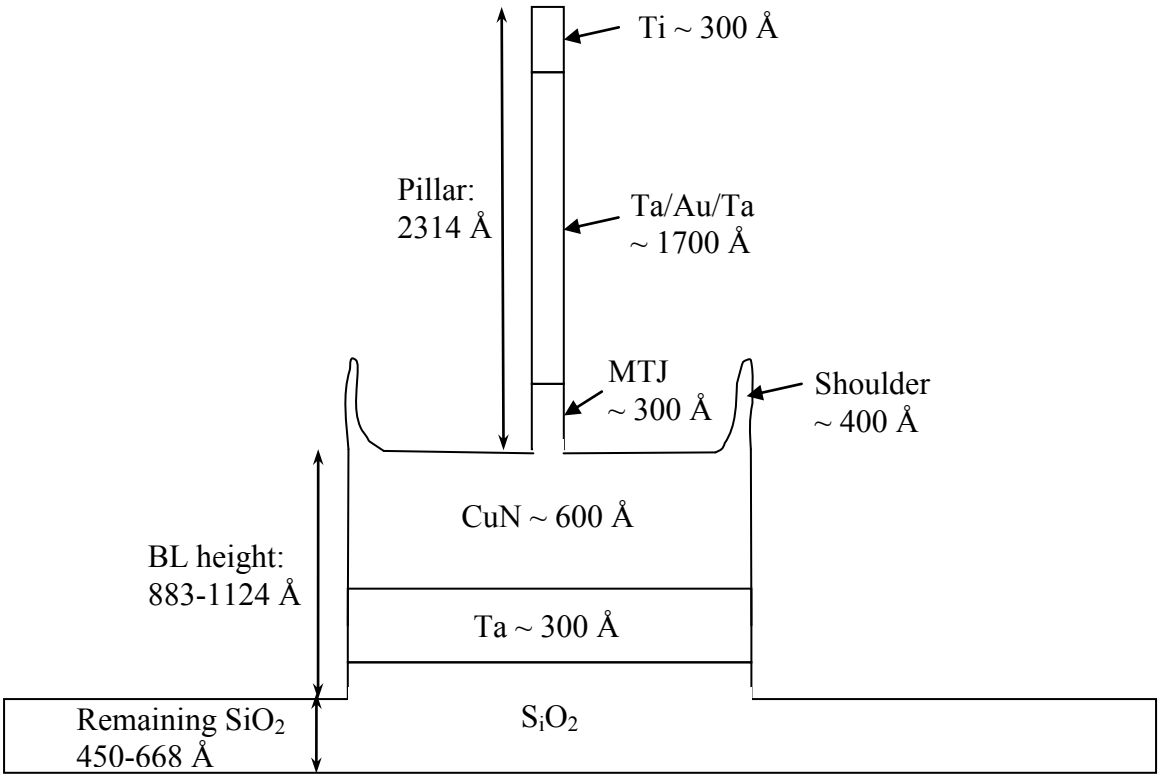

Step15: SiO2 deposit PECVD

Recipe: SiO2150; thickness is 1000 Å higher than the stack height

Comments: depends on the Ti thickness measurement OR the testing pillar height (rate: 353 Å ~377 Å /min)

Actual Time: 12 min 30 s.

Step16: SiO2 measurement

#1 measure the SiO2 thickness on the wafer

Recipe: SiO2 on thermal SiO2 on Si

Center: 5034, 5012, 5017, 5008 (in Å)
Edge: 4927, 4985, 5032, 4996, 4927 (in Å)
Average: 4993 Å

#2 measure the BL step

Center: 965, 986 (in Å)
Edge: 1183, 1207 (in Å)

Step 17: Bottom leads edge cover PR spin

Photo Resist Coating:

Equipment: CEE Photoresist Spinner(Double layers: SF 5, PR 1813)
Condition: **SF5:**
☐Pre-bake 170^{o}C for 5 minute (to remove H2O totally), cool down for a few sec.
☐Program 9: 500RPM/500RPM (acc)-10sec/4000RPM/4000PRM (acc)-35sec.
☐Bake at 150^{o}C for 5 minute
PR1813:
☐Program 4: Coat PR1813 at 4000RPM 30 seconds
☐Soft Bake 105^{o}C for 1 minute

Comments: CEE **vacuum** test first
Pure SF 5 need to be quick, pure it in the center.

Mask exposing (mask name: L4) :

Equipment: KARLSUSS MAB6
Condition: Program: Hard-Ct/cont.
☐Time: 5seconds, Distance 20 *u*m, Power: 12mW/cm^2

Photo Resist developing:

Solution: MF319 (avoid water)
Condition:
☐Clean beaker: use DI water and MF319 to clean the beaker and blow dry
☐MF319 time: 1.5 min
☐DI water rinse and N2 blow dry.
☐Microscope: to check if the pillar shape is good
☐Hard Bake: 120°C for 1 min.

Step18: Bottom leads edge SiO2 cover deposited E-beam evaporator

Thickness: 1000 Å

Step 19: lift-off

Solution: Developer 1165
Condition: 1165 heat at 80 degree. Put it in ultrasonic if necessary.

Step20: Photo Resist Coating for planarization

Prebake @ 150 °C for 5 min;
HMDS 30min;
1805 coating: spray @ 500RPM for 10s then 4000RPM for 30s

Surface flat baking: 50C for 3min; 105C for 1min

Measure photoresist 1805 thickness: 4167 Å
Ellipsometer------Recipe: resist on SiO_2 on thermal SiO_2 on Si

Step21: Planarization

Resist etch: RIE
Recipe: **planr12**: Ar 70sccm, CF 47sccm, CHF3 6sccm for **10 min**
(photoresist etching rate **(~250 Å /min)**)

* Resist thickness: Measure remaining 1805 thickness:
Ellipsometer: Recipe: resist on SiO_2 on thermal SiO_2 on Si

Remaining PR 1805 thickness: 1775, 1817, 1821, 1692, 1695, 1838, 1707, 1763 (in Å)
Average: 1746 Å
Actual PR 1805 etching rate: 240.6 Å/min

Etching resist and SiO_2: RIE
Recipe: **planr12**: Ar 70sccm, CF 47sccm, CHF3 6sccm for **10 min**

*Measure remaining SiO_2 thickness
Ellipsometer: Recipe: SiO_2 on thermal SiO_2 on Si

PR 1805 all gone.
Remaining SiO_2 thickness: 5235, 5289, 5341, 5321, 5216, 5290, 5396, 5187 (in Å)
Average: 5284 Å

Etching SiO_2: test SiO_2 etching rate RIE (**rate ~ 272 Å /min**)
Recipe: **planr12**: Ar 70sccm, CF 47sccm, CHF3 6sccm for **6 min**

*Measure remaining SiO_2 thickness
Ellipsometer: Recipe: SiO_2 on thermal SiO_2 on Si

Remaining SiO_2 thickness: 3487, 3671, 3628, 3583, 3512, 3697, 3525, 3642 (in Å)
Average: 3581 Å
Actual etching rate: 283.7Å/min

Etching SiO2: Expose the capping metal contact
Recipe: planr12: Ar 70sccm, CF 47sccm, CHF3 6sccm for 2 min 40 s

Remaining SiO_2 thickness: 2812, 2934, 2876, 2785, 2847, 2963, 2749, 2863 (in Å)
Average: 2853.6 Å

Pillar Exposed. Planarization done!

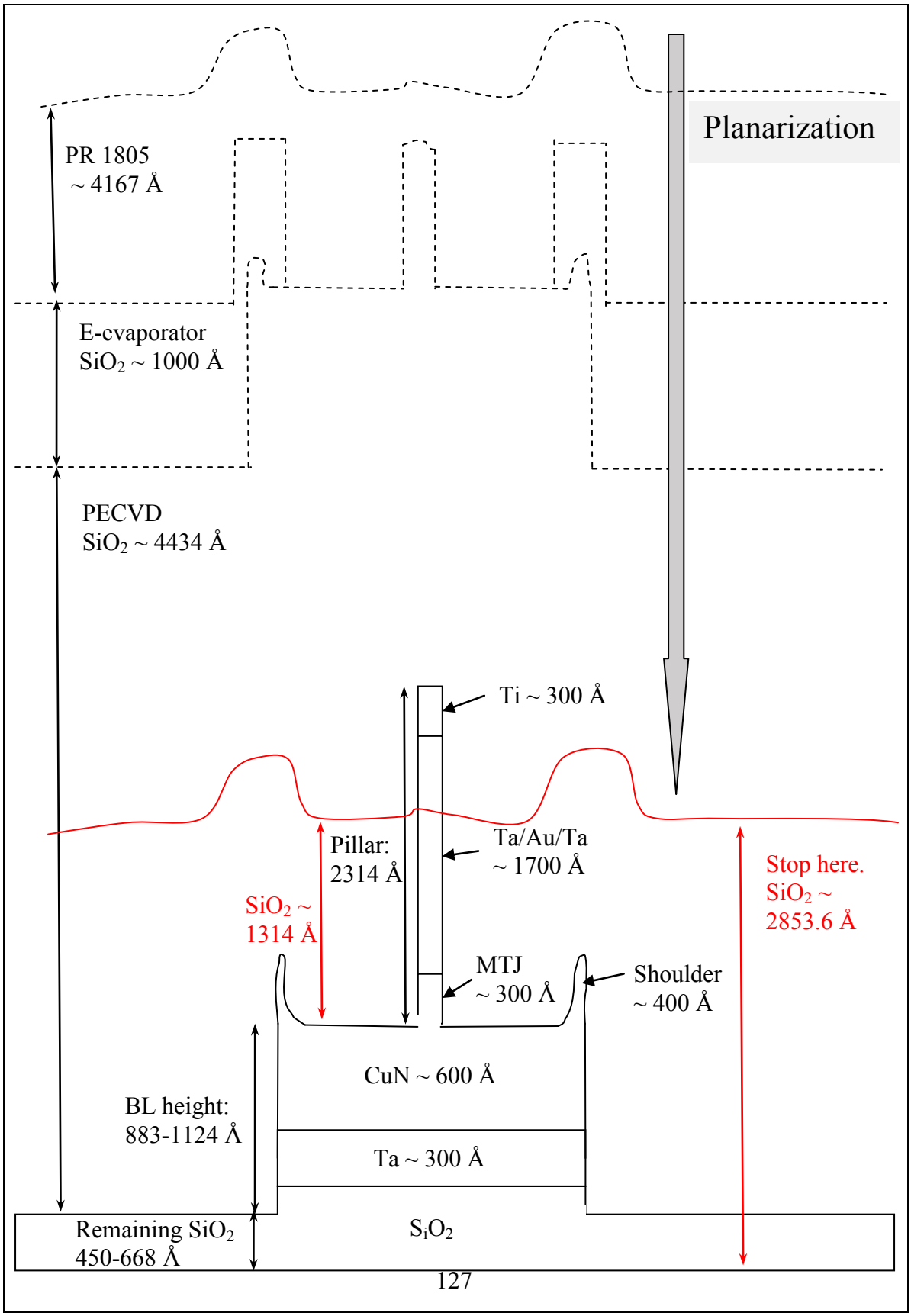
Planarization
PR 1805
~ 4167 Å
E-evaporator
SiO_2 ~ 1000 Å
PECVD
SiO_2 ~ 4434 Å
Ti ~ 300 Å
Pillar:
2314 Å
Ta/Au/Ta
~ 1700 Å
SiO_2 ~
1314 Å
Stop here.
SiO_2 ~
2853.6 Å
MTJ
~ 300 Å
Shoulder
~ 400 Å
CuN ~ 600 Å
BL height:
883-1124 Å
Ta ~ 300 Å
Remaining SiO_2
450-668 Å
S_iO_2

Step 22: Bottom electrode hole masks exposing. (clean-room, bay3)

Photo Resist Coating:

Equipment: CEE Photoresist Spinner
Condition:

☐Pre-bake 170^{o}C for 5 min

☐Program 4: Coat PR1813 at 4000RPM 30 seconds (around 18000Å thick).

☐Soft Bake 150^{o}C for 5 minute

Comments: CEE **vacuum** test first!

Mask exposing (mask name: T-E L-3) :

Equipment: KARLSUSS MAB6
Condition: Program: Vacuum cont.

☐Time: 5.5 seconds, Power: 12mW/cm^2

Comments:

Photo Resist developing:

Solution: MF:319 developer
Condition:

☐ MF:319 time=1 min 30 s

☐DI water rinse; N2 blow dry

☐Hard Bake: 120°C for 1 min.

☐Microscope: to check the pattern shape

Comments: little bit over developing is good for this step.

Step 23: STS etching

Equipment: STS
Condition: file name: "planr12.set"

Comment: for PECVD 150°C SiO_2, etching rate is 304.6A/min
STS doesn't etch metal or metal oxide
Actual etching time =SiO_2 thickness+2min.

☐For 1314Å SiO_2 from PECVD, so run the process about 5 min +2 min.
☐Put acetone into ultrasonic to clean PR for 10 min
☐DI water tank; DI water rinse; N2 blow dry
☐Microscope to check the pattern

Comment: When clean the wafer (when get it out of Acetone), do be quick to avoid the wafer dry itself which induces a lot of contamination.

Check the BL contact by four point probes to confirm SiO_2 is gone.

Step 24: Top electrode masks exposing. (clean-room, bay2)

Photo Resist Coating:

Equipment: CEE Photoresist Spinner(Double layers: SF 5, PR 1813)

Condition: **SF5:**

☐Pre-bake 170^{o}C for 5 minute (to remove H2O totally), cool down for a few sec.

☐Program 9: 500RPM/500RPM (acc)-10sec/4000RPM/4000PRM (acc)-35sec.

☐Bake at 150^{o}C for 5 minute

PR1813:

☐Program 4: Coat PR1813 at 4000RPM 30 seconds

☐Soft Bake 105^{o}C for 1 minute

Comments: CEE **vacuum** test first

Pure SF 5 need to be quick, pure it in the center.

Mask exposing (mask name: T-E L-4) :

Equipment: KARLSUSS MAB6

Condition: Program: Hard-Ct/cont.

☐Time: 5.5 seconds, Distance 20 *u*m, Power: 12mW/cm^2

Comments:

Photo Resist developing:

Solution: MF319 (avoid water)

Condition:

☐Clean beaker: use DI water and MF319 to clean the beaker and blow dry

☐MF319 time: 1.5 min

☐DI water rinse and N2 blow dry.

☐Microscope: to check if the pillar shape is good

☐Hard Bake: 120°C for 1 min.

Comments:

Step25: Leads Deposition (Ta 50/Cu 1000/Ta 200A)

Equipment: AJA

Condition:

☐Pre-sputter #2-Ta #5-Cu

☐Etching 5min

☐Deposit Ta 200w 50sccm 80sec (50 Å)

☐Deposit Cu 250w 45sccm 780sec (2500 Å)

☐Deposit Ta 200w 50sccm 80sec (50 Å)

☐Deposit Au 250w 50sccm 193sec (2500 Å)

Step 26: lift-off. (clean-room, bay 2)

Solution: Developer 1165

☐Condition: Heat set point at 70 ^{o}C for 45min+.

Put 1165 into Ultrasonic for 25min+ (1165 can be heated to 60 ^{o}C first).

Water tank; DI water rinse; N2 blow dry.

Check with Microscopes.

Comments: Before lift-off, make some stripes on the unuseful area to help lift-off.

Several bathes during the heating and Ultrasonic

Notes: for SJY33 heating time:

Ultrasonic time:

Appendix B: Publication List

1. **H. Zhao**, A. Lyle, Y. Zhang, P. K. Amiri, G. Rowlands, Z. Zeng, J. Katine, H. Jiang, K. Galatsis, K. L. Wang, I. N. Krivorotov, and J.-P. Wang, "Low writing energy and sub nanosecond spin torque transfer switching of in-plane magnetic tunnel junction for spin torque transfer random access memory," *Journal of Applied Physics*, vol. 109, no. 7, pp. 07C720–07C720–3, Mar. 2011.

2. **H. Zhao**, B. Glass, P. K. Amiri, A. Lyle, Y. Zhang, Y.-J. Chen, G. Rowlands, P. Upadhyaya, Z. Zeng, J. A. Katine, J. Langer, K. Galatsis, H. Jiang, K. L. Wang, I. N. Krivorotov, and J.-P. Wang, "Sub-200 ps spin transfer torque switching in in-plane magnetic tunnel junctions with interface perpendicular anisotropy," *Journal of Physics D: Applied Physics*, vol. 45, no. 2, p. 025001, Jan. 2012.

3. **H. Zhao**, P. K. Amiri, Y. Zhang, A. Lyle, J. A. Katine, J. Langer, H. Jiang, K. L. Wang, I. N. Krivorotov, and J.-P. Wang, "Spin-Transfer Torque Switching Above Ambient Temperature," *IEEE Magnetics Letters*, vol. 3, pp. 3000304–3000304, 2012.

4. **H. Zhao**, Y. Zhang, P. K. Amiri, J. A. Katine, J. Langer, H. Jiang, I. N. Krivorotov, K. L. Wang, and J.-P. Wang, "Spin-Torque Driven Switching Probability Density Function Asymmetry," *IEEE Transactions on Magnetics*, vol. 48, no. 11, pp. 3818–3820, Nov. 2012.

5. K. C. Chun, **H. Zhao**, J. D. Harms, T.-H. Kim, J.-P. Wang, and C. H. Kim, "A Scaling Roadmap and Performance Evaluation of In-Plane and Perpendicular MTJ Based STT-MRAMs for High-Density Cache Memory," *IEEE Journal of Solid-State Circuits*, vol. 48, no. 2, pp. 598–610, Feb. 2013.

6. Y. Zhang, **H. Zhao**, A. Lyle, and J.-P. Wang, "Power enhancement of angular polarizer spin torque oscillator in magnetic tunnel junction," *Journal of Applied Physics*, vol. 109, no. 7, pp. 07C714–07C714–3, Mar. 2011.

7. Y. Zhang, **H. Zhao**, A. Lyle, P. A. Crowell, and J.-P. Wang, "Spin torque oscillation modes of a dual magnetic tunneling junction," *Journal of Applied Physics*, vol. 109, no. 7, pp. 07D307–07D307–3, Mar. 2011.

8. Y. Zhang, **H. Zhao**, A. Lyle, P. A. Crowell, and J.-P. Wang, "High power and low critical current spin torque oscillation from a magnetic tunnel junction with a built-in hard axis polarizer," *Applied Physics Letters*, vol. 100, no. 3, pp. 032405–032405–4, Jan. 2012.

9. Z.M. Zeng, P. K. Amiri, I. N. Krivorotov, **H. Zhao**, G. Finocchio, J.-P. Wang, J. A. Katine, Y. Huai, J. Langer, K. Galatsis, K. L. Wang, and H. Jiang, "High-Power Coherent

Microwave Emission from Magnetic Tunnel Junction Nano-oscillators with Perpendicular Anisotropy," *ACS Nano*, vol. 6, no. 7, pp. 6115–6121, Jul. 2012.

10. Z. M. Zeng, P. Khalili Amiri, G. Rowlands, **H. Zhao**, I. N. Krivorotov, J.-P. Wang, J. A. Katine, J. Langer, K. Galatsis, K. L. Wang, and H. W. Jiang, "Effect of resistance-area product on spin-transfer switching in MgO-based magnetic tunnel junction memory cells," *Applied Physics Letters*, vol. 98, no. 7, pp. 072512–072512–3, Feb. 2011.

11. A. Lyle, A. Klemm, J. Harms, Y. Zhang, **H. Zhao**, and J.-P. Wang, "Probing dipole coupled nanomagnets using magnetoresistance read," *Applied Physics Letters*, vol. 98, no. 9, pp. 092502–092502–3, Feb. 2011.

12. P. K. Amiri, Z. M. Zeng, P. Upadhyaya, G. Rowlands, **H. Zhao**, I. N. Krivorotov, J.-P. Wang, H. W. Jiang, J. A. Katine, J. Langer, K. Galatsis, and K. L. Wang, "Low Write-Energy Magnetic Tunnel Junctions for High-Speed Spin-Transfer-Torque MRAM," *IEEE Electron Device Letters*, vol. 32, no. 1, pp. 57–59, Jan. 2011.

13. M. T. Rahman, A. Lyle, P. Khalili Amiri, J. Harms, B. Glass, **H. Zhao**, G. Rowlands, J. A. Katine, J. Langer, I. N. Krivorotov, K. L. Wang, and J. P. Wang, "Reduction of switching current density in perpendicular magnetic tunnel junctions by tuning the anisotropy of the CoFeB free layer," *Journal of Applied Physics*, vol. 111, no. 7, pp. 07C907–07C907–3, Feb. 2012.

14. P. Khalili Amiri, Z. M. Zeng, J. Langer, **H. Zhao**, G. Rowlands, Y.-J. Chen, I. N. Krivorotov, J.-P. Wang, H. W. Jiang, J. A. Katine, Y. Huai, K. Galatsis, and K. L. Wang, "Switching current reduction using perpendicular anisotropy in CoFeB–MgO magnetic tunnel junctions," *Applied Physics Letters*, vol. 98, no. 11, p. 112507, 2011.

15. G. E. Rowlands, T. Rahman, J. A. Katine, J. Langer, A. Lyle, **H. Zhao**, J. G. Alzate, A. A. Kovalev, Y. Tserkovnyak, Z. M. Zeng, H. W. Jiang, K. Galatsis, Y. M. Huai, P. K. Amiri, K. L. Wang, I. N. Krivorotov, and J.-P. Wang, "Deep subnanosecond spin torque switching in magnetic tunnel junctions with combined in-plane and perpendicular polarizers," *Applied Physics Letters*, vol. 98, no. 10, pp. 102509–102509–3, Mar. 2011.